Czech University of Life Sciences Prague
Faculty of Engineering

2023

Proceeding of 25th International Conference of Young Scientists 2023

Czech University of Life Sciences Prague – Faculty of Engineering

Sept. 12th – Sept. 13th 2023

CZECH UNIVERSITY OF LIFE SCIENCES PRAGUE

FACULTY OF ENGINEERING

25th INTERNATIONAL CONFERENCE OF YOUNG SCIENTISTS 2023

PROCEEDING OF 25TH INTERNATIONAL CONFERENCE OF YOUNG SCIENTISTS 2023

September 12th 2023 – September 13th 2023

Prague

Czech Republic

Editors: Rostislav Chotěborský, Barbora Černilová, Lenka Křivánková

ISBN 978-80-213-3345-1

25th International Conference of Young Scientists 2023

September 12th 2023 – September 13th 2023

Conference ICYS publishes research in engineering and physical sciences that represent advances in understanding or modelling of the performance of biological and physical systems for sustainable developments in land use and the environment, agriculture and amenity, bioproduction processes and the food chain, logistics systems in agriculture, manufacturing and material systems in design of agriculture engineering.

Conference venue:

Faculty of Engineering, Czech University of Life Sciences Prague, Kamýcká 129, Praha 6, Prague, 165 21, Czech Republic

Scientific committee:

doc. Ing. Jiří Mašek, Ph.D.

prof. Ing. David Herák, Ph.D.

doc. Ing. Rostislav Chotěborský. Ph.D.

prof. Ing. Roman Gálik, Ph.D.

doc. RNDr. Vlasta Vozárová, PhD.

doc. Ing. Pavel Beňo, PhD.

doc. Ing. Peter Koleda, Ph.D.

CONTENT

Application of thermal images as a tool for precision agriculture

K. Balážová[1], S. Petrásek [1], J. Kumhálová[2]

[1]*Department of Africultural Machines, Faculty of Engineering, Czech University of Life Sciences Prague, Prague, Czech Republic*

[2]*Department of Vehicles and Ground Transport, Faculty of Engineering, Czech University of Life Sciences Prague, Prague, Czech Republic*

Abstract

This article focuses on the use of thermal images from the DuetT camera (senseFly) and images from the handheld Flir 5E device to monitor water stress in 2 varieties of spring wheat (*Triticum aestivum*), modern variety Kabot and old variety Khorasan. The experiment was arranged on six plots, one half of which was sown with the Khorasan wheat variety and the other half was sown with the Kabot wheat variety. Three tillage methods were used for each cultivar: conventional processing (CT) (20–25 cm), minimum processing (MTC) with a share cultivator (15 cm) and minimization processing (MTD) with a disc cultivator (12 cm). The air mission using the EbeeX UAV was complemented by measuring the temperature of individual sheets from a height of about 1 m using a DuetT thermal camera and a Flir E5 handheld sensor. The temperature of the canopy (T_c) was determined from the air mission and the reference temperatures (T_{dry}) and (T_{wet}) from the measurements of the individual sheets. The results showed that the differences between varieties and tillage were not statistically significant.

Key words: water stress, thermal remote sensing, UAV

INTRODUCTION

Nowadays, crop condition monitoring using unmanned aerial vehicles (UAVs) fitted with multispectral or thermal cameras is a very important and useful area of precision agriculture (Amaral et al., 2021). In addition, Comba et al. (2015) points to the advantage of images taken from unmanned aerial vehicles, which have a very high spatial resolution and can thus monitor the structure and health of the stand with very high accuracy. This is also the case with thermal imaging using UAVs, which are non-invasive monitoring devices and can quickly evaluate the temperature of the canopy or provide important quantitative information about the state of water in the stand (Das et al., 2021).

Canopy temperature (T_c) is determined by heat and water vapour flow and is closely related to water stress, as water deficiency results in reduced stomatal conductivity and evapotraspiration rate, resulting in an increase in leaf/canopic temperature. (Luan and Vico, 2021). According to Matese et al. (2018), plants manifest themselves in water scarcity by

several mechanisms that allow adaptation to slow or rapid water scarcity, while particular attention is paid to the increase in CO_2 (Messina and Modica, 2020). According to Berni et al. (2009), the canopy temperature (T_c) can provide information for estimating stomatal conductivity to water vapor and water status in the plant.

Further, Jones et al. (2002) points out that the physiological parameters of the leaves are not always straightforward, especially in variable meteorology (atmospheric pressure, radiation, wind speed, humidity, etc.). Fuentes et al. (2012) also addresses in their study the time of day when the images are taken, according to him, the measurement should be carried out in the hottest part of the day (between 12:00 and 15:30), when the differences between stressed vegetation and non-stressed should be best seen. Emerging problems arising from changing conditions can be solved, according to Jones et al. (1997), by using "dry" or "wet" and "dry" reference surfaces. Another option is to compare the current temperature of the canopy with temperatures at maximum ("wet") and zero ("dry") levels of transpiration in the same climatic environment.

One of the most reliable indices proposed by Idso et al. (1981) is the Crop Water Stress Index (CWSI), which is used to calculate water stress when it is normalized by the temperature difference between the stand surface and air by the vapour pressure deficit (VPD), which allows comparison of the state of the stand of a wide range of crops (vines, wheat, rice, sunflower, corn or cotton) under different environmental conditions and terms (Jones et al. 2002),(Alchanatis et al., 2010). After adjusting the index by Jones et al. (2002), the reference temperatures T_{dry} and T_{wet} were added for a more reliable interpretation of the results. Many authors see in CWSI the potential for irrigation planning (Costa et al., 2020). However, the best choice of heat indices for accurate information on water stress is still unclear (Pou et al., 2014).

MATERIALS AND METHODS

Experimental area

The study was conducted in the 2023 vegetation season and was in six regular plots in the size of 4 × 50 m near Čenovice (49°47′42.78″ N, 15°6′35.94″ E), a central Bohemian region in the Czech Republic. The soil is Haplic Luvisol. Temperature was measured by an agrometeorological station located next to the experiment (Tab 1.).

Tab 1. Temperatures at different growth stages according to the BBCH and for measurement data

Growth stages	Temperature (°C)
BBCH 55- 59 (Heading)	21.5 for July 4 (in measured time 11:50)
after 60 BBCH (Anthesis)	31.7 for July 11 (in measured time 15:10)

UAV, handheld instrument Canopy Sensing and Data Processing

Aerial photography of the term 4th July 2023 was carried out using a fixed wing eBeeX drone fitted with a dual DuetT camera (senseFly SA, Route de Genéve 38, Cheseaux-sur-Lausanne, Switzerland). The measurements with the DuetT camera were carried out with 80% longitudinal and 75% side overlap and at a height of approximately 91.8 m above the elevation data flight altitude, with a 12 $\mathrm{cm} \cdot \mathrm{px}^{-1}$ resulting spatial resolution for the thermal images. The current temperature of the canopy was measured in all 6 variants.

T_{dry} and T_{wet} reference were measured using a handheld Flir-E5 sensor (Flir systems OÜ, Estonia) and a DuetT camera holding about 1 m above the ground. The measurement took place on 11th July 2023 when the wheat was in BBCH after 60 Anthesis. Selected plant leaves in the selected variants were lubricated with white petroleum jelly on the plant so that the lower and top of the leaf were covered with a layer of petroleum jelly and the stomata was closed and evapotranspiration was prevented. This starts to heat the leaf and demonstrates T_{dry} -temperature corresponding to the dry surface (°C). The sheets were taken after about 30 minutes and were measured using a FLIR and handheld sensor and a DuetT camera. Other leaves were treated on both sides with water with added wetting agent (spring). This demonstrated T_{wet} - temperature corresponding to the wet surface (°C). The sheets were also measured after 20 seconds using only a Flir E5 handheld sensor because the DuetT camera collapsed due to overheating.

Images from Duet T thermal camera were processed using Duet T templates. The thermal maps were visualized in absolute temperature values. The resulting layers were in the GeoTIFF format georeferenced in the WGS84 UTM Zone 33N coordinate system.

RESULTS AND DISCUSSION

The development of the canopy temperature (T_c) depends on the density of the stand and other factors, such as meteorological conditions, thermal camera properties or the intensity of thermal radiation at the time of taking the images (Khanal et al., 2017). Figure (Fig. 1) shows small differences in temperatures between tillage methods. Varietally, Khorasan wheat seems to show a higher temperature. According to Nakhforoosh et al. (2015), Kamut showed the lowest separating ability compared to other varieties. As a result, the vegetation can be less involved. Thus, a larger area of soil is exposed and there is a higher evaporation of available water from the soil.

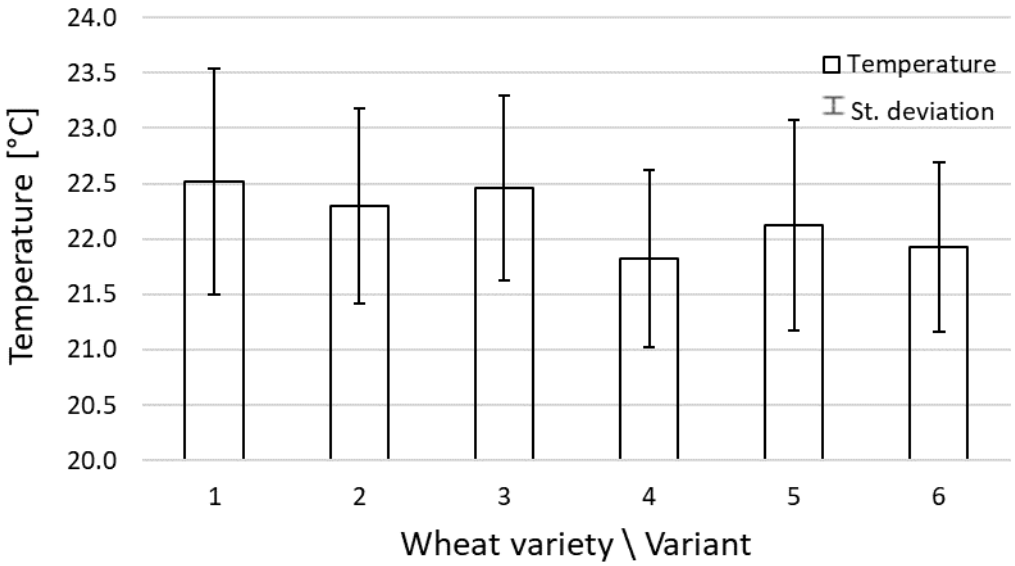

Fig. 1 Comparison of stand temperatures (°C) for individual variants taken using thermal imaging from DuetT

Figure (Fig. 2) of Part A shows the reference temperature T_{wet}. In this case, it was measured in the Kamut variety, which has been treated with tillage (MTC). After applying spring water to both sides of the leaf and waiting 20 s, a T_{wet} of 23.7 °C was measured. According to Brennan et al. (2007), transpiration has a cooling effect because the hottest molecule escapes from the plant. In Part B, a reference value of T_{dry} was measured for the same Kamut variety and the same tillage variant was read 30 minutes after treatment with petroleum jelly on both sides of the leaf. The measured value of T_{dry} was 41.6 °C. Transpiration is an important factor for overall plant temperature during drought stress (James et al., 2008). These refencies are the basis for calculating the crop water stress index (CWSI), but they must be measured in the same environment and at the same time to be exposed to the same meteorological conditions (Banerjee et al., 2020).

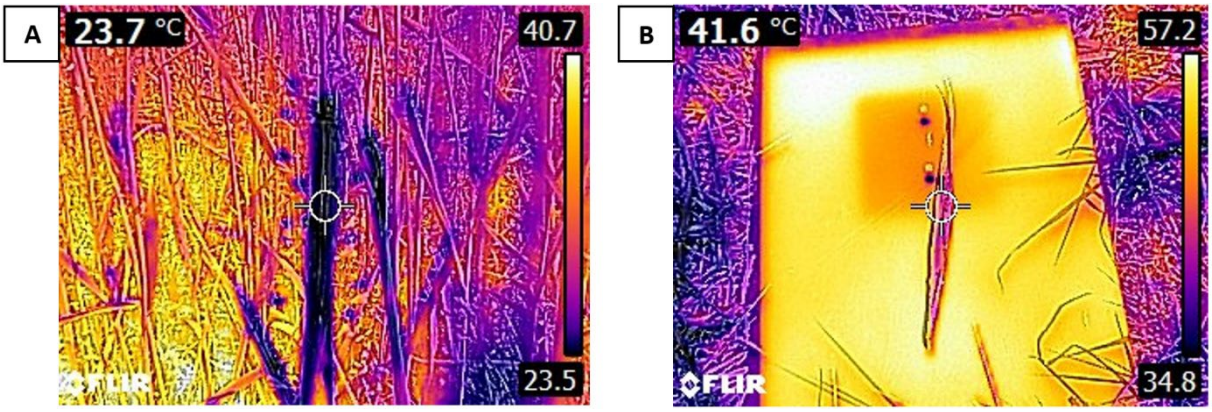

Fig. 2. Images taken from the handheld Flir E5 sensor. Part A shows the value of the reference temperatures T_{wet} (°C) for the Kamut variety treated with minimal tillage (MTC) and part B shows the value of reference temperatures T_{dry} (°C) for the same treatment variants

Figure (Fig. 3) shows an image taken from a DuetT thermal camera held about 1 m above an object, specifically a leaf of the Kamut tillage treated (MTC) variety. The measured T_{dry} reference value is shown more generally for method comparison, but its value is around 45 °C. According to Ali et al. (2021) it is good to use IR-based thermal imaging, as it can identify sensitive plants when drought stress is initiated or determine stress tolerance in different cultivars. He also points out that plants that have cooler surfaces than others are more demanding on the water they consume, which they transpire.

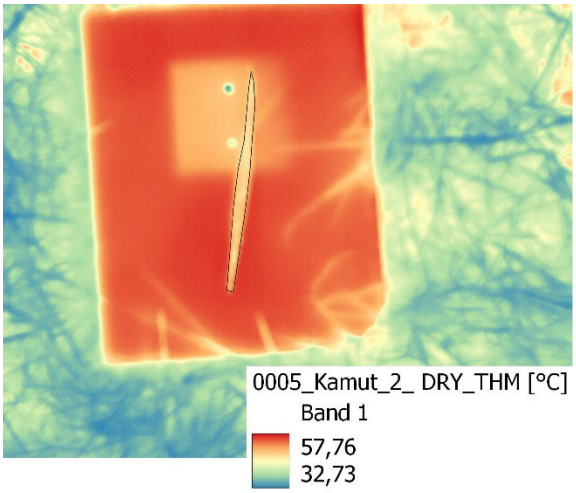

Fig. 3 An image taken by the DuetT camera showing a Kamut wheat leaf treated with tillage (MTC) and its reference T_{dry}

CONCLUSION

According to the evaluated results, in terms of canopy temperature, there were no statistical differences between the varieties and the different tillage. Images taken with the Flir E5 handheld sensor and the DuetT thermal camera are a good indicator of dry stress. However, more detailed research and more experiments are needed to achieve better results on the stand. In conclusion, however, thermal imaging is an ideal way to find out the necessary information about the state and usability of water by plants, and it is even possible to create irrigation maps, which would be a welcome bonus for many farmers.

ACKNOWLEDGEMENT

This research was funded by internal project of the Faculty of Engineering at the Czech University of Life Sciences Prague, grant number 2023: 31160/1312/3108.

REFERENCES

Alchanatis, V., Cohen, Y., Cohen, S., Moller, M., Sprinstin, M., Meron, M., Tsipris, J., Saranga, Y., & Sela, E. (2010). Evaluation of different approaches for estimating and mapping crop water status in cotton with thermal imaging. *Precision Agriculture*, 11, 27 – 41.

Ali, F., Umar, M., & Siddiqui, Z. S. (2021). Comparative physiological assessment of some edible oil-seed crops under drought stress environment using fluorescence and IR imaging techniques. *Pak. J. Bot*, 53(4), 1183-1192.

Amaral, L. R. D., Zerbato, C., Freitas, R. G. D., Barbosa Júnior, M. R., & Simões. (2021) I. O. P. D. S. UAV applications in Agriculture 4.0. *Revista Ciência Agronômica*, 51.

Banerjee, K., Krishnan, P., & Das, B. (2020). Thermal imaging and multivariate techniques for characterizing and screening wheat genotypes under water stress condition. *Ecological Indicators*, 119, 106829.

Brennan, J.P., A.G. Condon, M. Van-Ginkel and M.P. Reynolds. 2007. An economic assessment of the use of physiological selection for stomatal aperture-related traits in the CIMMYT wheat breeding program. *J. Agric. Sci.*, 145: 187-194

Comba, L., Gay, P., Primicerio, J., & Aimonino, D. R. (2015). Vineyard detection from unmanned aerial systems images. *computers and Electronics in Agriculture*, *114*. 78-87.

Costa, J. D. O., Coelho, R. D., Barros, T. H. D. S., Fraga Junior, E. F., & Fernandes, A. L. T. (2020). Canopy thermal response to water deficit of coffee plants under drip irrigation. *Irrigation and drainage*, 69(3), 472-482.

Das, S., Christopher, J., Apan, A., Choudhury, M. R., Chapman, S., Menzies, N. W., & Dang Y. P. (2021). UAV-Thermal imaging and agglomerative hierarchical clustering techniques to evaluate and rank physiological performance of wheat genotypes on sodic soil. ISPRS *Journal of Photogrammetry and Remote Sensing*, 173, 221-237.

Fuentes, S., De Bei, R., Pech, J., & Tyerman, S. (2012). Computational water stress indices obtained from thermal image analysis of grapevine canopies. Irrigation Science, 30, 523-536.

Idso, S.B., Jackson, R.D., Pinter, P.J., Reginato, R.J., Hatfield, J.L. (1981). Normalizing the Stress-Degree-Day Parameter for Environmental Variability. Agricultural Meteorology, 24(C):45-55.

James, A. T., Lawn, R. J., & Cooper, M. (2008). Genotypic variation for drought stress response traits in soybean. II. Inter-relations between epidermal conductance, osmotic potential, relative water content, and plant survival. *Australian Journal of Agricultural Research*, 59(7), 670-678.

Jones, H. G., Stoll, M., Santos, T., Sousa, C. D., Chaves, M. M., & Grant, O. M. (2002). Use of infrared thermography for monitoring stomatal closure in the field: application to grapevine. *Journal of experimental botany*, 53(378), 2249-2260.

Khanal, S., Fulton, J., & Shearer, S. (2017). An overview of current and potential applications of thermal remote sensing in precision agriculture. *Computers and Electronics in Agriculture*, 139, 22-32.

Luan, X. & Vico, G. (2021) Canopy temperature and heat stress are increased by compound high air temperature and water stress and reduced by irrigation–a modeling analysis. *Hydrology and Earth System Sciences*, 2021. 25(3), 1411-1423.

Matese, A., Baraldi, R. Berton, A., Cesaraccio, C., Di Gennaro, S.F., Duce, P., Facini, O., Mameli, M.G., Piga, A., Zaldei, A. (2018). Estimation of Water Stress in Grapevines Using Proximal and Remote Sensing Methods. *Remote Sensing*, 10, 114.

Messina., G. & Modica. G. (2020). Applications of UAV Thermal Imagery in Precision Agriculture: State of the Art and Future Research Outlook. *Remote Sensing*, *12*. 1491.

Nakhforoosh, A., Grausgruber, H., Kaul, H. P., & Bodner, G. (2015). Dissection of drought response of modern and underutilized wheat varieties according to Passioura's yield-water framework. *Frontiers in plant science*, 6, 570.

Pou, A., Diago, M. P., Medrano, H., Baluja, J., & Tardaguila, J. (2014). Validation of thermal indices for water status identification in grapevine. *Agricultural water management*, 134, 60-72.

The study of selected tribological properties of different hardfacing materials

L. Boszorádová[1], M. Baráth[1], M. Kotus[1],

1 Institute of Design and Engineering Technologies, Faculty of Engineering, Slovak University of Agriculture in Nitra, Tr. A. Hlinku 2, 949 76 Nitra, Slovakia

Abstract

The aim of this paper is study properties of four hardfacing materials Ok 86.08, Ok 86.28, Fluxofil 54 and Fluxofil 58. The abrasive wear behavior of these materials is studied. To evaluate wear resistance two-body abrasion test was used. Average weight loss was used to evaluate wear resistance of materials. Results were statistically processed. The results of this study showed a significant influence of the chemical composition of the material and the synergy of the individual chemical elements to the wear resistance of the materials.

Key words: wear resistance, hardfacing, two- body abrasion test, hardness

INTRODUCTION

Wear is responsible for the degradation of machinery and its components, limiting their lifetime while their repair entails service and maintenance costs. Wear is influenced by a series of internal and external factors. The five main types of wear are adhesive, abrasive, fatigue wear, fretting, and erosion, which are commonly observed in practical situations. Hardfacing is a form of resistance to wear; it is an application of the build-up of deposits of special alloys on surfaces. Therefore, it is helpful in experimentally estimating wear resistance, as well as the factors that guide the selection of materials for abrasion conditions, experimentally (Slota et.al., 2022). Studies on the abrasive wear issues show that the use of a wide variety of hardfacing techniques can improve the performance of machinery and machinery components in an industry in an economical manner. Hardfacing is emerging as the most versatile method for depositing wear-resistant layers on a wide variety of materials (Badisch et.al., 2013), (Kenchireddy et.al., 2014), (Venkatesh et al., 2015) presented state-of-the-art wear characteristics of hardfacing alloys. An analysis of the literature shows that wear resistance depends on factors such as hardfacing alloys, erodent and abrasion particles, matrix hardening agents, temperature and matrix materials. (Venkatesh et al., 2020) studied the wear characteristics of multi-layer Fe-C-Cr hardfacing alloys on a pin-on-disc tribometer. It was revealed that an increase in carbon content increases the hardness, but also increases the brittleness soft he hardfacing alloys. The authors (Javeheri et. al., 2018) have defined four types of interaction between abrasive particles and worn material. It is a general model of abrasive wear. Typical situations that occur during abrasive wear: microploughing, microcutting, microcutting connected with fatigue fracture, microcutting connected with microcracks. (Wang et al., 2008) studied the microstructure,

hardness and wear resistance of Fe-based alloys by adding the elements ferrotitanium (Fe–Ti), ferromolybdenum (Fe–Mo), ferrovanadium (Fe–V) and graphite, which were applied by the arc welding process. The results showed that the hardness and resistance of the hardfacing metal layer increase with an increasing proportion of Fe-Ti, Fe-V, Fe-Mo and graphite. Their amounts must be controlled in the range of 8–10% graphite, 12–15% Fe-Ti, 10–12% Fe-V and 2–4% Fe-Mo. However, cracks begin to form in the layer of hardfacing metal if the amount of Fe-Mo is more than 5%.

MATERIALS AND METHODS

Test specimens were manufactured from the STN 12 050 steel. The specimens had shape of cylinders with a diameter of 10 mm and length of 60 mm. To create the studied hardfacing layers four different hardfacing materials were used, their properties are in table (Tab. 1). Depending on the used harfacing material the layers on the samples were created using MMA and MAG technologies. The manufacturers of the hardfacing materials recommend creating deposits with three layers. Within the research, the properties of the the created deposits were observed and compared after each created layer. The wear resistance of each material to wear was assessed by measuring the average weight loss of the specimens. Each sample was measured four times, and from these values, the arithmetic mean and standard deviation were calculated. Abrasive wear process was performed in the laboratory using a device that simulates abrasive wear. The abrasive was in the form of abrasive cloth with a grit size of P100. Another examined property was hardness. The Vickers method was chosen for measuring hardness. The measurement was carried out on an HPO 250 instrument with an applied force of 98N and a maximum loading time of 15s.

Tab. 1 Chemical composition of cladding materials used (wt. %)

	C	Si	Mn	Cr	Mo	Ni
OK 86.08	1.08	0.7	12.2			
OK 86.28	0.67	0.2	13.2			3
Fluxofil 54	0.1	0.6	1.5	5.5	0.9	
Fluxofil 58	0.45	0.6	1.6	5.5	0.6	

RESULTS AND DISCUSSION

In the figure (Fig. 1) we can see the average weight losses of deposits created by different hardfacing materials. The coefficient of variation ranged from 0.88% (for Fluxofil 54, third layer) to 2.99% (for OK 86.08, third layer). As we can see, the lowest value of average weight loss was achieved by the Fluxofil 58 material. Compared to the OK 86.08 material, which had the highest weight loss, Fluxofil 58 achieved an average weight loss that was 53% lower. We can also observe the significance of creating multi-layer deposits, where the difference in average weight loss between the first and third layers was from 8.7% to 16%.

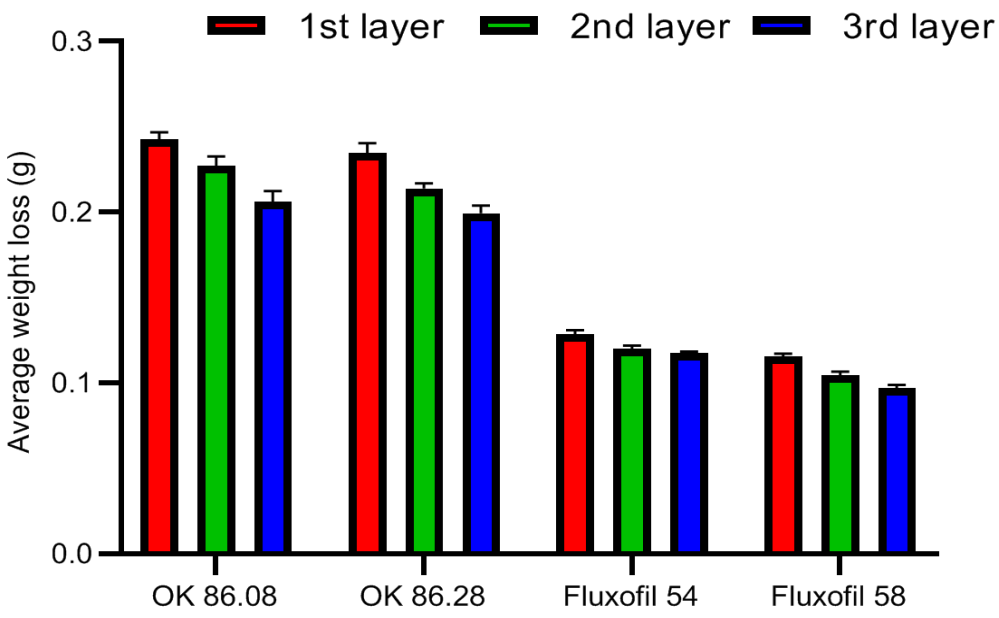

Fig. 1 Comparison of the average weight loss of the observed materials

In the figure (Fig. 2) we can see a comparison of the relative wear resistance of layers created with different hardfacing materials in comparison to the base material and the reference material. The relative wear resistance of the material was increased by 172% by creating a layer with the Fluxofil 58 material. For the remaining hardfacing materials, an increase in wear resistance of the base material was achieved, ranging from 28% to 125%.

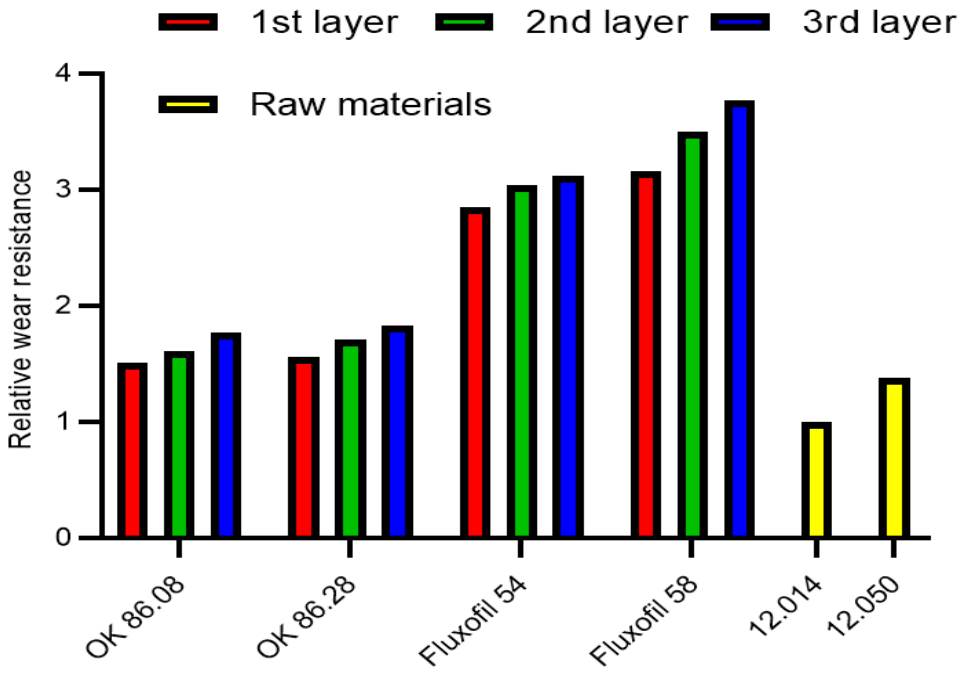

Fig. 2 Comparison of the relative wear resistance of observed materials and standard material and base material

The Figure (Fig. 3) illustrates the hardness of deposits created using different hardfacing materials. Fluxofil 58 has significantly higher hardness compared to Fluxofil 54 due to its higher carbon content. Electrodes do not contain Cr and Mo, and their hardness is comparable to Fluxofil 54 due to the higher content of C and Mn. Upon observing the Figure 1 and the Figure 3, it is evident that material wear resistance depends not only on the hardness of the material but primarily on the elements that the material contains. For example, even though the difference in hardness between OK 86.08 and Fluxofil 54 is only about 8%, the difference in their average weight losses is 43%. The significantly higher wear resistance of Fluxofil 54 and Fluxofil 58 materials is attributed to the presence of Cr and Mn in these materials.

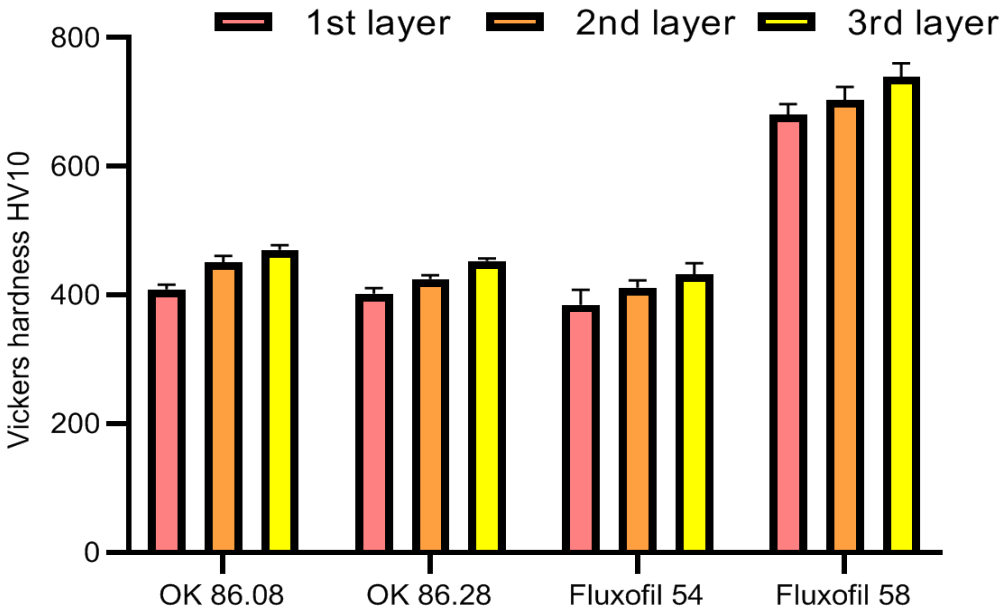

Fig. 3 Comparison of the Vickers hardness of the observed materials

Authors (Wang et al., 2008) conducted a study on the influence of alloying elements on wear resistance, and their research shows that increasing the content of molybdenum leads to an increase in material wear resistance. This correlates with our results, as materials containing Mo exhibited higher wear resistance. The research by (Tang and Li, 2023) focuses on the impact of C, Si, and Mn on material wear resistance. They found that these elements and their synergies determine the resulting material properties. Similarly, in our case, the differences in C content of 0.35%, Mn content of 0.1%, and Mo content of 0.1% caused a significant change in material wear resistance. Furthermore, the research by (Zhao et al., 2023) demonstrates the significant synergistic effect of individual elements on the resulting wear resistance of materials.

CONCLUSION

This paper is focused to compare wear resistance and hardness of for different hardfacing materials. Specifically OK 86.08, OK 86.28, Fluxofil 54 and Fluxofil 58. The result shows that the wear resistance of materials does not only depend on their hardness, but also their chemical composition has a significant influence. The presence of elements like Cr and Mo, as seen,

considerably enhanced the material's resistance to wear. Since Fluxofil 54 Ok 86.08 and Ok 86.28 have comparable hardness, Fluxofil 54 has 43% less weight loss. From all these results we can conclude were resistance of material depends on chemical composition and on synergy of chemical elements.

ACKNOWLEDGEMENTS

This paper was created within the project KEGA no. 003SPU-4/2021 “An Innovation of Study Programs using New Education Methods and Advanced Manufacturing Technologies.”

REFERENCES

Badisch, E., Roy, M. (2013). Hardfacing for Wear, Erosion and Abrasion. *Surface Engineering for Enhanced Performance against Wear*.

Javaheri, V., Porter D., Kuokkala V.T. (2018). Slurry erosion of steel – Review of tests, mechanisms and materials. *Wear*.

Kenchireddy, K.M., Jayadeva, C.T., Sreenivasan, A. (2014). Influence of material characteristics on the abrasive wear response of some hardfacing alloys. *Glob. J. Eng. Sci. Res*.

Slota, J., Kubit, A., Gajdoš, I., Trzepiecinski, T., Kaščák, L’. (2022). A Comparative Study of Hardfacing Deposits Using a Modified Tribological Testing Strategy. *Lubricants*, 10, 187.

Venkatesh, B., Sriker, K., Prabhakar, V.S.V. (2015). Wear characteristics of hardfacing alloys: State-of-the-art. *Procedia Mater. Sci.*

Venkatesh, B., Sriker, K., Kumar, M.A. (2020). Wear characteristics of multi layer hardfacing alloys. *AIP Conf. Proc*.

Wang, X., Han, F., Liu, X., Qu, S., Zou, Z. (2008). Microstructure and wear properties of the Fe–Ti–V–Mo–C hardfacing alloy. *Wear*.

Wang, X.H., Han, F., Liu, X.M., Qu, S.Y., Zou, Z.D. (2008). Effect of molybdenum on the microstructure and wear resistance of Fe-based hardfacing coatings. *Mater. Sci. Eng. A*

Yunqing, T., Li, D.Y. (2023). Influences of C, Si and Mn on the wear resistance of coiled tubing steel. *Wear*.

Zhao, W., Yu, K., Ma, Q., Song, Ch., Xiao, G., Zhang, H., Lv, Y., Guo, N., Li, Z. (2023). Synergistic effects of Mo and in-situ TiC on the microstructure and wear resistance of AlCoCrFeNi high entropy alloy fabricated by laser claddin. *Tribology International*.

Determining the attenuation of the UHF RFID signal for tracking the movement of particulate matter

B. Černilová[1], M. Linda[1], J. Kuře[1]

[1]Department of Electrical Engineering and Automation, Faculty of Engineering, Czech University of Life Sciences Prague, Prague, Czech Republic

Abstract

This article is concentrated on the measuring the signal attenuation of RFID tags depending on the layer of particulate matter. Three UHF RFID tags and four types of particulate matter (polypropylene, silica sand, rapeseed and soil) were used during the measurement. The aim of this article was to describe the methodology for determining the RSSI difference for tags placed under a certain layer of particulate matter. Furthermore, the aim was to determine the effect on the reading distance. The obtained results are useful for application in tracking the movement of particulate matter using the RFID technology.

Key words: UHF RFID, Movement monitoring, RFID tag, Attenuation, DEM, Particulate matter

INTRODUCTION

RFID is one of the technologies that can be used for tracking individual objects and at the same time for tracking particulate systems, and it can also be used in agricultural processes. (Charléty et al., 2022) The many advantages of RFID include, for example, small dimensions, contactlessness and ease of use. (Mikšaj & Bonefačić, 2017)

PIT RFID is often used to track particulate matter. (Allan et al., 2006) PIT RFID has very small dimensions and thus wide application possibilities. (Kayad et al., 2019) However, its significant disadvantage is the low frequencies (typically 124 kHz), which cause a low reading range, which under normal conditions reaches a maximum of 0.5 m. In contrast, ultra-frequency RFID (UHF RFID), which works on frequency 868 MHz has its reading range up to 3 m and more. (Mikšaj & Bonefačić, 2017)

The localization and tracking of objects using RFID in particulate systems is often affected by many environmental factors that can affect sensor feedback. Such factors include, for example, humidity, cover height and temperature. All this can reduce the accuracy of the localization, which is determined based on the energy loss on the antenna. (He et al., 2017)(He et al., 2017) The aim of this article is to describe the methodology for determining the RSSI difference for tags placed under a certain layer of particulate matter. Furthermore, the goal is to determine the effect on the reading distance.

MATERIALS AND METHODS

In this experiment, the amount of attenuation was determined depending on the distance from the antenna and the type of material of the particulate matter. Three types of tags were used for the measurements, which are shown in figure (Fig. 1). All tags are of the UHF RFID type. A UHF RFID antenna with a gain of 5 dBi was used for the measurement. Figure (Fig. 2 (a)) shows images of the antenna used. Figure (Fig. 2 (b)) shows the radiation characteristics of the used antenna. (*5dBi RFID UHF Anténa - ShopID*, n.d.)

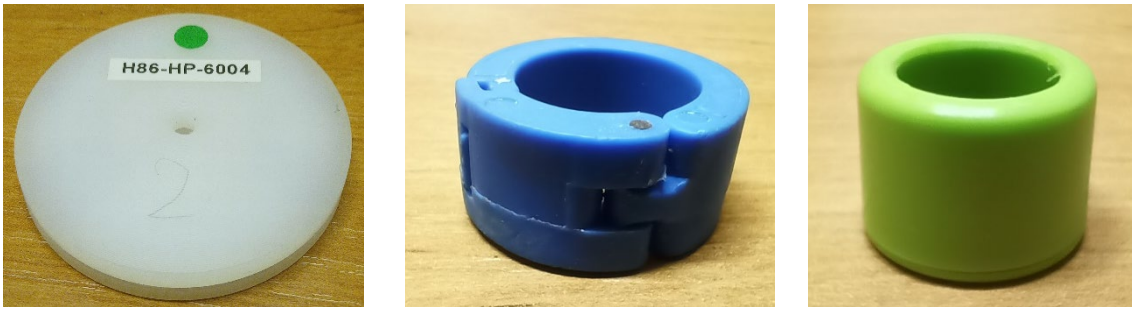

Fig. 1 Used RFID tags.

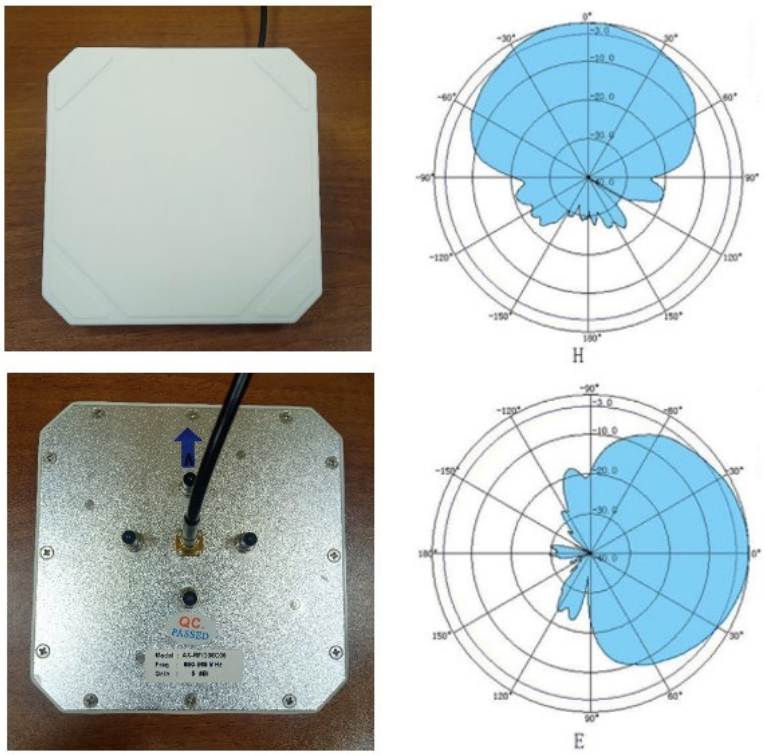

Fig. 2 (a) images of the used antenna (b) radiation characteristics of the used antenna (*5dBi RFID UHF Anténa - ShopID*, n.d.)

Four types of particulate matter were used for the measurements: polypropylene, silica sand, rapeseed and soil. The moisture content of all listed particulate matter was 0%. Particulate matter was poured into a bucket with a diameter of 260 mm and a height of 295 mm. The wall thickness of the bucket was 2 mm. Each of the listed tags was successively inserted into a bucket with a given particulate matter (Fig. 2). The tag was inserted in the center of the bucket, i.e. to a height of 147 mm and a width of 130 mm. The antenna was placed on an elevated place up to

a height of 100 mm. The antenna was placed perpendicular to the ground. The bucket was gradually moved towards the antenna and the RSSI value was determined. The RSSI value was recorded using the developed software. The measurement continued until the signal was lost. As soon as the signal began to be lost, the distance from the antenna was recorded, along with the RSSI value.

Fig. 3 Bucket used for inserting tags into particulate matter.

RESULTS AND DISCUSSION

Table (Tab. 1) shows the resulting RSSI values of three different tags depending on the threshold distances. The resulting values are further dependent on the type of particulate matter into which they were inserted during the measurement. The values always have two extremes, for the minimum distance and then for the maximum distance. The minimum distance is the same for all tags. The specified 130 mm was the placement of the tag in the center of the bucket. The maximum distance is different according to the tag used and according to the particulate matter. Figure (Fig. 4) shows a graph showing the detected distance values for the white tag inserted into soil. These values are obtained based on the RSSI values. The X-axis shows the measurement number and the Y-axis shows the measured distance.

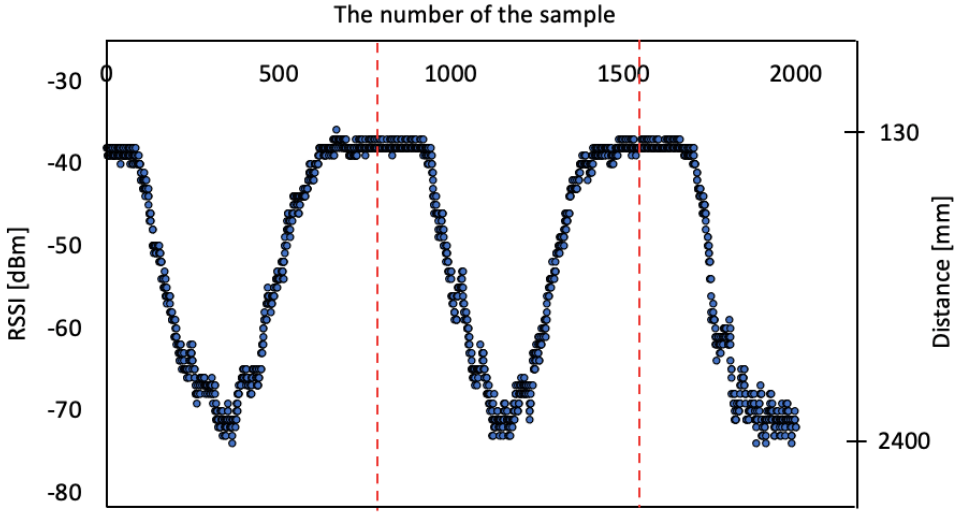

Fig. 4 The detected distance values for the white tag inserted into soil.

Some of the results showed hysteresis of maximum values during movement towards the antenna and when moving away from the antenna. Hysteresis was measured for the green tag when inserted into rapeseed and into soil. For rapeseed, the maximum distance when moving towards the antenna was 1150 mm and when moving back 1750 mm. The difference was therefore 600 mm. On the ground, this was a maximum distance of 550 mm when moving towards the antenna and 850 mm when moving back. So the difference was 300 mm. Hysteresis was measured for the blue tag when placed in rapeseed and in sand. With rapeseed, the maximum distance when moving from the antenna was 11700 mm, when moving towards the antenna, the signal began to be lost already at 2700 mm. The tag showed identical results when embedded in sand. Hysteresis was found for the white tag when inserted into polypropylene, sand and rapeseed. When moving towards the antenna, the polypropylene signal started to lose already at a distance of 2400 mm. A maximum distance of 9300 mm was measured when moving back. When moving towards the antenna, near the sand, the signal started to disappear at a distance of 2400 mm and when moving back at a distance of 6300 mm. For sand, the maximum value of the distance during the reverse movement was 8000 mm. When moving towards the antenna, this value was again 2400 mm.

Tab. 1 Values of maximum measurable distances according to the type of particulate matter. Along with that, the RSSI values are given for each measurement.

Material	Green tag		Blue tag		White tag	
	Distance [mm]	RSSI [dBi]	Distance [mm]	RSSI [dBi]	Distance [mm]	RSSI [dBi]
Polypropylene	130	-33	130	-45	130	-40
	1400	-72	1800	-84	9300	-77
Silica send	130	-46	130	-34	130	-40
	1150	-75	11700	-84	6300	-75
Rapeseed	130	-49	130	-39	130	-32
	1750	-79	11700	-84	8000	-75
Soil	130	-61	130	-45.5	130	-37
	850	-80	3000	-83	2400	-69

For a white tag inserted into the soil, an experiment was carried out to insert the tag into the back of the bucket. The tag was therefore covered with a 260 mm layer of soil perpendicular to the antenna. The maximum distance measured for this method of storage was 2400 mm. This value coincided with the maximum distance for a tag that was only covered by a 130 mm layer of soil.

CONCLUSION

The aim of this contribution was to determine the effect of a layer of particulate matter on the attenuation of the RFID signal. Using measurements, the maximum detected distances under the layer of four different particles were found. These values will be included in the RFID material library. Furthermore, the correspondence was found in the maximum measurable distance when comparing the measurements of a tag that was inserted into the soil with a cover layer of 130 mm and a cover layer of 260 mm. The results showed that the UHF RFID method is suitable for the potential tracking of particulate matter.

REFERENCES

5dBi RFID UHF anténa - ShopID. (n.d.). Retrieved August 31, 2023

Allan, J. C., Hart, R., & Tranquili, J. V. (2006). The use of Passive Integrated Transponder (PIT) tags to trace cobble transport in a mixed sand-and-gravel beach on the high-energy Oregon coast, USA. *Marine Geology*, *232*(1–2), 63–86.

Charléty, A., Le Breton, M., Larose, E., & Baillet, L. (2022). 2D Phase-Based RFID Localization for On-Site Landslide Monitoring. *Remote Sensing 2022, Vol. 14, Page 3577*, *14*(15), 3577.

He, H., Akbari, M., Sydänheimo, L., Ukkonen, L., & Virkki, J. (2017). 3D-Printed Graphene Antennas and Interconnections for Textile RFID Tags: Fabrication and Reliability towards Humidity. *International Journal of Antennas and Propagation*, *2017*.

Kayad, A., Rainato, R., Picco, L., Sartori, L., & Marinello, F. (2019). Assessing Topsoil Movement in Rotary Harrowing Process by RFID (Radio-Frequency Identification) Technique. *Agriculture 2019, Vol. 9, Page 184*, *9*(8), 184.

Mikšaj, U. T., & Bonefačić, D. (2017). Propagation characteristics of UHF radiofrequency identification system signal for application in indoor positioning. *ICECom 2016 - Conference Proceedings, 22nd International Conference on Applied Electromagnetics and Communications*.

A comparative analysis of Pump as Turbine performance characteristics measured by the PIV method and Ansys CFX simulations

J. Černý[1]

[1]*Department of Mechanical Engineering, Faculty of Engineering, Czech University of Life Sciences Prague, Prague, Czech Republic*

Abstract

This article serves as a publication of interim results leading to the innovation of the spiral casing and impeller geometry for the pump as a turbine (PAT). Validation of the Ansys CFX calculation module for the needs of the pump turbine mode was carried out using the PIV (Particle Image Velocimetry) method and by measuring values on a test circuit. The pump model was created in the Autodesk Inventor design application. The mesh for the simulations was created in Ansys Meshing with respect to the mesh quality parameters of *skewness* and *aspect ratio*. The simulation results were compared with the measured values from the test circuit, and it was found that the torque parameter is on average 1.2 Nm higher than the measured torque on the test circuit. Correction of this parameter resulted in a good match across all other parameters of the turbine performance. The velocity vectors in the suction pipe were mapped using the PIV method and the Ansys results were then compared. Lastly, the effect of the spiral casing of the original spiral and the rectangular cross-section spiral on the efficiency at the highest point of the power characteristic was subjected to comparison.

Key words: particle image velocimetry (PIV), Ansys, pump as turbine (PAT), performance characteristic

INTRODUCTION

As part of the extension of the Green Deal in the form of the 2022 REPowerEU Plan, EU countries have committed to achieve a share of renewable energy in total consumption of at least 45% by 2030 by improving energy efficiency and product eco-design. Small hydropower plants (SHPs) with a capacity of up to 10 MW are the solution for harnessing the potential of hydropower (Binama et al., 2017). With regard to the budget of SHP projects, turbines are the highest cost item. A more cost-acceptable alternative is the reverse turbine pumps (PAT), which can replace conventional small hydro turbines (Motwani et al., 2013). PATs refer to pumps running in reverse mode by inverting the flow direction and using the electric motor as a generator. The possibility of using pumps operating in turbine mode has been widely recognized since the third decade of the 20th century, but the benefits of their use in water distribution networks (WDNs) have only been pointed out recent years (Pugliese et al., 2016). The use of hydraulic pumps operating as turbines offers several advantages over conventional turbines. The main advantages are its low investment costs and market accessibility. One of the purposes for the use PAT is pressure control in water supply networks where pressure reduction valves are used (Araujo et al., 2006). The use of pressure reduction valves results in energy losses, PAT is a solution to recover this energy (Carravetta et al., 2013), (Buono et al., 2015),

(Rossi et al., 2016). Some studies report that up to 40% of the energy can be recovered in this way. (Lydon et al., 2017). PATs can also be used for energy storage, operating similarly to pumped-storage hydroelectric power plants. Førsund stated that a standard pumped storage consists of a water source (river, lake) at the location of the generator and a purpose-built reservoir at a higher altitude without any natural inflow. According to Førsund, water can be pumped into the reservoir and then released through turbines to generate electricity. Nevertheless, he pointed out that because less energy is created than the energy used by the pumps to take up the water, there is an economic problem at the heart of the pumped storage plant. As he mentioned, the fundamental requirement for pumped-storage being an economic proposition is that there must be a price difference of sufficient magnitude between periods so that the loss is overcome by the difference in price, and in addition, there is the cost of the investment in pumped storage to be covered (Førsund & Førsund, 2015). However, the ability to predict the performance of a pump as a turbine and to select the appropriate machine for a given hydropower plant is still an open question. The issue of conversion parameters between pump and turbine modes has been addressed by (Barbarelli et al., 2017) and (Polák, 2017), (Polák, 2021) in their publications. The correct methodology for solving PAT design issues plays a vital role in selecting the right pump for a particular application. Manufacturers usually do not have information on the pump's turbine mode characteristics and therefore need to determine them. In addition to measuring the performance characteristics on the test circuit, it is possible to obtain the characteristics using mathematical models.

MATERIALS AND METHODS

Verification tests were conducted on a hydraulic circuit in the fluid mechanics laboratory at the Faculty of Engineering, Czech University of Life Sciences, Prague. The circuit diagram is shown in Figure 1. The testing circuit consisted of a set of two reservoirs with pipes and control and measuring elements. With this setting, the tested PAT was measured in turbine mode. By closing the valve V2, the water flowed in the direction of the dashed arrows, while the feeding pump (FP) created the hydropower potential for the turbine. The dynamometer (D) with momentum sensor Magtrol TMB 307/41 (accuracy 0.1%) allowed continuous regulation of shaft speed via the frequency inverter LSLV0055s100-4EOFNS. This device enabled operation in motor and braking modes. The water flow was measured using an electromagnetic flowmeter (Q) SITRANS F M MAG 5100 W (accuracy 0.5%). Pressures at pp and ps were measured by pressure sensor HEIM 3340 (accuracy 0.5%) installed according to first class accuracy requirements (ČSN EN ISO 9906, 2013).

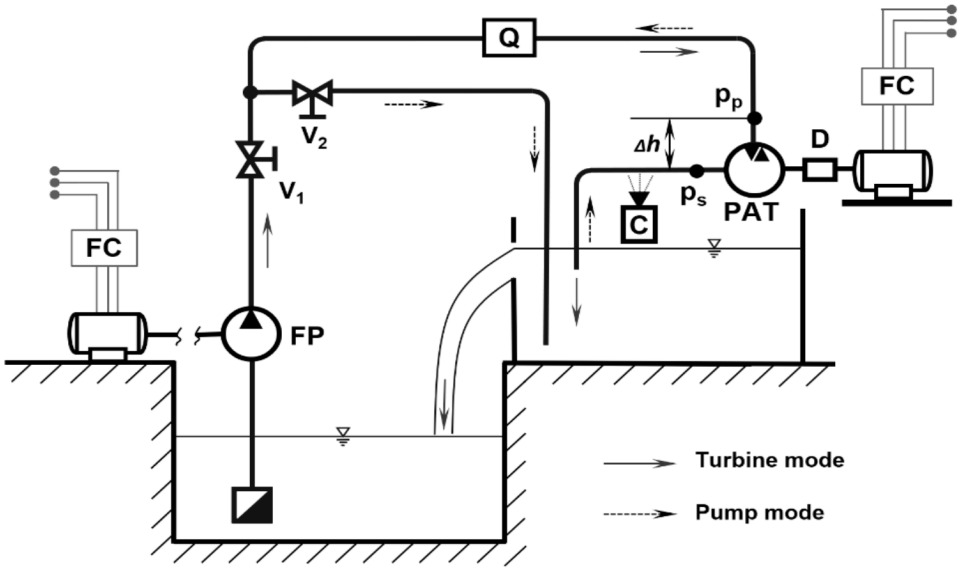

Fig. 1 Hydraulic circuit scheme for testing turbines/pumps; Q, flowmeter; FP, feed pump; PAT, pump as turbine; V1, and V2, control valves; D, dynamometer; FC, frequency inverter; C, camcoder (Polák, 2019)

A single-stage radial centrifugal cast iron pump with a spiral casing was used for the measurement. The diagram of the pump and its performance parameters guaranteed by the manufacturer is presented in Fig. 2. The evaluation tests were based on the CSN EN ISO 9906 standard providing the tests of hydrodynamic pumps. The torque was measured by a torque sensor on the shaft between the pump and the electric motor. The pressures were monitored by pressure sensors on the suction (ps) and discharge pipes (pp). The flow through the PAT was measured using a flowmeter located in front of the throttle valve.

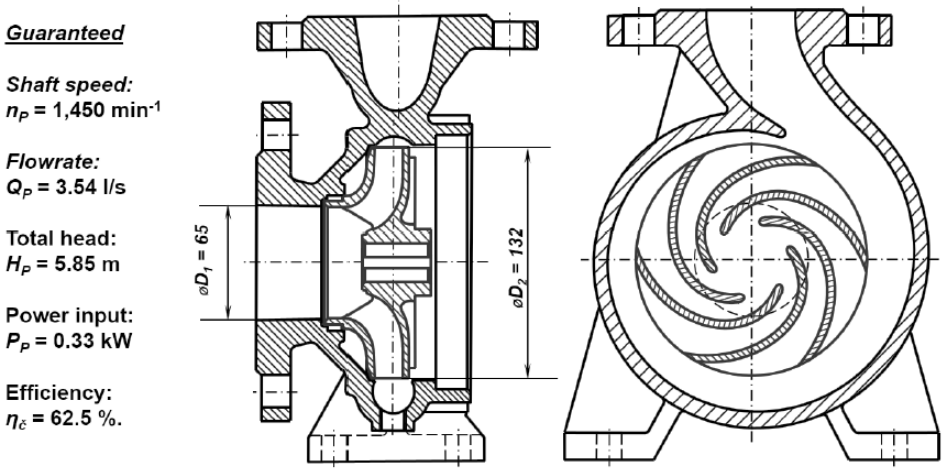

Fig. 2 Cast iron impeller in spiral casing and parameters of pump (Polák, 2019)

A 2D PIV set from the TSI company was used to measure the velocity fields in the PAT suction pipe (Fig. 3). The basis was a two-pulse Nd:YAG laser (YAG100-100-LIT) with a wave-length of 532 nm operating with an optical device Light Sheet Optics 610026 and a camera Powerview Cameras 630092. The set was completed by a synchronizer LaserPulse Model 610036 and COMPUTER for PIV 600054-64 with INSIGHT ™ 4G-2DTR Data Acquisition software. Hollow glass spheres 100-SLVR with a diameter of 12 μm, silver-coated to increase the

reflection of light on the surface were dispersed in the flowing fluid. A vertical plane in the axis of the transparent suction pipe at the PAT outlet was selected to monitor the flow (Fig. 3). A laser was placed above the pipe, repeatedly emitting two consecutive light pulses with a time delay of 50 μs. The optical system directed the emitting laser beam into a thin light sheet which illuminated the monitored area in the suction pipe. A high-speed camera positioned perpendicular to the plane scanned the area at the same frequency as the laser pulses. This was provided by the synchronizer. The images from the camera captured the positions of the fluorescent particles. The first image (t) displayed the initial positions of the particles and the second (t´) the final positions. The image processing was carried out by specialized software, which, by comparing the corresponding pairs, determined the directions and sizes of the velocity vectors of individual particles or flowing fluid. The Scilab program was used to visualize the measured data. The graphical form of the vector fields was created in this program.

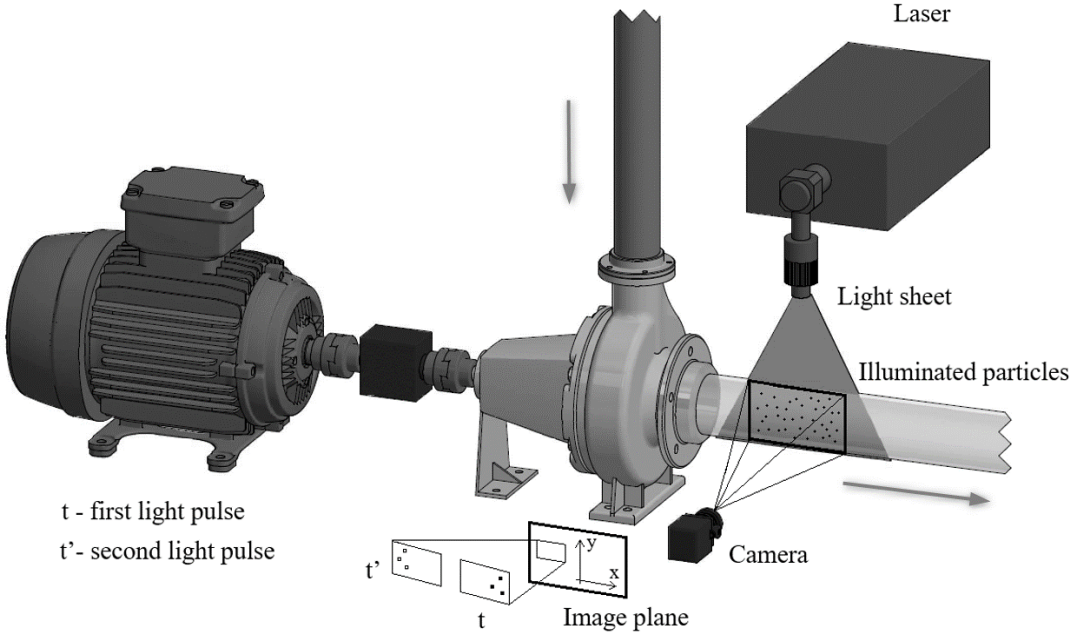

Fig. 3 Diagram of PIV method application during the experiment (Černý & Sitte, 2020)

A pump model was created to carry out simulations in Inventor. The model was further modified and prepared for simulations in Ansys CFX. In Ansys Fluent Meshing, a fine mesh with approximately 11 million elements was created for the model, meeting the quality parameter *aspect ratio* with a minimum value of 0.15 and a *skewness* parameter for a maximum value of 0.65, both of which ensure that the model is sufficiently prepared for accurate simulations. In Ansys CFX, a flow simulation was created according to previously verified methods (Černý & Polák, 2023) and compared with the values measured on the test circuit. The pressure differential and velocity values at the inlet and outlet of the model and the efficiency were selected for comparison. The model was then compared with the measured values from the PIV method. The same plane section was created as was in the PIV experiment. And the velocity values throughout turbine characteristics were compared. After the simulation was verified, the same simulation was performed with another spiral shape, except now using the rectangular-section spiral, which has the same section area as the original (Fig. 4). Here, the

highest-efficiency simulation was performed in respect to the previous simulation and the values were compared with the original spiral model.

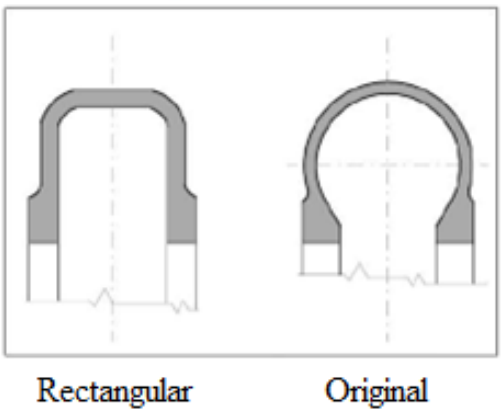

Fig. 4 Two types of cross section of the spiral casing

RESULTS AND DISCUSSION

For the measurements on the test circuit, the shaft speed and inlet pressure were adjusted using the feed pumps and throttle valve V1 (Fig. 1) to control the total head of the pump/PAT. The measurements were made for a total head of 13 [m] and 7 measurements were made for different speeds from 600 to 2400 [rpm] and for each measurement on the test circuit, a PIV measurement was also provided. Figures (Fig. 5), (Fig. 6) and (Fig. 7) show the values measured on the test circuit and compared with the values calculated using Ansys CFX. Figure 5 shows the velocities measured on the circuit at the inlet (Vp) and outlet (Vs) of the turbine. The values of A_Vs and A_Vp are the inlet and outlet velocities calculated using Ansys CFX.

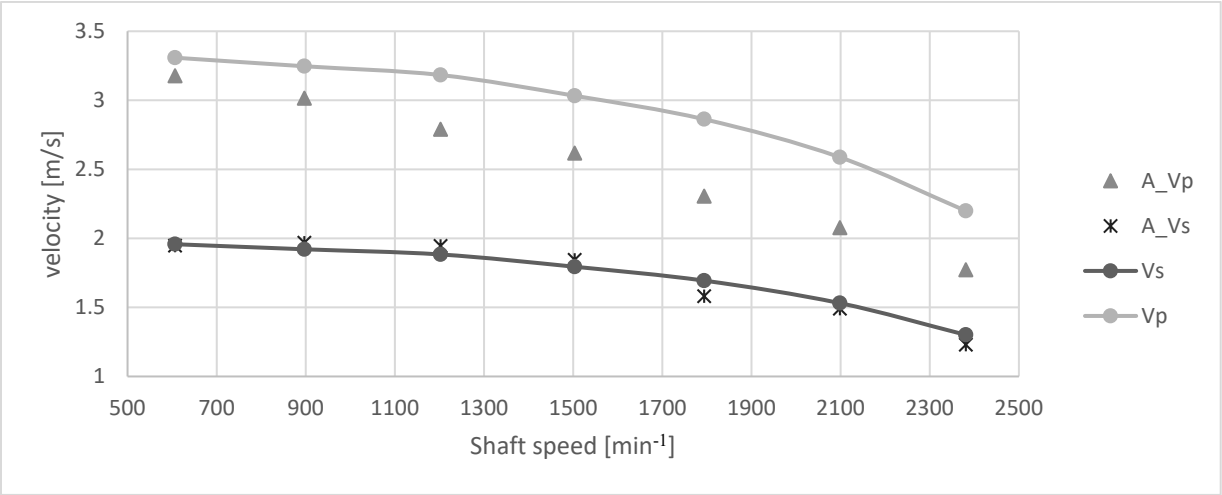

Fig. 5 The dependence of the inlet and outlet velocity on the shaft speed

The velocity values in the suction pipe (turbine outlet) are in good match, as their maximum deviation is 0.1 m/s. The velocities in the pressure pipe (turbine inlet) have a maximum deviation of 0.5 m/s.

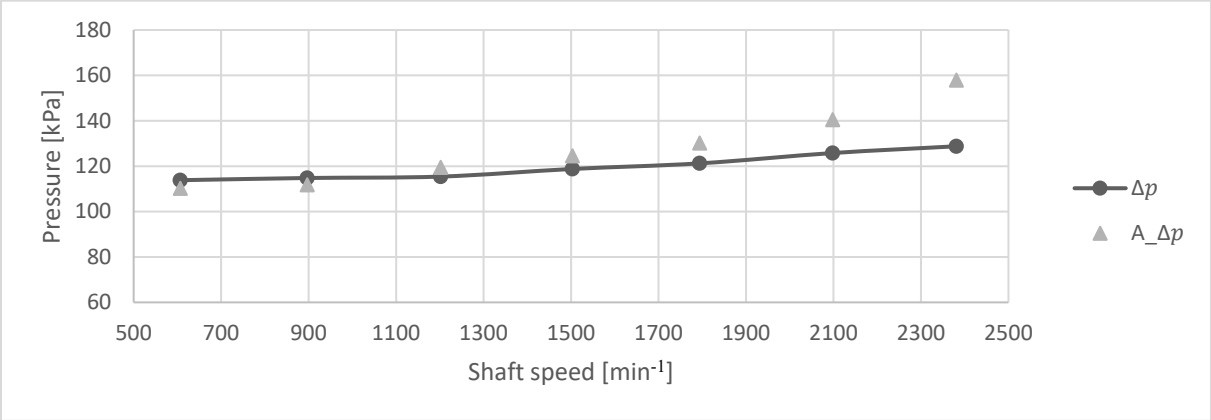

Fig. 6 Dependence of the size of pressure differential on shaft speed

Figure (Fig. 6) shows the pressure differential of the measured Δp and calculated A_Δp. The differential is an important value for the subsequent turbine characteristic calculations. The calculated values deviate significantly from the measured values at high speed where the difference between the inlet pressure and outlet pressure recorded with the two different measurement approaches reaches 30 kPa. The problematic value was the calculated torque, which was significantly higher than the measured values. Its average deviation for all measurements was 1.2 [Nm], which has a large effect on the efficiency calculation. This error can be attributed to the simplification of the blades geometry that took place due to the simplification of the calculation and the calculation module. If a correction is made for this value, the corrected efficiency (C_ηT) comes out. This corrected efficiency has a maximum deviation from the measured value of less than 5% as can be seen in figure (Fig. 7). The graph below also illustrates the efficiency measured on the test circuit (ηT) and the same value calculated using the Ansys CFX programme (A_ηT).

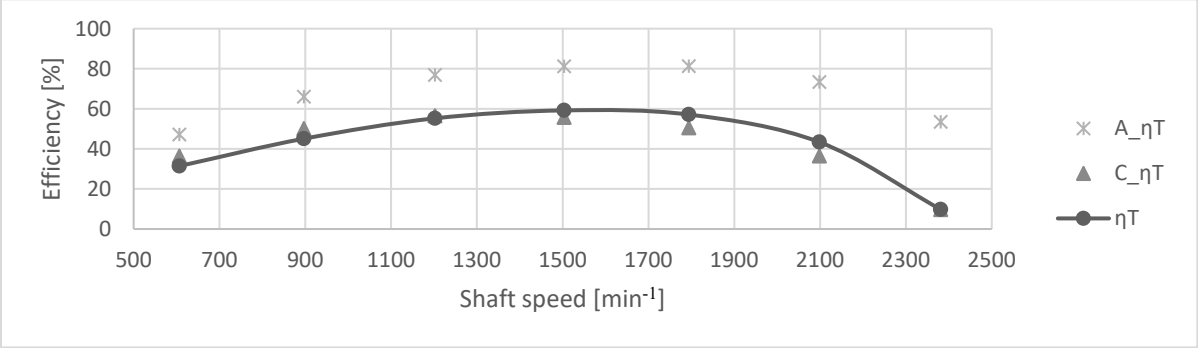

Fig. 7 Efficiency dependence on shaft speed

The next comparison is between the velocity field measured by PIV and the Ansys simulation for the 3 points with the highest turbine efficiency. In Fig. 8, the velocity field measured by PIV can be seen compared with the Ansys results for 3 different speeds which are plotted on the efficiency versus shaft speed graph as in figure (Fig. 7).

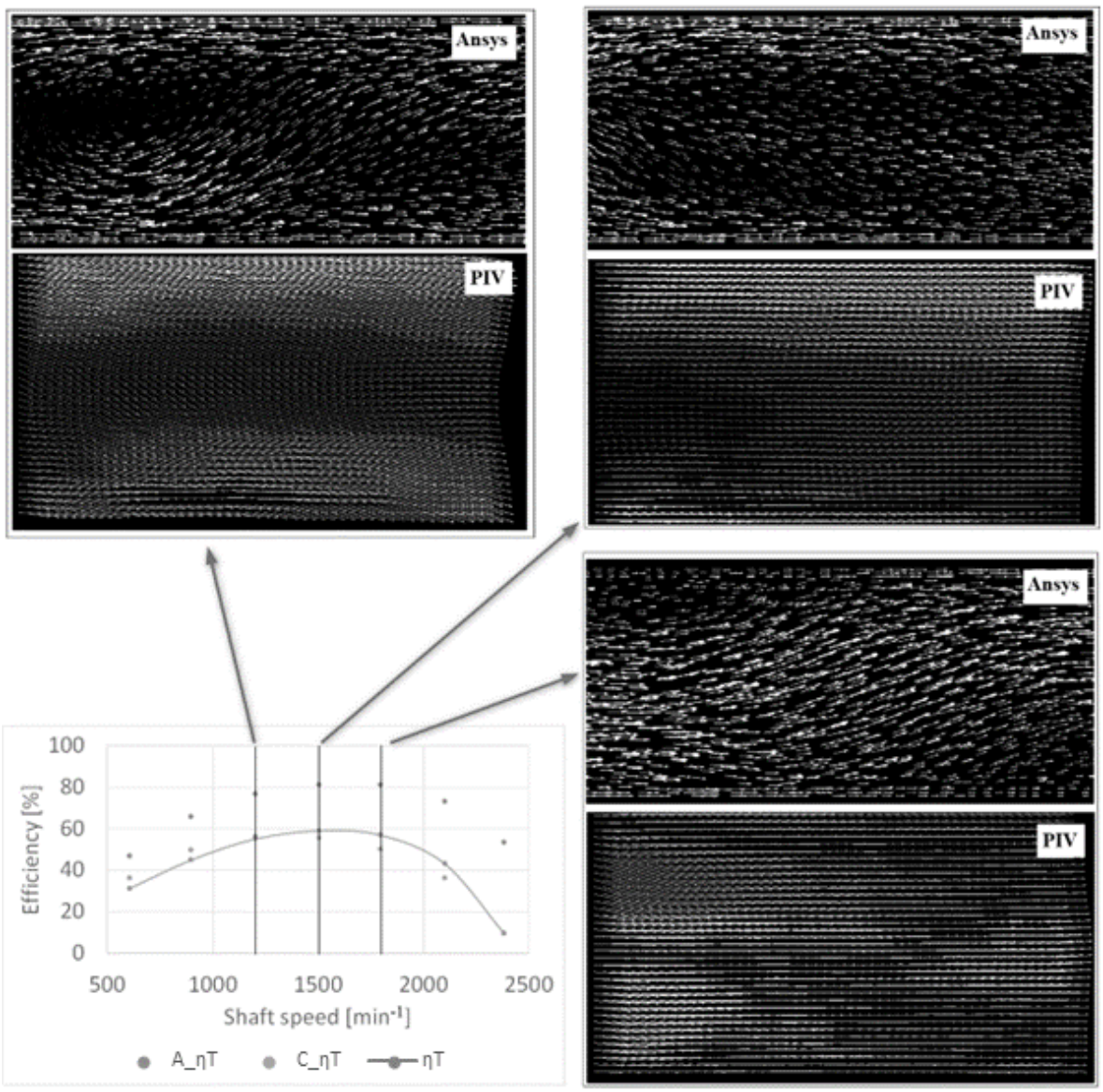

Fig. 8 Velocity field comparison, PIV vs Ansys

The PIV and Ansys measurements are in agreement in terms of the sense of vortex rotation at the PAT outlet, i.e. at lower speeds in the opposite to the direction of impeller rotation and at higher speeds in the direction of impeller rotation. At values around the optimum, i.e. measurements between 1500 rpm and 1800 rpm, the normal velocity at the pipe wall is almost zero. The dependence of the efficiency on shaft speed can be seen in figure (Fig. 9). where the value (ηT_rec) represents the efficiency of the rectangle-section spiral. The new design was calculated in Ansys. The rectangular-cross section was found to have a shifted efficiency curve compared to the original spiral in the higher speeds. The highest efficiency of the rectangular cross-section was 2% less than the original spiral. This confirms the findings of Yang et al., who have concluded that the circular shape of the spiral has the highest efficiency when compared to other types of spirals (Yang et al., 2011).

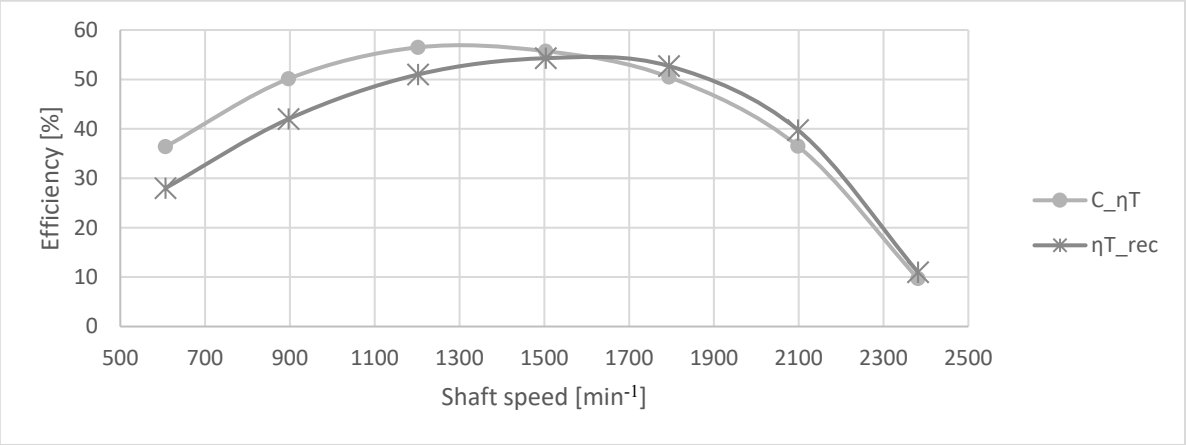

Fig. 9 Dependence of efficiency on shaft speed

CONCLUSION

The main objective was to see to what extent is Ansys CFX able to produce an accurate simulation for the Pump Turbine Mode (PAT). From the results it is evident that the values are very close to the actual measured values. The most problematic parameter is the torque, which comes out higher than the measured values – at all points by approximately the same value of 1.2 [Nm]. This error may be due to simplified geometry or the calculation module itself. After correcting the torque by the average deviation value, the rest of the results are in good agreement with the measured values. From the comparison of the vector fields created with the PIV method and those simulated in Ansys it is evident that in the point of optimal efficiency there is no significant occurrence of vortex. At lower speeds in the pipe section there is a vortex in the opposite direction to the rotation of the impeller and at the higher speeds there is a vortex shaped in the direction of the impeller rotation. The comparison of numerical models with different types of spirals revealed that the difference between highest efficiencies achieved with the different types of spirals was 2 %. The numerical model proved that the original spiral had a higher efficiency when compared to other types. The measurement is an intermediate result and the basis for a comprehensive innovative solution for the modification of the PAT spiral and subsequently the impeller.

REFERENCES

Araujo, L.S., Ramos, H. & Coelho, S.T. (2006) Pressure Control for Leakage Minimisation in Water Distribution Systems Management. *Water Resources Management*, 20 (1), 133–149.

Barbarelli, S., Amelio, M. & Florio, G. (2017) Experimental activity at test rig validating correlations to select pumps running as turbines in microhydro plants. *Energy Conversion and Management*, 149, 781–797.

Binama, M., Su, W.-T., Li, X.-B., Li, F.-C., Wei, X.-Z. & An, S. (2017) Investigation on pump as turbine (PAT) technical aspects for micro hydropower schemes: A state-of-the-art review. *Renewable and Sustainable Energy Reviews*, 79, 148–179.

Buono, D., Frosina, E., Mazzone, A., Cesaro, U. & Senatore, A. (2015) Study of a Pump as Turbine for a Hydraulic Urban Network Using a Tridimensional CFD Modeling Methodology. *Energy Procedia*, 82, 201–208.

Carravetta, A., Del Giudice, G., Fecarotta, O. & Ramos, H.M. (2013) Pump as Turbine (PAT) Design in Water Distribution Network by System Effectiveness. *Water*, 5(3), 1211–1225.

Černý, J. & Polák, M. (2023) Analysis of Fluid Flow in a Radial Centrifugal Pump. *Processes*, 11(2).

Černý, J. & Sitte, D. (2020) Analysis of the flow of liquid in the suction pipe of the radial centrifugal pump. In *Proceeding of 22nd International Conference of Young Scientists 2020*. *22nd International Conference of Young Scientists 2020*, Prague: Czech University of Life Sciences Prague.

ČSN EN ISO 9906 (2013) *Rotodynamic Pumps—Hydraulic Performance Acceptance Tests—Grades 1, 2 and 3*. Brussels, Belgium: European Committee for Standardization (110033).

Førsund, F.R. & Førsund, F.R. (2015) Pumped-storage hydroelectricity. *Hydropower Economics*, 183–206.

Lydon, T., Coughlan, P. & McNabola, A. (2017a) Pressure management and energy recovery in water distribution networks: Development of design and selection methodologies using three pump-as-turbine case studies. *Renewable Energy*, 114, 1038–1050.

Lydon, T., Coughlan, P. & McNabola, A. (2017b) Pump-As-Turbine: Characterization as an Energy Recovery Device for the Water Distribution Network. *Journal of Hydraulic Engineering*, 143(8), 04017020.

Motwani, K.H., Jain, S.V. & Patel, R.N. (2013) Cost Analysis of Pump as Turbine for Pico Hydropower Plants – A Case Study. *Chemical, Civil and Mechanical Engineering Tracks of 3rd Nirma University International Conference on Engineering (NUiCONE2012)*, 51, 721–726.

Polák, M. (2017) Experimental evaluation of hydraulic design modifications of radial centrifugal pumps. *Agronomy Research*, 15, 1189–1197.

Polák, M. (2019) The Influence of Changing Hydropower Potential on Performance Parameters of Pumps in Turbine Mode. *Energies*, 12(11).

Polák, M. (2021) Innovation of Pump as Turbine According to Calculation Model for Francis Turbine Design. *Energies*, 14(9).

Pugliese, F., De Paola, F., Fontana, N., Giugni, M. & Marini, G. (2016) Experimental characterization of two Pumps As Turbines for hydropower generation. *Renewable Energy*, 99, 180–187.

Rossi, M., Righetti, M. & Renzi, M. (2016) Pump-as-turbine for Energy Recovery Applications: The Case Study of An Aqueduct. *Energy Procedia*, 101, 1207–1214.

Yang, S., Kong, F. & Chen, B. (2011) Research on Pump Volute DesignMethod Using CFD. *INTERNATIONAL JOURNAL OF ROTATING MACHINERY*, 2011.

Optimization of extrusion filament production line for additive manufacturing

P. Jirků[1]

[1]*Department of Material Science and Manufacturing Technology, Faculty of Engineering, Czech University of Life Sciences Prague, Prague, Czech Republic*

Abstract

This article focuses on the optimization of 3D printing filament production. It discusses the possibilities and needs of additive manufacturing. It describes the principle of material deposition using FDM technology and explains the requirements for the filaments used. Describes the process of extrusion of polymer filaments for use in additive technologies. The optimization of the extrusion line at CZU is described. This includes nozzle optimization, fitting of the necessary electronics and laser measuring system.

Key words: 3D printing, additive manufacturing, filament, extrusion, PLA, nozzle

INTRODUCTION

The concept of additive manufacturing (AM), which is often also referred to as rapid prototyping (RP), is mainly driven by 3D printing. In 3D printing, the basic principle is to apply material layer by layer. In this way, complex parts can be created, usually with small sizes and low production runs. Other advantages include a very low percentage of waste, as only the part being produced can be created directly without the need for moulds or the generation of large amounts of waste chips, as is the case with subtractive technologies (turning and milling) (Arockiam et al., 2022), (Cosmi & Dal Maso, 2020), (Daminabo et al., 2020). Over time, the demand for lightweight, functional and cost-effective parts with polymers and polymer-based composites has increased. This pressure has led to a growing industry of polymer-based materials for additive technologies (Gao et al., 2015), (González et al., 2017), (Scheithauer et al., 2015). 3D printing technologies can be classified into several categories, mainly based on the method of material deposition and the type of material used. The materials are the aforementioned polymers, metals in powder form, photosensitive resins, etc. This article focuses on FDM 3D printing technology where thermoplastic polymers are the main material used. FDM is one of the most widely used technologies in additive manufacturing (Daminabo et al., 2020). For use on a 3D printer, material in the form of filament is used. The most used materials are PLA, PET-G and ABS polymers (Hafsa et al., 2014). For FDM technology, thermoplastics are used, as the manufacturing process is based on the principle of heating the material to be deposited (reactive plastics do not allow repeated shape changes) (Turner et al., 2014), (Vyavahare et al., 2020). The raw material used is supplied in the form of a filament on a spool. In the print head of the 3D printer, the thermoplastic polymer filament is gradually

heated and sequentially deposited using a nozzle. The filament here acts like a piston, where the rigid part pushes outwards from the nozzle the part that is already heated and softened. Therefore, the polymer filament has certain viscosity and stiffness requirements to achieve continuity in the material flow area during extrusion (Liu et al., 2017), (Singamneni et al., 2021).

MATERIALS AND METHODS

For the optimization was selected extrusion line Jwell JWS35/25, which is part of the property of the Department of Materials and Engineering Technology at the Technical Faculty of the Czech University of Agriculture in Prague. It was modified with necessary components for the needs of filament extrusion applicable in the field of FDM 3D printing. These are in particular the extruder nozzle. It was made in two variants.

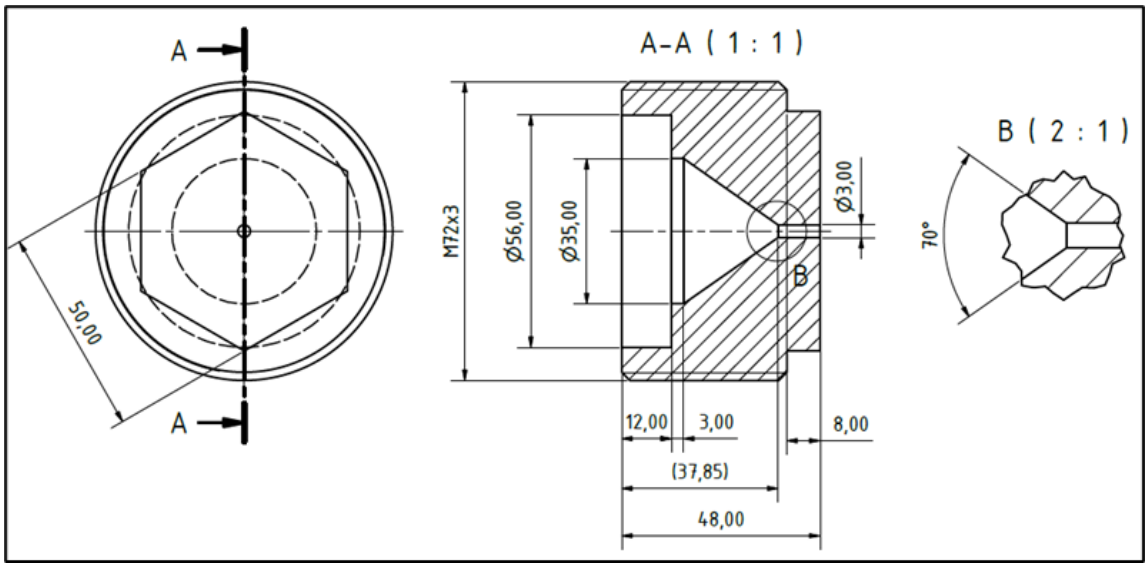

Fig. 1 Technical drawing of the nozzle

Figure (Fig.1) shows a drawing of the first variant. This nozzle was created with a tapered outlet with a diameter of 3 mm. For variability, nozzle No.2 was also made with an interchangeable tip. This makes it unnecessary to dismantle the entire extrusion line head when changing to a different diameter. Figure (Fig. 2) shows the exchangeable nozzles with 2 mm and 4 mm inner diameters. The material chosen for the nozzles is stainless steel DIN 1.4301.

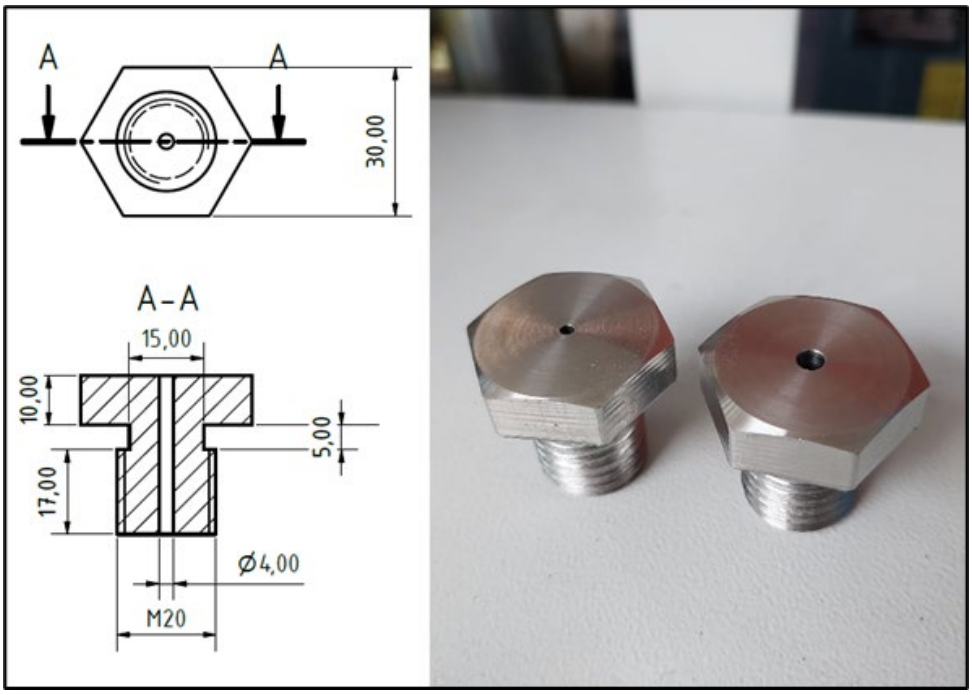

Fig. 2 Exchangeable extruder nozzles.

Furthermore, the unwinding system has been modified to allow precise adjustment of the filament "pulling" speed. During extrusion of the material, two basic variables are set: the speed of rotation of the extruder screw (extrusion) and the speed of pulling out the already cooled filament by the unwinding system. To achieve the optimum material flow through the nozzle and the desired diameter of the resulting filament, these values must be adjusted relative to each other. For this reason, the filament production line was further modified. It was equipped with an optical sensor L-LAS-TB-AL Series from Sensor Instruments. This device allows the filament diameter to be monitored during production. Thanks to this, the machine operator can react flexibly and adjust the optimum value for the filament diameter to a standardized value of 1.75 mm by controlling the speed of the extrusion screw. The test batches of filament produced contained a slight variation in circularity and did not cause printing errors that filament with an ovality outside the permissible limit could produce (material jamming, sudden change in flow). For the purpose of filament production, the line was divided into 4 basic sections: heating of material by screw and extrusion through nozzle (extrusion line); cooling section in the overflow chute; material drying section (blowing residual water off the filament surface); unwinding system (pulling the material out at a set speed and then winding it onto the spool). Figure (Fig. 3) shows the process of filament formation on a Jwell JWS35/25 extrusion line. After leaving the extruder nozzle, the material was fed into a water bath where it was cooled and passed through a drying section to be measured and wound onto a spool in the form of a string.

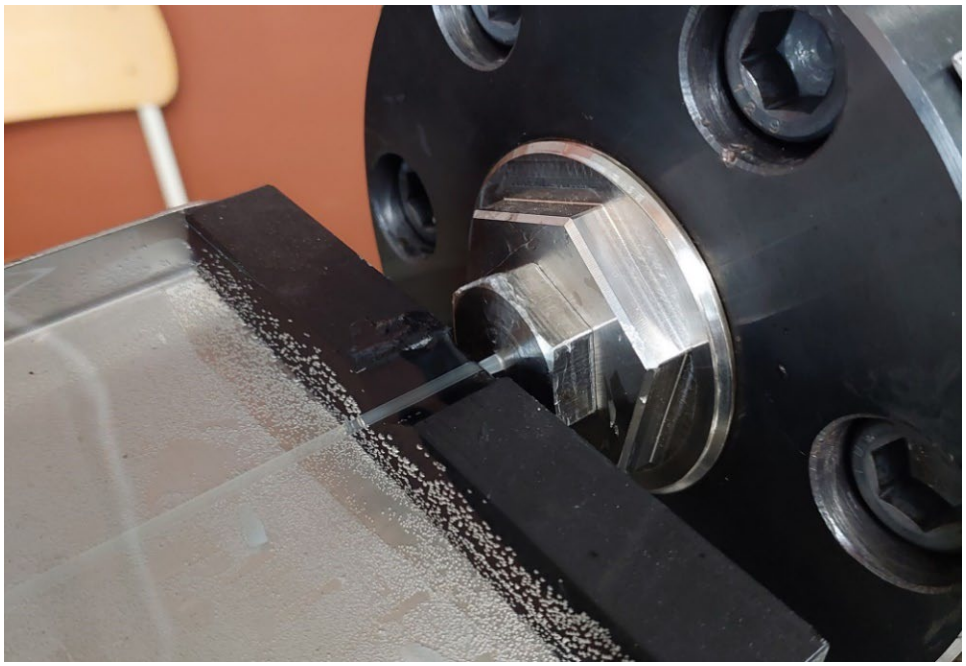

Fig. 3 Filament production on the Jwell JWS35/25 extrusion line

RESULTS AND DISCUSSION

During extrusion, the fibre diameter was measured and recorded using L-LAS-TB-Scope V5.4.5. Figure 4 shows the values of the measured diameters over time. The value was recorded for 60 seconds at an interval of one second each time. After setting the optimum speed of the extruder screw and extractor, the values ranged from 1733 µm to 1769 µm.

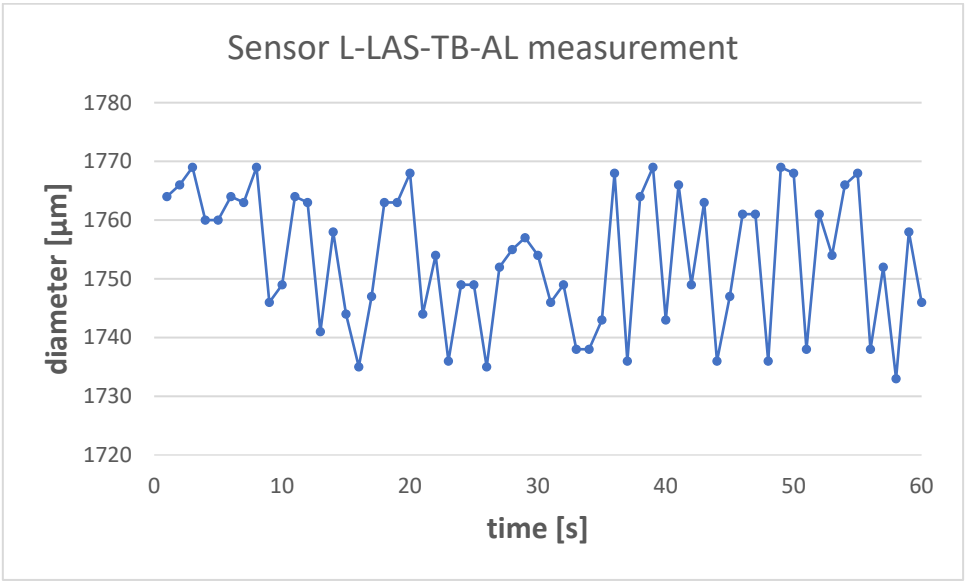

Fig. 4 Measured amounts of mechanical characteristic of rapeseeds pressed mixtures and their fitted functions.

A series of samples were then printed from the filament on a Prusa IMK3S 3D printer. These were mainly calibration bodies on which changes in flow and printing errors could be observed. A calibration cube with defined XYZ dimensions of 20x20x20 mm was printed. Figure 5 shows a calibration cube with the following dimensions printed: X = 19.9 mm, Y = 19.85 mm and Z = 20 mm. This slight deviation may be due to printer inaccuracy.

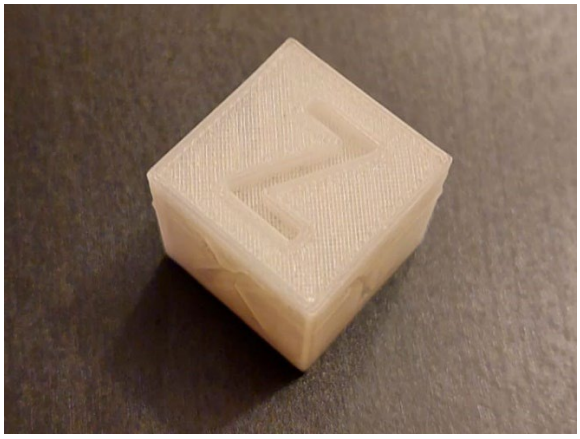

Fig. 5 Calibration cube

CONCLUSION

The polylactic acid filament formed on the modified extrusion line performed well when used on a 3D printer. It did not cause jamming in the print head, nor did it cause significant diameter changes that would be picked up by the laser thickness sensor and reflected on the printed calibration cube. In the future, an extrusion filament production line may be used for additive manufacturing applications. The disadvantage of the extrusion line investigated is its size, which is not suitable for laboratory use as a large amount of material is consumed in starting the line when it is shut down. If the material were allowed to cool in the extruder screw, it could cause jamming in the melt zone, requiring dismantling of the line.

REFERENCES

Arockiam, A. J., Subramanian, K., Padmanabhan, R. G., Selvaraj, R., Bagal, D. K., & Rajesh, S. (2022). A review on PLA with different fillers used as a filament in 3D printing. *Materials Today: Proceedings*, *50*, 2057–2064.

Cosmi, F., & Dal Maso, A. (2020). A mechanical characterization of SLA 3D-printed specimens for low-budget applications. *Materials Today: Proceedings*, *32*, 194–201.

Daminabo, S. C., Goel, S., Grammatikos, S. A., Nezhad, H. Y., & Thakur, V. K. (2020). Fused deposition modeling-based additive manufacturing (3D printing): techniques for polymer material systems. *Materials Today Chemistry*, *16*, 100248.

Gao, W., Zhang, Y., Ramanujan, D., Ramani, K., Chen, Y., Williams, C. B., Wang, C. C. L., Shin, Y. C., Zhang, S., & Zavattieri, P. D. (2015). The status, challenges, and future of additive manufacturing in engineering. *Computer-Aided Design*, *69*, 65–89.

González, C., Vilatela, J. J., Molina-Aldareguía, J. M., Lopes, C. S., & LLorca, J. (2017). Structural composites for multifunctional applications: Current challenges and future trends. *Progress in Materials Science*, *89*, 194–251.

Hafsa, M. N., Ibrahim, M., Wahab, M. S., & Zahid, M. S. (2014). Evaluation of FDM pattern with ABS and PLA material. *Applied Mechanics and Materials*, *465–466*, 55–59.

Liu, X., Chi, B., Jiao, Z., Tan, J., Liu, F., & Yang, W. (2017). A large-scale double-stage-screw 3D printer for fused deposition of plastic pellets. *Journal of Applied Polymer Science*, *134*(31), 45147.

Scheithauer, U., Schwarzer, E., Richter, H. J., & Moritz, T. (2015). Thermoplastic 3D Printing—An Additive Manufacturing Method for Producing Dense Ceramics. *International Journal of Applied Ceramic Technology*, *12*(1), 26–31.

Singamneni, S., Behera, M. P., Truong, D., Le Guen, M. J., Macrae, E., & Pickering, K. (2021). Direct extrusion 3D printing for a softer PLA-based bio-polymer composite in pellet form. *Journal of Materials Research and Technology*, *15*, 936–949.

Turner, B. N., Strong, R., & Gold, S. A. (2014). A review of melt extrusion additive manufacturing processes: I. Process design and modeling. *Rapid Prototyping Journal*, *20*(3), 192–204.

Vyavahare, S., Teraiya, S., Panghal, D., & Kumar, S. (2020). Fused deposition modelling: a review. *Rapid Prototyping Journal*, *26*(1), 176–201.

Influence of additive carbide-forming elements on the microstructure of Fe-B-C alloys

L. Křivánková[1], R. Chotěborský[1], M. Linda[2]

[1]*Department of Material Science and Manufacturing Technology, Faculty of Engineering, Czech University of Life Sciences Prague, Prague, Czech Republic*

[2]*Department of Electrical Engineering and Automation, Faculty of Engineering, Czech University of Life Sciences Prague, Prague, Czech Republic*

Abstract

This article describes the method of preparing samples for the subsequent investigation of the effect of selected additive elements (Cr, V, W) on the basic Fe-B-C alloy. The influence of additional elements on the microstructure of alloys was determined based on a literature search on the given issue and calculations in SW JMat. The size of the bets was calculated in the designed SW LenBorka. According to the findings and calculations in the software, the alloys were cast in an induction furnace and samples were prepared for subsequent microstructural analysis.

Key words: chemical composition, microstructure, Fe – B – C alloys, vanadium, tungsten

INTRODUCTION

Knowledge of the effect of microstructure due to additive elements is the basis for research and subsequent development of new wear-resistant materials. Correctly designing the microstructure of Fe – B – C alloys increases resistance to abrasive wear. Currently, agricultural tools are made from several types of materials. Basic steels used for the manufacture of agricultural tools include manganese steel, high nickel alloy steel and chromium alloy steel. However, the content of alloying elements is high, therefore Fe – B – C alloys appear to be a promising material that can be used to produce agricultural tools (Sang et al. 2015), (Tian et al., 2019), (Guo et al., 2003), (Bhakat et al., 2007).The borides in the structure form a framework that is resistant to wear, especially for Fe – Cr – B and Fe – B – C alloys. Already 0.001 wt. % B leads to an increase in hardenability of steel. However, the solubility of boron in iron is very limited and the addition of excessive amounts of boron leads to the formation of a continuous network of eutectic boride M2B (M represents Fe, Cr or Mn) along the grain boundaries, which adversely affects the mechanical properties and leads to embrittlement of Fe – B – C alloys with high boron content (Sang et al., 2015), (Zhang et al. 2019), (Fu et al., 2007). A significantly lower amount of added boron (supplemented by low additions of other chemical elements – Cr, W, V) enables the production of higher quality iron alloys than using a significant amount of traditional alloying elements (Chotěborský et al.,2008), (Chotěborský et al., 2013), (Sabet et al. 2011).. One of the main advantages of Fe – B – C alloys is their

structure, corresponding to metal matrix composites (MMC) (Zhang et al., 2019), (Fu et al., 2007). Vanadium, as well as tungsten form hard MC carbides, due to their low solubility in engineering alloys, they remain relatively pure. However, these carbides are harder than precipitated chromium carbides (commonly used in wear-resistant alloys) and are suitable as alternative hard phases.

MATERIALS AND METHODS

The casting was preceded by batch calculations. The weight of one batch per casting was calculated according to the size of the casting mold up to 500g. This is to create a casting of sufficient volume to produce the required number of samples for microstructure examination and subsequent sample preparation (for heat treatment and wear resistance tests). The optimal amount (mass content) of additive chemical elements in basic alloys was determined by a literature search of previous research in this issue. SW JMat was used to create CCT diagrams, TTT diagrams and phase transformations presented in figure (Fig. 1).

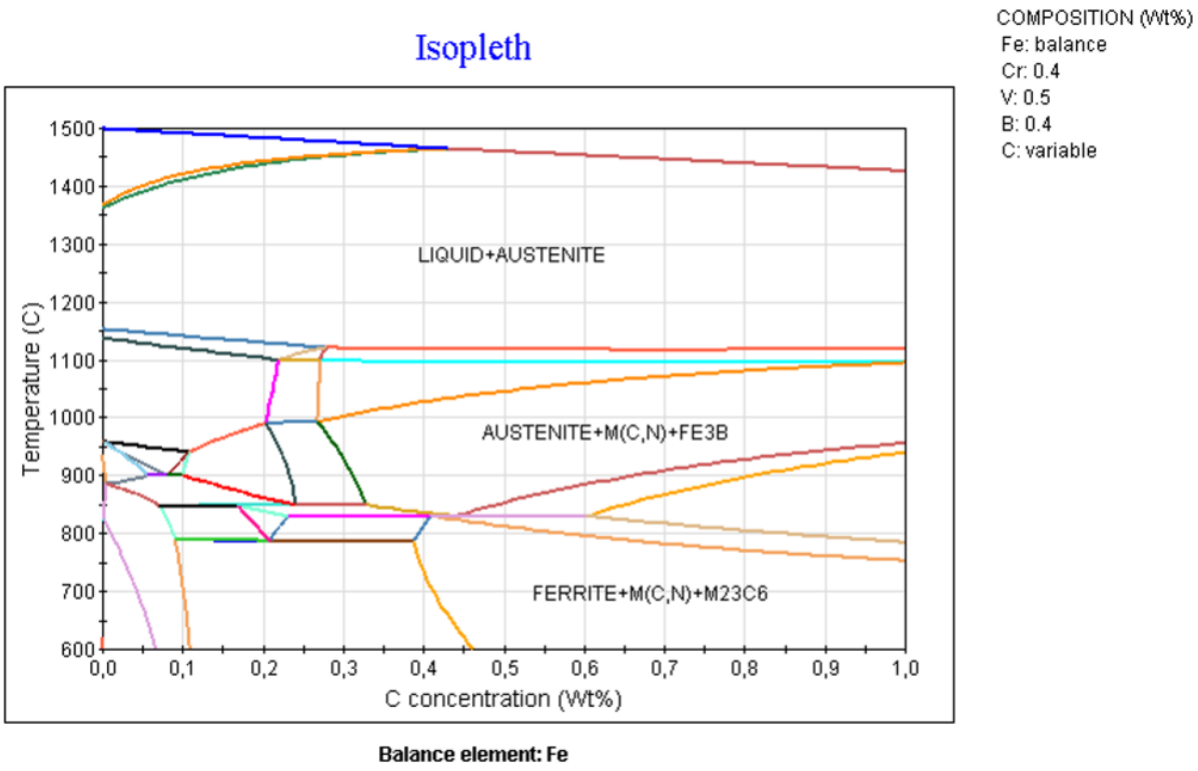

Fig. 1 Phase diagram from SWJMat

The mass content of carbon and boron in the base alloy was determined to be approximately 0.3 wt. % C and 0.4 wt. % B. A total of eight batches of chemical composition were prepared, the chemical composition of which is shown in table (Tab.1).

Tab. 1: Chemical composition of batches

Experiment	C (wt. %)	B (wt. %)	Cr (wt. %)	V (wt. %)	W (wt. %)
E1	0.4	0.3	0.4	0	0
E2	0.4	0.3	1	0	0
E3	0.4	0.3	0.4	0.5	0
E4	0.4	0.3	1	0.5	0
E5	0.4	0.3	0.4	0	0.5
E6	0.4	0.3	1	0	0.5
E7	0.4	0.3	0.4	0.5	0.5
E8	0.4	0.3	1	0.5	0.5

C35 steel (diameter 30 mm) was first descaled and cut into cylinders of 95 mm length, these cyllinders were weighed (Fig.2). The determined weight of these cylinders was entered into SW Lenborka. which can calculate the required weight composition in grams of added ferroalloys. Based on this calculation, ferroalloys were also weighted (Fig. 3).

Fig. 2 C35 steel cylinders

Fig. 3 Weighted ferroalloys

Weighted ferroalloys together with steel were melted in a VTC 200 V induction furnace. The graphite casting mold was preheated to 200 °C. Subsequently, casts were created (Figure 4). Parts were cut from these castings, which were then cast in acrylic resin with DuroCit Powder filler mixed with Durocit Liquid I and II. After the resin had cured, the sample was ground with a diamond wheel (Struers - MD Piano 220) with water and a diamond wheel (Struers - MD Alegro) with a water-based diamond suspension of 9 µm. The next step was to polish the sample with a wheel (Struers – MD Dac) with a DP-Dac 3 µm water-based diamond suspension. The last step is to polish the sample with a disc (Struers – MD Chem) OP-S colloidal suspension Al2O3 0.05 µm. The finished samples prepared for microstructural analysis are shown in Figure 5. The rest of the casting will later be processed for other samples to be heat treated and subjected to wear resistance tests.

Fig. 4 Casts E1, E2, E3

Fig. 5 Metallographic samples

RESULTS AND DISCUSSION

After polishing the samples, the cleanliness of these samples was examined, images were taken on a Zeiss AxioCam optical microscope at 200x and 500x magnification, black areas on the grain boundaries were detected, which will subsequently be detected on an electron microscope. A step followed, etching the samples to determine the microstructure. The samples were etched with Nital solution for approximately 30 seconds. Subsequently, the samples were again examined under a microscope and images were created at 200x and 500x magnification. In the sample E1, martensite, bainite and a small amount of granular pearlite were detected. A ferritic-bainitic microstructure was found in sample E2, the ferrite is soft, acicular. The last sample E3 shows a ferritic-pearlitic microstructure. Perlite is soft, partly globular. Borides are reticulate.

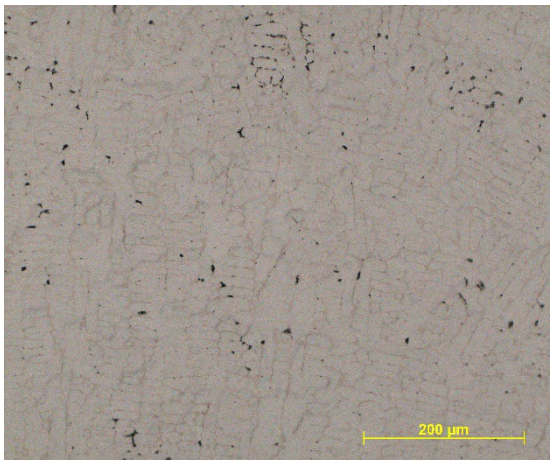

Fig. 7 Sample E1 before etching (mag. 200x)

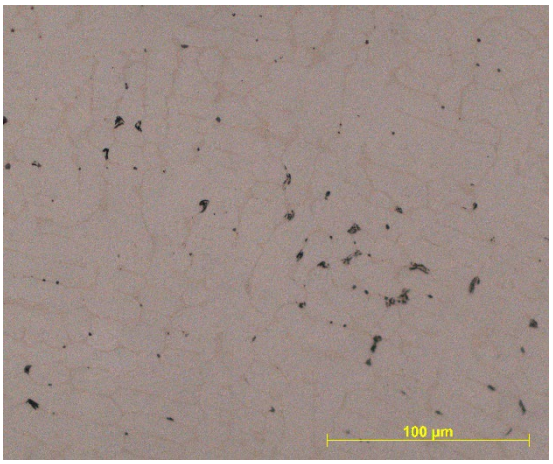

Fig. 8 Sample E1 before etching (mag. 500x)

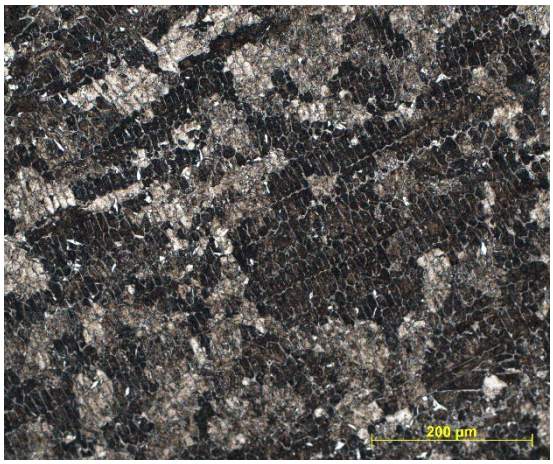

Fig. 9 Cellular microstructure of sample E1, (mag. 200x)

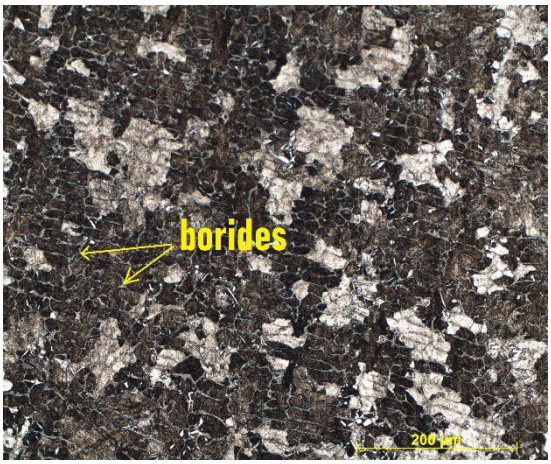

Fig. 10 Cellular microstructure of sample E1, martensite, bainite, granular pearlite (mag. 500x),

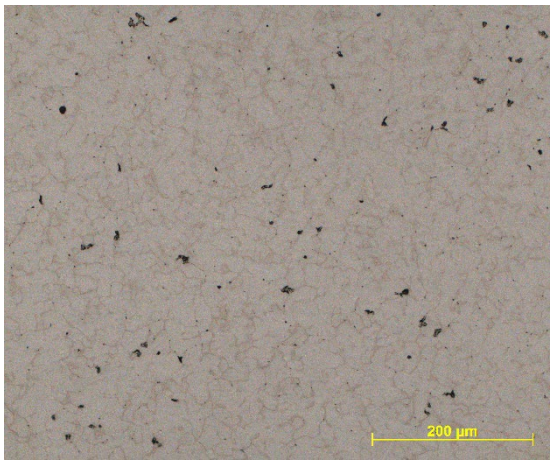

Fig. 11 Sample E2 before etching (mag. 200x)

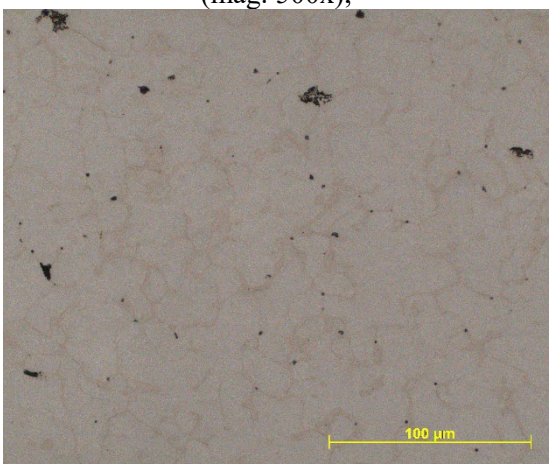

Fig. 12 Sample E2 before etching (mag. 500x)

Fig. 13 Microstructure of sample E2 (mag. 200x)

Fig. 14 Microstructure of sample E2, ferrite, bainite, (mag. 500x),

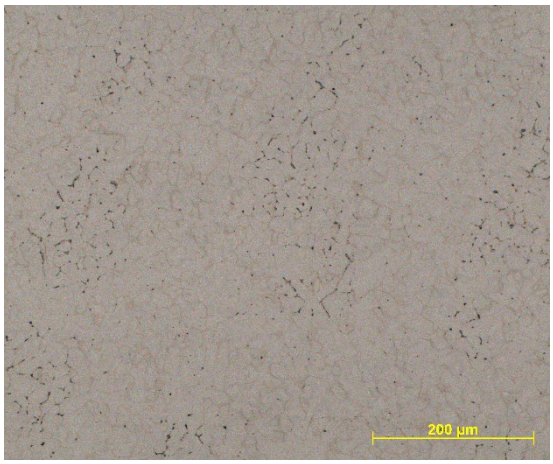

Fig. 15 Sample E3 before etching (mag.200x)

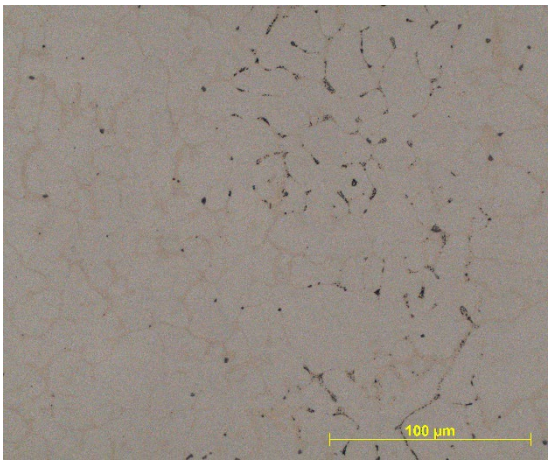

Fig.16 Sample E3 before etching (mag.500x)

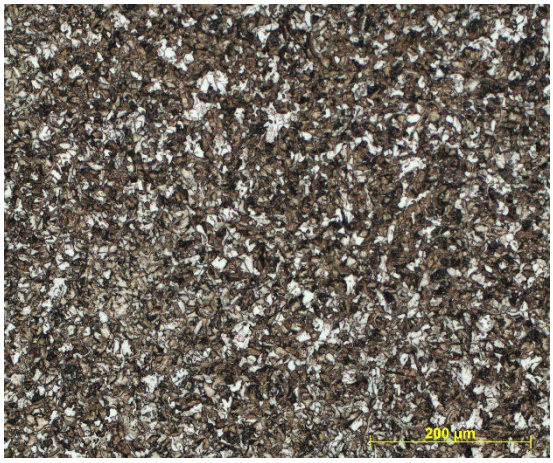

Fig. 17 Microstructure of sample E3, magnification 200x

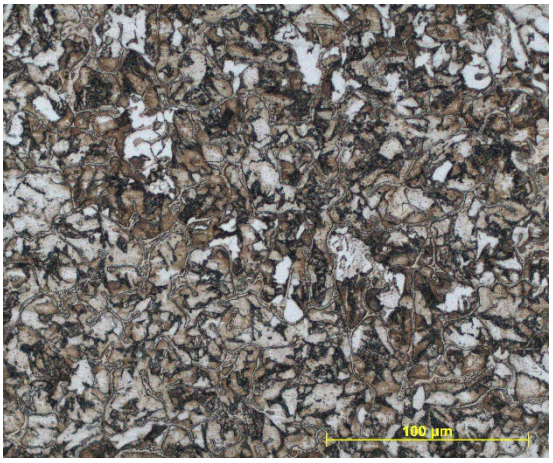

Fig. 18 Microstructure of sample E3, magnification 500x, ferrite, pearlite

After microstructural analysis, the hardness of all samples was measured on a Vickers hardness tester (HV 30), presented in table (Tab. 2). It was found that the sample where only chromium (wt. 4%) was added to the steel had the smallest hardness, the E2 sample with a higher mass content of chromium (wt. 1%) showed greater hardness, and the greatest hardness was found in the E3 sample, where in addition to chromium (wt. 0.4%), vanadium (wt. 0.5%) is also added. This experiment therefore points to the fact that adding a smaller amount of an additive element (vanadium) can improve the mechanical properties of steel than adding a large amount of commonly used alloys.

Tab. 2 Measured hardness of the samples

Vickers hardness test	HV 30 (E1)	HV 30 (E2)	HV 30 (E3)
1.	288	309	413
2.	287	312	422
3.	282	311	427
Average value	**286**	**311**	**420**

CONCLUSION

The rest of the soldered batches will still be cast and finally all the microstructures will be compared to each other. In Figure 18, the borides are not well visible, so further research will also focus on finding another etching method to clearly separate the borides from the matrix. With this step, it will be possible to subsequently use SW to measure cells. The determined value will be used to correct the calculations in SW JMat. Next, the casting samples will be heat-treated and annealed, which will once again create new microstructures that can be etched in a different way.

ACKNOWLEDGEMENT

This study was supported by Internal Grant Agency 31140/1312/3107 of Faculty of Engineering, Czech University of Life Sciences in Prague – Influence of additive carbide-forming elements on the microstructure of Fe-B-C alloy.

REFERENCES

Sang, P. et al. (2015) 'Effect of boron concentration on solidification structure and hardness of Fe-B-C wear-resistant alloy', *Materialwissenschaft und Werkstofftechnik, 46(9), pp. 962–969*.

Tian, Y. et al. (2019) 'Effect of Chromium Content on Microstructure, Hardness, and Wear Resistance of As-Cast Fe-Cr-B Alloy', *Journal of Materials Engineering and Performance, 28(10), pp. 6428–6437*.

Guo, C. and Kelly, P. (2003) 'Boron solubility in Fe–Cr–B cast irons', *Materials Science and Engineering: A, 352(1), pp. 40–45.*

Bhakat, A. K., Mishra, A. K. and Mishra, N. S. (2007) 'Characterization of wear and metallurgical properties for development of agricultural grade steel suitable in specific soil conditions', *Wear, 263(1-6 SPEC. ISS.), pp. 228–233.*

Chotěborský, R. et al. (2008) 'Abrasive wear of high chromium Fe-Cr-C hardfacing alloys', *Research in Agricultural Engineering, 54(4), pp. 192–198.*

Chotěborský, Rostislav; Bryksí-Stunová, Barbora; Kolaříková, M. (2013) 'Effect of rare earth element on microstructure of Fe-B cast alloy', *22nd International Conference on Metallurgy and Materials, METAL 2013. TANGER Ltd., pp. 203–207.*

Zhang, J. et al. (2019) 'A review on relationship between morphology of boride of Fe-B alloys and the wear/corrosion resistant properties and mechanisms', *Journal of Materials Research and Technology, 8(6), pp. 6308–6320.*

Fu, H., Zhou, Q. and Jiang, Z. (2007) 'A study of the quenching structures of Fe-B-C alloy', *Materialwissenschaft und Werkstofftechnik, 38(4), pp. 299–302.*

Shibe, V. and Chawla, V. (2018) 'Characterization of Fe–C–Cr Based Hardfacing Alloys', *Transactions of the Indian Institute of Metals, 71(9), pp. 2211–2220*.

Sabet, H. et al. (2011) 'The microstructure and abrasive wear resistance of Fe-Cr-C hardfacing alloys with the composition of hypoeutectic, eutectic, and hypereutectic at Cr/C 6', *Tribology Letters, 44(2), pp. 237–245.*

Possibilities of determining the size of wood chips using image analysis.

M. Maděra[1], F. Kumhála[1]

[1]Department of Agricultural Machines, Faculty of Engineering, Czech University of Life Sciences Prague, Prague, Czech Republic

Abstract

This thesis examines the possibilities of evaluating the quality of wood chips that are used to produce electricity or heat. One of the latest methods for evaluating the quality of wood chips is carried out by a method based on the image analysis of a color photograph. The software adjusts the photo in grayscale, followed by radial optical distortion correction. Using the brightness histogram, we determine the threshold values, and then the photo is converted to a binary image, from which the size of the measured particles is converted from pixels to millimeters according to the number of pixels. With this method, only the surface of the sample can be examined, therefore multiple photographs of the given sample must be taken. In our case, 5 measurements of one sample were performed. Thanks to the use of the software, we are able to determine the size of the fraction of the examined sample of wood chips in a matter of minutes. The work uses the Sedimetrics digital Gravelometer software, developed by researchers from Loughborough University and published by MALTAB®.

Key words: image analysis, woodchips, quality, fraction, measurements

INTRODUCTION

Combustion equipment for solid biomass - from kilowatt furnaces for heating homes to combined production of heat and electricity in the order of megawatts, suffering from the quality of the burned material. When compared to conventional fossil fuels, the quality of the delivered material is very variable with solid biofuels. The low quality of the burned material leads to a low energy value, i.e. the combustion itself is not so efficient and does not provide as much heat and energy. Nowadays, in the industry, the term solid biomass mainly refers to wood biomass, i.e. wood chips. When burning wood chips, it is important to know these parameters such as fraction, moisture content and admixture content. In the countries of the European Union, the ISO 17225 standard even defines the range in which the properties of wood chips must be, which will then be used to produce electricity and heat. Unfortunately, very often there is a non-compliance with the standard and the wood chips that actually burn do not reach these parameters. Due to the bark blight that affected most of the forested area of Central Europe, wood from tree trunks was also allowed to be used for the production of wood chips, as the trees affected in this way could not be used for standard use. So it had to be used only for energy purposes. So the wood chips produced were of very high quality. This led many manufacturers to try to reduce the quality, in order to achieve the largest possible volume of weight of the

wood chips produced, and to start mixing high-quality chips with low-quality or even waste wood. Often even combinations with soil and straw were created. Unfortunately, economic needs often act as a strong force towards cheaper resources, such as the already mentioned residual or waste wood, bushes, bark or straw. As a result, manufacturers often produce mixtures of "high" and "low" quality (Lokare et al, 2006), (Eriksson et al, 2009)

The raw material used and its unsuitable fuel quality drastically affect the behavior of the biomass furnace. Substandard biomass reduces furnace life and leads to operational problems such as corrosion or ash deposition (Plankenbuhler et al, 2019), (Plankenbuhler et al, 2017), leading to increased gas and particulate emissions (Schon et al, 2019). A promising method for preliminary evaluation of the quality of wood chips is optical analysis (in the most basic case, image capture through photography) followed by image evaluation. Such technology is able to run most without the need for human intervention or interaction (eg by monitoring fuel conveyor belts, feeders or chain conveyors). Moreover, it is a non-intrusive measurement method that can be easily retrofitted into the fuel systems of biomass plants. This potentially enables a priori determination of raw material properties. Contactless analysis of biomass raw materials has been the subject of increasing interest in recent years. Swedish researchers reported that continuous image analysis to characterize biomass fuels was too time-consuming and "tiring" (Paulrud et al, 2002). However, due to the increase in computing resources and new technologies, there may have been a significant change from this point of view. The literature shows different image evaluation techniques for different purposes and applications. The authors in (Rodriguez et al, 2013) provide a good overview of the optical analysis of particle properties; however, they focus on individual particles instead of particles in large ensembles. Rezaei et al. examined individual parts of wood using microscopes, scanners and PC technology (Rezaei et al, 2016), (Igathinathane et al, 2009). However, there have also been ideas that do not consider the size of the wood chip fraction as a parameter, but the very distribution of the burned material in the combustion boiler (Ferrari et al, 2022). The shortcomings of the image analysis lie in the two-dimensional analysis, when we omit the third dimension when measuring particles, i.e. the depth of the part itself. According to (Tannous et al, 2012) according to the research carried out, a value of 30% of its part width can be considered accurate and reliable for the particle size. The problem cannot be solved by the already developed 3D analysis method today, because the material is transported and stored in a bulk state, so it is not possible to use 3D analysis to analyze parts inside the bulk material (Reley et al, 1942).

Most researchers dealing with the issue of particle size determination, but already for wood chips or other materials, agree that the most promising method in the future is precisely image analysis, which can identify a large number of variable parameters and, based on the information obtained, then mathematically calculate and model a real fractional analysis material. It appears from the literature that image analysis in conjunction with mathematical modeling software is one of the main non-destructive methods for real and immediate determination of the particle size, i.e. the size of the fraction in wood chips. Currently, we already have some software that is able to determine the particle size of various materials. For

example, the Sedimetrics digital Gravelometr software, which is commonly used in research projects on the size composition of sediment particles, has good results using image analysis (Graham et al, 2005), (Sime et al, 2003).

MATERIALS AND METHODS

For the experiment, we secured samples from companies that produce wood chips for energy use. The effort was to ensure as many different samples as possible regarding the type of wood from which the wood chips are then produced. Each sample was divided into 5 separate samples due to the proposed methodology. The sample was laid out in a created grid of known dimensions (1.5 x 1 m). Each time, the applied wood chip was removed and then the wood chip sample was re-applied. A Canon EOS 600D camera with a resolution of 18 mega pixels was chosen to take the photos that were subsequently used for image analysis. This is a robust consumer type camera. The camera was placed above this grid to achieve an even distribution of the photo and to avoid distortion of the photo due to the angle of the camera. All images were taken without the use of added light (flash lights, ring lights, continuous lights). Only the industrial lighting of the laboratory (tube lamps) was present when the photographs were taken. After accumulating a sufficient number of photos and samples, when there were a total of 7 samples and 5 photos were taken for each sample. Subsequently, the photographs taken were evaluated using a program for image analysis. From the obtained results, the wood chip fractions were evaluated and determined.

The Sedimetrics Digital Geavelometer program was chosen for image processing and analysis. Particle identification and measurement is an eight-step process. When the photos taken were edited using radial correction, projective transformation, converting the image to grayscale and then to binary image, median filter, highlighting thresholds, watershed transformation and, thanks to us, the known size of the measuring grid, converting the size of particles from pixels to millimeters.

The data from the image analysis was then compared with the data declared by the wood chip manufacturer and the accuracy of the image analysis was evaluated.

RESULTS AND DISCUSSION

All the companies we contacted produced wood chips from wood species that are found in the vicinity of the company's headquarters, so it is not an imported material, but really processing local resources. In practice, according to the companies interviewed, the 30 mm fraction is most often used. We also managed to secure the sizes of other fractions, but they mostly come from trees affected by bark beetle calamity, where it is possible to process tree trunks for the production of wood chips. It is therefore not a classically processed material such as branches, low trees and residues from logging. The wood chips for the samples were supplied by the companies: Kovosteel s.r.o., which supplied sample number 1 and 6, the wood comes from the recultivation project of the dead arm of the Morava River, i.e. the wood species found in the vicinity of the rivers. Sawmill Mendl Medlovice supplied samples 2 and 4, these are wood originating from residues after logging in the forest and from residues during further processing

at the sawmill. SÚS Uherské hradiště supplied wood chips that come from the processing of wood waste at their collection yard. The last company Lesy ČR, s.p. based in Buchlovice supplied wood chips from conifers affected by bark beetle blight. Table (Tab. 1) summarizes the information and parameters found on the investigated wood chip samples.

Tab. 1 Wood chips samples

Sample number	Type of wood chips	Fraction size [mm]
1.	Linden, Birch	50
2.	Spruce, Pine	50
3.	Waste wood	Not specifed
4.	Oak, Beech	30
5.	Spruce – Bark Beetle	10
6.	Invasive trees	50
7.	Spruce	30

After taking 5 digital photos for each sample examined (7 in total), the photos were converted from digital to grayscale, see figure (Fig. 1). Next, a radial correction was made figure (Fig. 2.), which must be applied due to the distortion of the image, due to the lens in the camera. Radial correction corrects image distortion caused by lens curvature. Distortion varies between cameras and at different focal lengths. While the effect of radial distortion on the inferred particle size distribution is likely to be small, it can be significant for some cameras at certain focal lengths. A new grayscale image was created to include this correction. Projective transformations were then applied to the photographs. A projective transform is applied to the image to correct for a camera axis that is not perfectly vertical over the center of the sample field. This transformation has altered the image and requires the specification of the sampling resolution (number of pixels and mm). The software automatically calculates the appropriate value to keep the image resolution approximately constant. The output of this adjustment was a rectified image in grayscale. Subsequently, the grayscale image was converted to a binary (black and white) image in which particles are represented in white and gaps in black. This phase consisted of three steps. Digital noise is reduced by using a median filter. The filter size setting was 5 x 5 pixels, but the filter setting can be changed to suit the usage. A larger filter reduces digital noise, but results in a slight blurring of the image. Gaps are enhanced by applying a morphological filter. The filter we set was a disc with a radius of 15 pixels, but the size can be changed. The goal of the filter was to highlight small dark areas in the image that represent gaps, without highlighting large dark areas, dark-colored particles may be mistaken for gaps. Increasing the size of the structuring element may increase the number of excluded particles, while decreasing its size may lead to insufficient enlargement of some gaps. The enhanced image was converted into two binary images containing threshold values at two different intensity values. Values were defined as percentiles of the intensity and frequency distribution. A threshold value of 1 was designed to identify all gaps in the image, but probably

also contains some intra-grain noise. A threshold of 2 was designed to identify only the darkest points in the image that definitely represent gaps. The two binary images were combined to create a third binary image that contained only those gaps from the first image that were associated with the gaps in the second image.

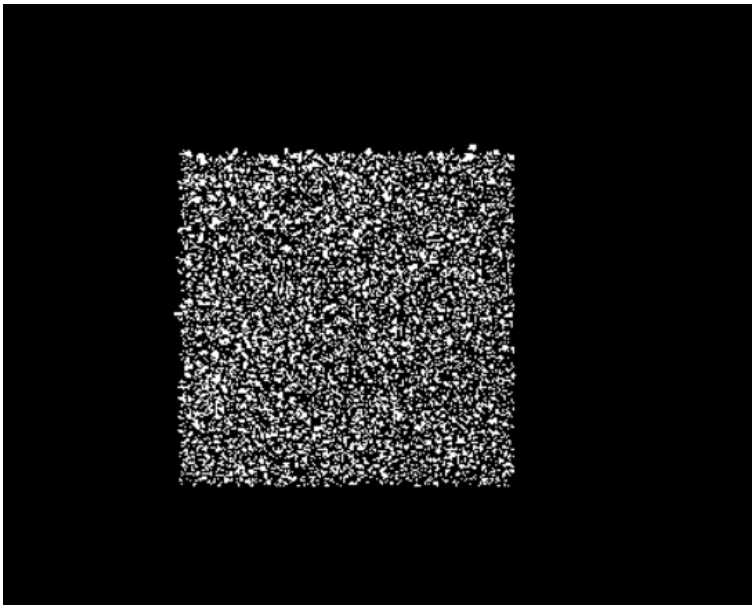

Fig. 1 Particle selection and conversion to grayscale

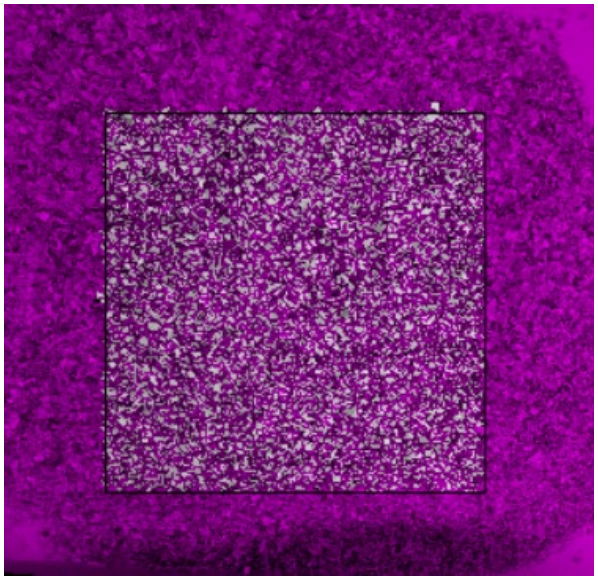

Fig. 2 Image after radial correction

Subsequently, particles separated at the point of contact with other particles. It is common for those regions that represent particles in the resulting binary image to actually consist of two or more connected particles. The binary image was further segmented by applying the watershed transformation. This led to significant re-segmentation of the image. An intermediate step in the watershed transformation was to smooth the image by applying the h-minimum transformation. The intensity of this smoothing was controlled by the minimum suppression parameter, which defaulted to 1. Decreasing this value resulted in increased particle oversegmentation, while increasing it may cause contact particle separation failure. The output

from the watershed segmentation was the final binary representation of the particles in the original image. Those particles that lay in the measurement area defined by the control points were selected for measurement. Since either including or excluding all particles crossing the boundary of the sampling region will lead to size bias (against and in favor), it is best to include particles crossing half the perimeter and exclude the rest. In our setup, particles lying along the top and left edges of the sampling region were included. The output of this step was a binary image containing only those particles that were inside the measurement window we defined.

Finally, the actual measurement of the particles took place. The selected particles are now measured. Information on particle size, orientation, shape and area is recorded. For now, particles are measured and reported in pixels, see figure (Fig. 3).

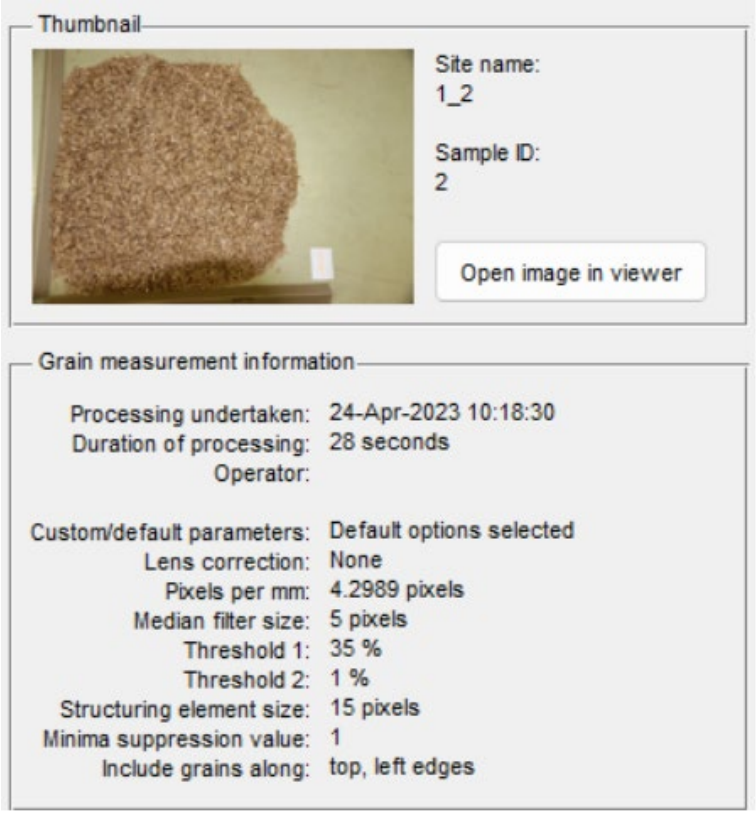

Fig. 3 Information for final particle size measurement

The final step converts particle sizes from pixels to millimeters using a known display scale.

Tab. 2 Table with the percentage representation of the size of the fraction in the 1st sample

	Size of fraction 1. sample									
measurement	10 mm	20 mm	30 mm	40 mm	50 mm	60 mm	70 mm	80 mm	90 mm	100 mm
1.	0.00 %	33.92 %	43.47 %	14.81 %	3.50 %	2.55 %	0.64 %	0.80 %	0.16 %	0.16 %
2.	0.00 %	27.14 %	41.03 %	25.78 %	0.16 %	0.00 %	3.67 %	1.11 %	1.11 %	0.00 %
3.	0.00 %	14.30 %	38.79 %	32.02 %	7.55 %	5.11 %	1.91 %	0.16 %	0.16 %	0.00 %
4.	0.00 %	34.81 %	40.19 %	17.16 %	4.82 %	1.02 %	1.86 %	0.07 %	0.00 %	0.07 %
5.	0.00 %	31.43 %	42.68 %	11.99 %	3.80 %	1.17 %	0.69 %	6.47 %	1.49 %	0.10 %
Average	**0.00 %**	**28.32 %**	**41.23 %**	**20.35 %**	**4.00 %**	**1.97 %**	**1.75 %**	**1.85 %**	**0.59 %**	**0.07 %**

Tab. 3 Table with the percentage representation of the size of the fraction in the 2nd sample

	Size of fraction 2. sample									
measurement	10 mm	20 mm	30 mm	40 mm	50 mm	60 mm	70 mm	80 mm	90 mm	100 mm
1.	0.00 %	34.41 %	42.09 %	14.27 %	5.88 %	2.28 %	0.84 %	0.12 %	0.12 %	0.00 %
2.	0.00 %	31.70 %	39.87 %	9.39 %	4.18 %	5.41 %	0.72 %	0.26 %	0.00 %	0.25 %
3.	0.00 %	37.18 %	36.65 %	21.60 %	3.17 %	0.70 %	0.70 %	0.00 %	0.00 %	0.00 %
4.	0.00 %	29.61 %	46.12 %	11.86 %	2.93 %	3.29 %	2.11 %	2.08 %	1.56 %	0.34 %
5.	0.00 %	19.49 %	34.50 %	39.07 %	0.43 %	4.15 %	1.36 %	0.00 %	1.00 %	0.00 %
Average	**0.00 %**	**30.48 %**	**39.85 %**	**19.24 %**	**3.32 %**	**3.17 %**	**1.15 %**	**0.49 %**	**0.54 %**	**0.12 %**

Tab. 4 Table with the percentage representation of the size of the fraction in the 3rd sample

	Size of fraction 3. sample									
measurement	10 mm	20 mm	30 mm	40 mm	50 mm	60 mm	70 mm	80 mm	90 mm	100 mm
1.	14.39 %	32.68 %	16.02 %	9.67 %	9.43 %	6.12 %	5.69 %	5.73 %	0.17 %	0.00 %
2.	13.28 %	27.69 %	17.7 %	12.44 %	10.9 %	11.38 %	6.25 %	0 .00 %	0.36 %	0.00 %
3.	11.14 %	31.82 %	20.61 %	15.37 %	13.84 %	4.53 %	2.5 %	0.19 %	0.00 %	0.00 %
4.	9.64 %	39.47 %	31.01 %	10.25 %	8.11 %	1.4 %	0.12 %	0.00 %	0.00 %	0.00 %
5.	17.61 %	24.19 %	35.22 %	14.29 %	7.69 %	2.68 %	0.00 %	1.32 %	0.00 %	0.00 %
Average	**13.21 %**	**31.17 %**	**24.11 %**	**12.40 %**	**9.99 %**	**5.22 %**	**2.91 %**	**1.81 %**	**0.11 %**	**0.00 %**

Tab. 5 Table with the percentage representation of the size of the fraction in the 4rd sample

	Size of fraction 4. sample									
measurement	15 mm	20 mm	25 mm	30 mm	35 mm	40 mm	50 mm	60 mm	70 mm	80 mm
1.	53.65 %	23.37 %	10.45 %	4.41 %	3.43 %	1.63 %	1.20 %	0.87 %	0.22 %	0.38 %
2.	45.22 %	29.17 %	9.75 %	6.34 %	6.34 %	2.31 %	0.80 %	0.06 %	0.00 %	0.00 %
3.	51.88 %	27.41 %	12.79 %	5.43 %	2.10 %	0.32 %	0.07 %	0.00 %	0.00 %	0.00 %
4.	47.92 %	22.41 %	11.17 %	7.36 %	4.82 %	4.02 %	1.41 %	0.89 %	0.00 %	0.00 %
5.	50.61 %	30.73 %	8.40 %	5.67 %	3.80 %	0.40 %	0.39 %	0.00 %	0.00 %	0.00 %
Average	**49.86 %**	**26.62 %**	**10.51 %**	**5.84 %**	**4.10 %**	**1.74 %**	**0.77 %**	**0.36 %**	**0.04 %**	**0.08 %**

Tab. 6 Table with the percentage representation of the size of the fraction in the 5th sample

	Size of fraction 5. sample									
measurement	10 mm	15 mm	20 mm	25 mm	30 mm	35 mm	40 mm	50 mm	60 mm	70 mm
1.	69.04 %	23.23 %	6.61 %	1.02 %	0.07 %	0.00 %	0.02 %	0.00 %	0.00 %	0.00 %
2.	72.52 %	19.79 %	4.63 %	2.27 %	0.59 %	0.16 %	0.04 %	0.00 %	0.00 %	0.00 %
3.	68.44 %	20.33 %	5.91 %	2.02 %	2.65 %	0.65 %	0.00 %	0.00 %	0.00 %	0.00 %
4.	70.63 %	17.80 %	9.84 %	1.46 %	0.16 %	0.11 %	0.00 %	0.00 %	0.00 %	0.00 %
5.	71.96 %	21.31 %	2.28 %	1.99 %	1.46 %	0.68 %	0.32 %	0.00 %	0.00 %	0.00 %
Average	**70.52 %**	**20.49 %**	**5.85 %**	**1.75 %**	**0.99 %**	**0.32 %**	**0.08 %**	**0.00 %**	**0.00 %**	**0.00 %**

Tab. 7 Table with the percentage representation of the size of the fraction in the 6th sample

	Size of fraction 6. sample									
measurement	15 mm	20 mm	25 mm	30 mm	35 mm	40 mm	45 mm	50 mm	60 mm	70 mm
1.	51.23 %	23.45 %	11.43 %	4.91 %	3.22 %	2.29 %	1.35 %	0.93 %	0.76 %	0.42 %
2.	50.11 %	29.59 %	7.73 %	6.20 %	4.76 %	0.32 %	0.32 %	0.97 %	0.00 %	0.00 %
3.	47.82 %	21.31 %	16.12 %	4.75 %	2.14 %	1.81 %	0.84 %	1.02 %	0.61 %	0.37 %
4.	48.92 %	26.41 %	9.59 %	7.08 %	4.11 %	1.02 %	0.89 %	1.11 %	0.89 %	1.00 %
5.	53.83 %	30.30 %	8.68 %	2.98 %	1.21 %	1.67 %	1.33 %	0.00 %	0.00 %	0.00 %
Average	**50.38 %**	**26.21 %**	**10.71 %**	**5.18 %**	**3.09 %**	**1.42 %**	**0.95 %**	**0.81 %**	**0.45 %**	**0.36 %**

Tab. 8 Table with the percentage representation of the size of the fraction in the 7th sample

	Size of fraction 7. sample									
measurement	15 mm	20 mm	25 mm	30 mm	35 mm	40 mm	50 mm	60 mm	70 mm	80 mm
1.	58.72 %	23.24 %	9.54 %	3.38 %	2.43 %	1.04 %	0.61 %	0.61 %	0.26 %	0.18 %
2.	42.68 %	31.14 %	8.33 %	7.78 %	6.08 %	3.12 %	0.80 %	0.07 %	0.00 %	0.00 %
3.	46.51 %	39.37 %	6.29 %	2.82 %	3.01 %	1.23 %	0.07 %	0.70 %	0.00 %	0.00 %
4.	38.22 %	46.81 %	9.79 %	3.16 %	1.01 %	0.00 %	0.71 %	0.30 %	0.00 %	0.00 %
5.	40.93 %	40.65 %	7.38 %	4.29 %	2.18 %	2.96 %	0.35 %	0.27 %	0.66 %	0.33 %
Average	**45.41 %**	**36.24 %**	**8.27 %**	**4.29 %**	**2.94 %**	**1.67 %**	**0.51 %**	**0.39 %**	**0.18 %**	**0.10 %**

The measurement results for all the samples examined by us do not contain a serious deviation from the size of the fraction given by the manufacturer. The most accurate agreement with the measured values can be observed in sample number 5. The 10 mm fraction is contained in approximately 70% of the measured sample. The majority of the remaining part consists of fractions of size 15 and 20 mm. Although, according to the measurements, we get approximate steps with the sizes of the fraction declared by the manufacturer, in most cases they still match in approximately 50% of the content of the measured sample. The remaining part of the sample is made up of fractions around the declared fraction. If we consider the surrounding fractions to be acceptable, our experiment achieves about 85% measurement accuracy with the declared values. For sample number 5, there was a significant agreement of about 91% compared to the declared fraction size from the manufacturer. A high percentage of stairs can be caused by the quality of the work as well as the precise adjustment of the production machine. From experience, the overall quality of wood chips made from bark beetle wood is much higher than that of wood chips made from residues after logging or cutting smaller trees and bushes. Even this fact can have an effect on the examined sample and its regularity. On the contrary, for sample number 3, the agreement is only around 68%. The size of the fraction was not declared to us for this examined sample, therefore the size of the fraction with the largest percentage representation was used for assessment. The sample comes from the processing of wood residues (branches, bushes) after logging in the forest. This indicates from general experience that this wood chip is not of high quality, therefore there may be a larger variation in fraction size. It is not excluded that wood chips can come from different types of wood chips, i.e. it can be a mix of wood chips. Of course, the difference in the size of the fraction could have been caused by a poorly set machine for the production of wood chips, or by the low quality of the work of the operator of the production machine. However, the difference between fraction sizes may seem small, but it is necessary to take into account the overall efficiency of the combustion boiler, when even a minor deviation from the declared and real state can cause economic

damage, increased wear and tear of the combustion equipment or increased production of harmful substances into the air. Sedimetrics digital Gravelometr software, developed by researchers at Loughborough University, was used for image analysis. The software works on the principle of graphic and mathematical image modeling. Table (Tab. 9) shows the measured values in comparison with the declared values from the manufacturer. Of the sub-targets, only the presence of soil (dust) could be measured, for the measurement of dust particles it was necessary to set the most detailed values. However, with this setting, there was a large distortion of the values when measuring the size of the wood chip fraction. Other admixtures, such as bark and wood species, could not be obtained with the help of our chosen image analysis software.

Tab. 9 Comparison of measured values with declared values

	sample number						
value type	1.	2.	3.	4.	5.	6.	7.
Declared value	30 mm	30 mm	not specified	20 mm	8 mm	20 mm	20 mm
Measured value (compliance) [%]	89.90 %	89.57 %	68.49 %	76.48 %	91.01 %	87.30 %	89.92 %

CONCLUSION

This thesis investigated and demonstrated a method of evaluating the quality of the size fraction in wood chips using image analysis. The method was designed with a view to future application in an industrial environment in which wood chips are processed to produce electricity or heat. The effort was to verify whether it is possible to determine the real fractional composition of wood chips in a controlled laboratory environment using software for image analysis.

The overall procedure and results of the experiment lead us to the conclusion that it is possible to determine the actual size of the wood chip fraction in minutes using image analysis. From seven measurements, all values were measured with approximately 85% accuracy.

A recommendation for further research is to continue to measure more wood chip samples and simulate as realistic an environment as possible that would approximate an industrial environment. Next, try to use other software for image analysis, whether it is not possible to achieve greater accuracy and the possibility of better resolution of impurities. Another suitable topic for future research could be to determine the economic impact of burning wood chips if we set the boiler combustion parameters with an accuracy of 85% to the actual condition of the fuel being burned. By how much will the calorific value of wood chips per unit of weight decrease and how big will the financial loss be in the event of an imperfect setting of the combustion boiler.

REFERENCES

Lokare, S.S., Dunaway, J.D., Moulton, D., Rogers, D., Tree, D.R., Baxter, L.L. Investigation of ash deposition rates for a suite of biomass fuels and fuel blends. *Energy Fuels* 2006, 20, 1008–1014.

Eriksson, G., Hedman, H., Bostrom, D., Pettersson, E., Backman, R., Ohman, M. Combustion characterization of rapeseed meal and possible combustion applications. *Energy Fuels* 2009, 23, 3930–3939.

Plankenbuhler, T., Muller, D., Karl, J. Influence of Fine Fuel Particles on Ash Deposition in Industrial-Scale Biomass Combustion: Experiments and Computational Fluid Dynamics Modeling. *Energy Fuels* 2019, 33.

Plankenbuhler, T., Muller, D., Karl, J. Slagging prevention and plant optimisation by means of numerical simulation. In Proceedings of the *25th European Biomass Conference & Exhibition*, Stockholm, Sweden, 12–15 June 2017; pp. 653–659.

Schon, C., Kurptz, D., Mack, R., Zelinski, V., Loewen, A., Hratmann, H. Influence of wood chip quality on emission behaviour in small-scale wood chip boilers. *Biomass Conv. Bioref.* 2019, 9, 71–82.

Paulrud, S., Erik, J., Nilsson, C. Particle and handling characteristics of wood fuel powder: E_ects of di_erent mills. Fuel Process. *Technol*. 2002, 76, 23–39.

Rodriguez, J.M., Edeskar, T., Knutsson, S. Particle Shape Quantities and Measurement Techniques—A Review. *EJGE* 2013, 18, 169–198.

Rezaei, H., Lim, C.J., Lau, A., Sokhansani, S. Size, shape and flow characterization of ground wood chip and ground wood pellet particles. Powder Technol. 2016, 301, 137–746. [CrossRef]

Igathinathane, C.; Pordesimo, L.O.; Columbus, E.P.; Batchelor,W.D.; Sokhansani, S. Sieveless particle size distribution analysis of particulate materials through computer vision. *Comput. Electron. Agric*. 2009, 66, 147–158.

Ferrari, L., Caposciutti, G., Higl, M., Müller, B., Kalfas A.; Ferrari L. ; Šimurda, D. Biomass woodchip tracking by image analysis in a model of a fixed bed combustor. *E3S Web of Conferences*. 2022, 345. ISSN 2267-1242.

Tannous, K., Lam, P.S., Sokhansani, S., Grace, J.R. Physical Properties for Flow Characterization of Ground Biomass from Douglas Fir Wood, *Particulate Science and Technology*, 31 (2012) 291-300

Riley, N.A. Projection sphericity, Journal of Sediment Research, 11 (1942) 94-95.

Graham, D.J., Reid, I.,Rice, S.P. Automated Sizing of Coarse-Grained Sediments: Image-Processing Procedures. *Math Geol* 37, 1–28 (2005).

L.C. SIME, R.I. FERGUSON; Information on Grain Sizes in Gravel-Bed Rivers by Automated Image Analysis. *Journal of Sedimentary Research* 2003;; 73 (4): 630–636.

Monitoring of the energy production in PV power plants

D. Mrázek[1], J. Šafránková[1], J. Sedláček[1], V. Beránek[2], V. Poulek[1], M. Libra[1]

[1]Department of Physics, Faculty of Engineering, Czech University of Life Sciences Prague, Prague, Czech Republic
[2]Solarmonitoring, Ltd., Prague, Czech Republic

Abstract

In this article, we present selected results of monitoring the operation of photovoltaic power plants. The monitoring system was developed in collaboration with authors and is operated at approximately 85 photovoltaic power plants in the Czech Republic.

Key words: PV power plant, photovoltaics, energy conversion

INTRODUCTION

The efficiency of a photovoltaic (PV) system depends on many parameters. In our previous article (Libra et al., 2021), we discussed influence of the temperature on the efficiency of the photovoltaic energy conversion. In this article, we compare mainly the amount of electricity produced. We present examples of our data collected from the monitored photovoltaic power plants. We compare the data with the expected values from the internationally used application about the photovoltaic energy forecast (PVGIS). Influence of roof installation of photovoltaic modules on the microclimate conditions was studied for example in the work (Bilčík et al., 2021).

MATERIALS AND METHODS

The presented photovoltaic power plant is located in the south Moravia region and it has coordinates 48.8°N, 16.9°E. The nominal output power is 4026 kWp. The power plant started the operation in 2015. The power plant uses PV panels based on crystalline silicon placed on fixed stands with an inclination of 35° with an orientation almost to the south (5° to the west). In this configuration, the highest electricity production is expected in the Central Europe.

RESULTS AND DISCUSSION

Figure (Fig. 1) shows an example of the electricity production in the mentioned photovoltaic power plant during the years 2021-2022. For a better comparison, the values are converted per nominal peak power 1 kW_p. The value 1155 $kWh.kW_p^{-1}.year^{-1}$ is expected in the south Moravia region (according the internationally used application PVGIS). So, the actual value is about 25% higher than the expected value. This testifies to the quality of the used photovoltaic panels with high efficiency of the photovoltaic energy conversion as well as to the quality of the construction of the entire photovoltaic power plant.

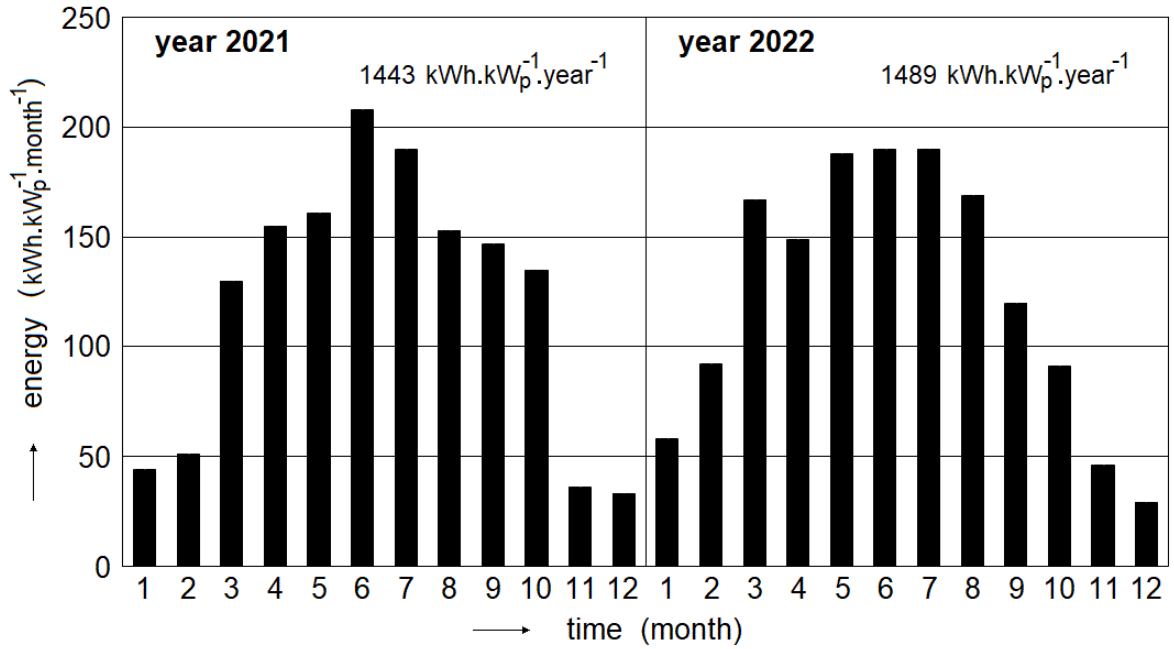

Fig. 1 Electricity production in the PV power plant located in the south Moravia region during last two years

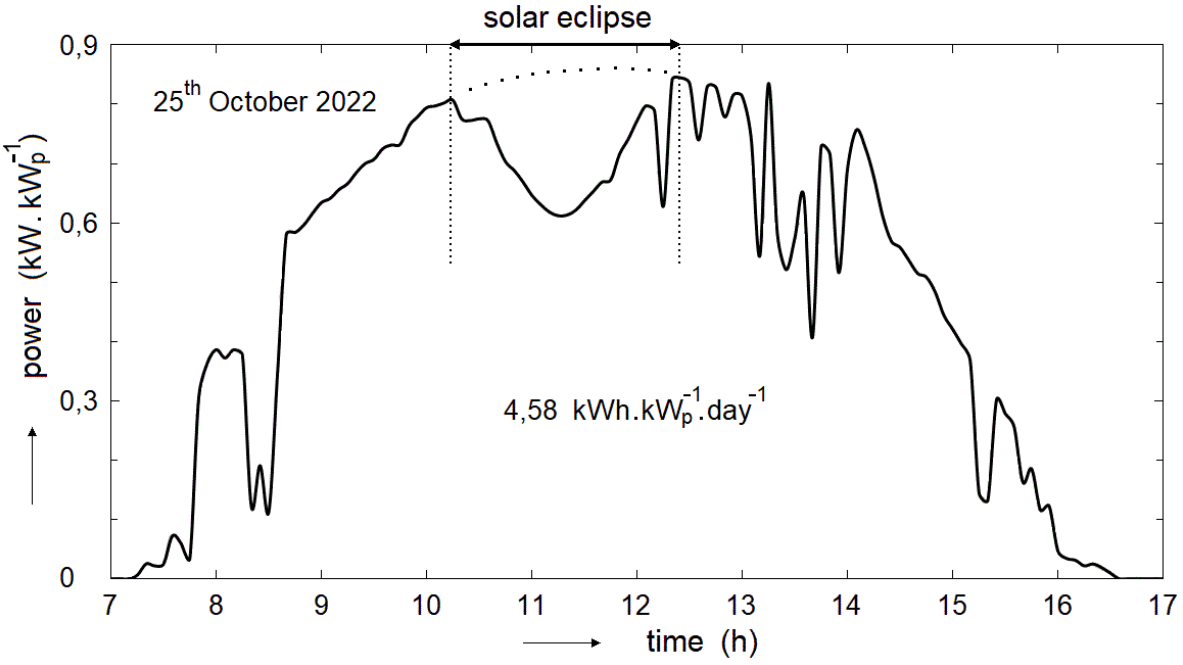

Fig. 2 Time dependence of the instantaneous power during the 25th October 2022

Figure (Fig. 2) shows the time dependence of the instantaneous power during the 25th October 2022. On this day, there was a partial eclipse of the Sun, which accounted for approx. 30% of the covered surface of the solar disk. The time of the solar eclipse is marked in the figure.

CONCLUSION

The production of electricity in the monitored power plants exceeds the expected values. Solar eclipses rarely occur, but they have a significant impact on the production of electricity in PV power plants. We assessed the effect of a solar eclipse on the loss in daily electricity production. The presented results from the selected photovoltaic power plant show a good agreement between theory and experiment, data from other PV power plants are similar. The eclipse on October 25, 2022 covered only about 30% of the surface of the solar disk and resulted in a loss of 5.8 % in daily electricity production. With a larger eclipse, the loss would be larger.

REFERENCES

Libra, M., Petrík, T., Poulek, V., Tyukhov, I.I., Kouřím, P. (2021). Changes in the Efficiency of Photovoltaic Energy Conversion in Temperature Range With Extreme Limits. IEEE *Journal of Photovoltaics*, 11(6): 1476-1481.

Bilčík, M., Božiková, M., Čimo, J. (2021). Influence of Roof Installation of PV Modules on the Microclimate Conditions of Cattle Breeding Objects. *Applied Sciences, 2 11:2140.*

PVGIS (Photovoltaic Geographical Information System), online (2023). Available from: https://re.jrc.ec.europa.eu/pvg_tools/en/tools.html. Accessed 12.4.2023.

Reduction of emissions from operation of cord fiber spinning mill

J. Palátka[1], K. Mayer[1], M. Pexa[1], E. Olmrová[1]

Department for Quality and Dependability of Machines, Faculty of Engineering, Czech University of Life Sciences Prague, Prague, Czech Republic

Abstract

Global impact of human activity due to general globalization now requires even closer attention than ever before. Generally used concepts are being analyzed horizontally and vertically seeking for space to improve. In this study it is a gas ventilation technology at a viscose cord fiber spinning mill operations and subsequent regeneration of raw materials being analyzed. By modifying existing technological concept, more efficient extraction of gas is obtained during spinning of the fiber. Vent gas contains sulfur compounds, thus higher concentration of sulfur gas for regeneration is desired. An increase in yield of sulfur compounds during production leads to an increase in secondary production of regenerated sulfuric acid. As a secondary effect, there is a decrease in concentration of sulfur compounds emitted into the environment and a significant savings in natural gas consumption are achieved. Natural gas gets consumed in regeneration process to preheat SULFOX technology. The discussed change results in an absolute reduction annually by 517 045 kg of emissions. Proposed modification consists of changing duct routing together with design change of covering spinning area with inside spinning mill machines. Modifications contributes to obtaining higher concentrations of sulfur gas for regeneration.

Key words: yarn, cord, viscose, spinning, emissions, savings, efficiency

INTRODUCTION

During spinning process (Li et al., 2021) and drying process of the fiber (Mondal et al., 2020) there is a large amount of sulfur compounds released into ambient air. (Hall & Losee, 1997) It used to be mainly exhausted through chimney (Klemeš & Varbanov, 2018) to the atmosphere, (Tan et al., 2001) which is undesirable condition. (Chaaban, 2001), (Hossain et al., 2008), (Xu et al., n.d.) The cord fiber spinning mill, where sulfur compounds are being released during production, consists of 56 spinning machines. The cord laundry is air-conditioned by six air-conditioning chambers with a total throughput of 600 000 $m^3 \cdot h^{-1}$. The machines and their surroundings have a complex air-conditioning system, which is divided into two basic streams. Between individual machines and between rows of machines.

Each spinning machine is covered both on wet and dry side to prevent gas release into surroundings. The original design did not allow efficient extraction of the highest proportion of sulfur compounds for subsequent regeneration. (Varbanov et al., 2021) Extraction was solved only inside the machines, where the main two streams of air vents are located. A ducting with low concentrations of sulfur gas that goes directly to chimney. The other ducting for rich concentrations of sulfur gas gets drawn off to SULFOX recovery plant. (King et al., 2013b)

The SULFOX device processes ventilation air rich in sulfur gas from cord spinning mill (Majumdar et al., 2022), and it subsequently transforms CS_2 and H_2S into H_2SO_4.(King et al., 2013a) The regenerated sulfuric acid is used again for the production process. (Sayyed et al., 2019) If majority of emissions were to be released without further use to the chimney,(Huang & Han, 2014) it would be a significant financial loss,(Seferlis et al., 2021) as well as a significant source of polluting emissions contaminating the environment.(Shen et al., 2010), (Varbanov et al., 2021), (Zivkovic et al., 2018)

Another significant thing that must be taken into consideration is the fact that spinning mill production equipment is not fully automated, which implies necessity for operator staff to be in immediate vicinity of the machine production technology. The technological change also aims to minimize the operator's exposure to the chemical environment. (Wang et al., 2020)(Yong et al., 2016) The main goal of this paper is to describe a solution to increase mass flow of sulfur gas generated during production of cord yarn and to transport it to SULFOX facility (*SULFOX - SYSTEM FOR SULFIDE POLLUTION-CONTROL-Web of Science Core Collection*, n.d.) for subsequent regeneration.

MATERIALS AND METHODS

The place where largest emission of sulfur gas occurs on spinning machines is located around galette area. This paper focuses mainly on research of covering the galette space and thereby obtaining the benefit of extracting much higher gas concentration for secondary use. This is subsequently regenerated on SULFOX unit, which leads to a reduction in amounts of carbon disulfide emissions through chimney and also increase in production of regenerated sulfuric acid. The main pollutant from spinning mill facility is carbon disulfide (CS_2) in gaseous form. Carbon disulfide is an input raw material for production of xanthogenate. As part of process, it gets then released back to ambient air when the fiber is spun. Carbon disulfide can reach up to 80 % of its content in the evaporated gas. Of the rest 20 % becomes hydrogen sulfide H_2S.

A significant part of the mentioned sulfur gas is being absorbed into liquids that flow through the spinning machine. Typically, this is a spinning bath, a plasticizing bath and washing water. The remaining carbon disulfide and hydrogen sulfide released to the air are transported from spinning mill to regeneration equipment using ventilator. Before described design change, regeneration reached around 49 % CS_2 and almost all H_2S. Regenerated sulfuric acid is then used for regeneration of the baths. The modification mainly represents decrease in mass flows of carbon disulfide in air streams with low sulfur content and redirecting them, thus getting rich streams of air containing sulfur compounds even higher in their concentrations. The aim is to increase mass flows of streams rich in sulfur compounds, as a result of which emission on the chimney would be reduced.

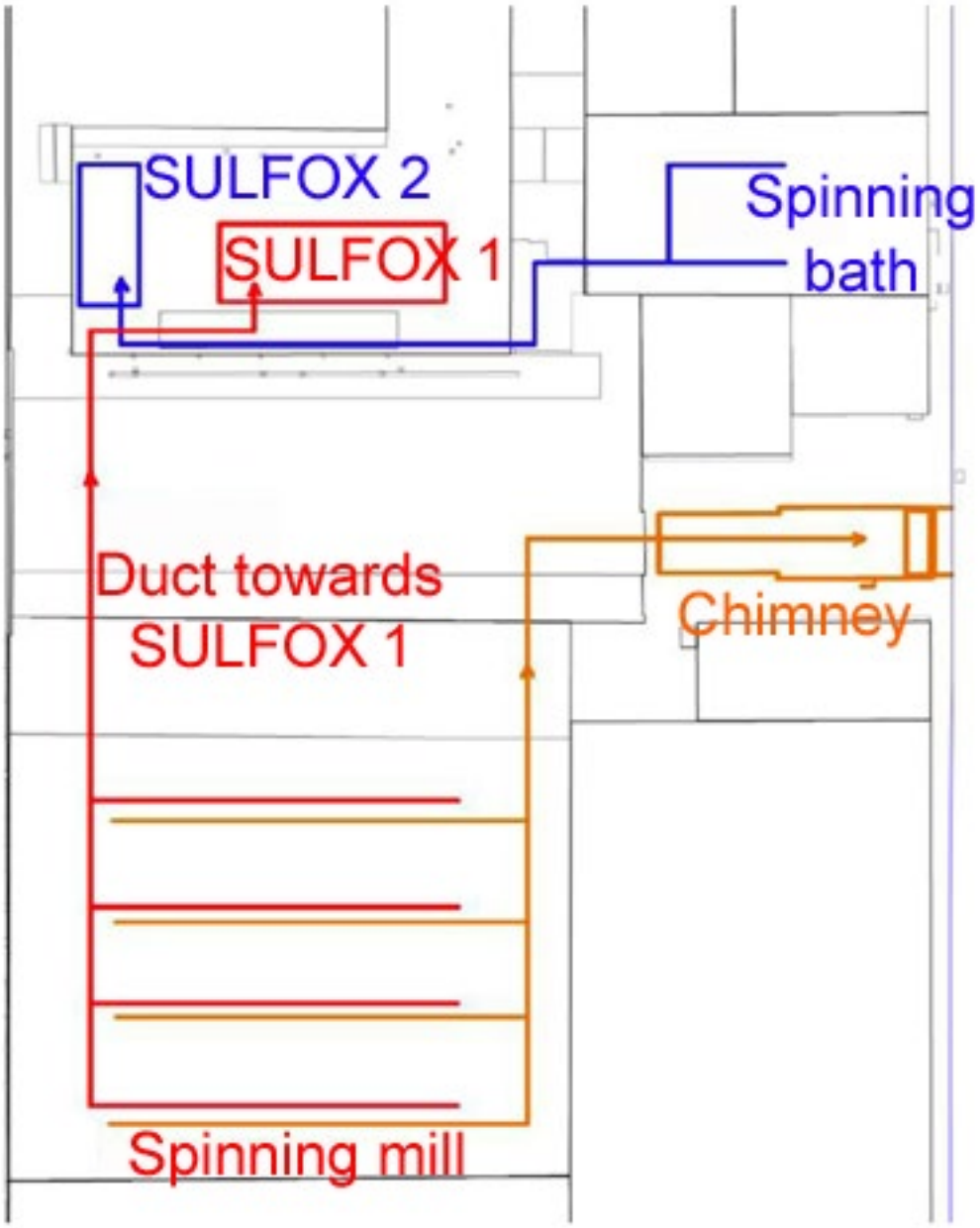

Fig. 1 Original air system layout

There is a simplified diagram of air system as shown on figure (Fig. 1), with duct marked red representing rich concentrations of exhaust gas. Those are transported to SULFOX device for regeneration. Low concentrations of gas evaporation are marked in orange and those are released into the atmosphere through a chimney. This schematic represents original design of the air system.

SPINNING MILL MACHINES AIR SYSTEM

A stream rich in sulfur compounds is drawn off from the galette plate. In the top part of the machine there is an air duct that sucks air from the entire machine to the chimney. Figure (Fig. 2) shows where carbon disulfide and hydrogen sulfide are released during fiber spinning process. A major problem with this arrangement is some rapid upward flow of air including

gas, where the high concentration of evaporated gas gets diluted. The volume flow rate of the rich air concentrations had limitations due to size of the SULFOX sulfur processing facility. This resulted in ineffective suction of a relatively small amount of sulfur gas through this route. Everything that was not absorbed by the bottom route, where rich gas concentrations are directed, followed to the upper suction ducting and was transported to the chimney.

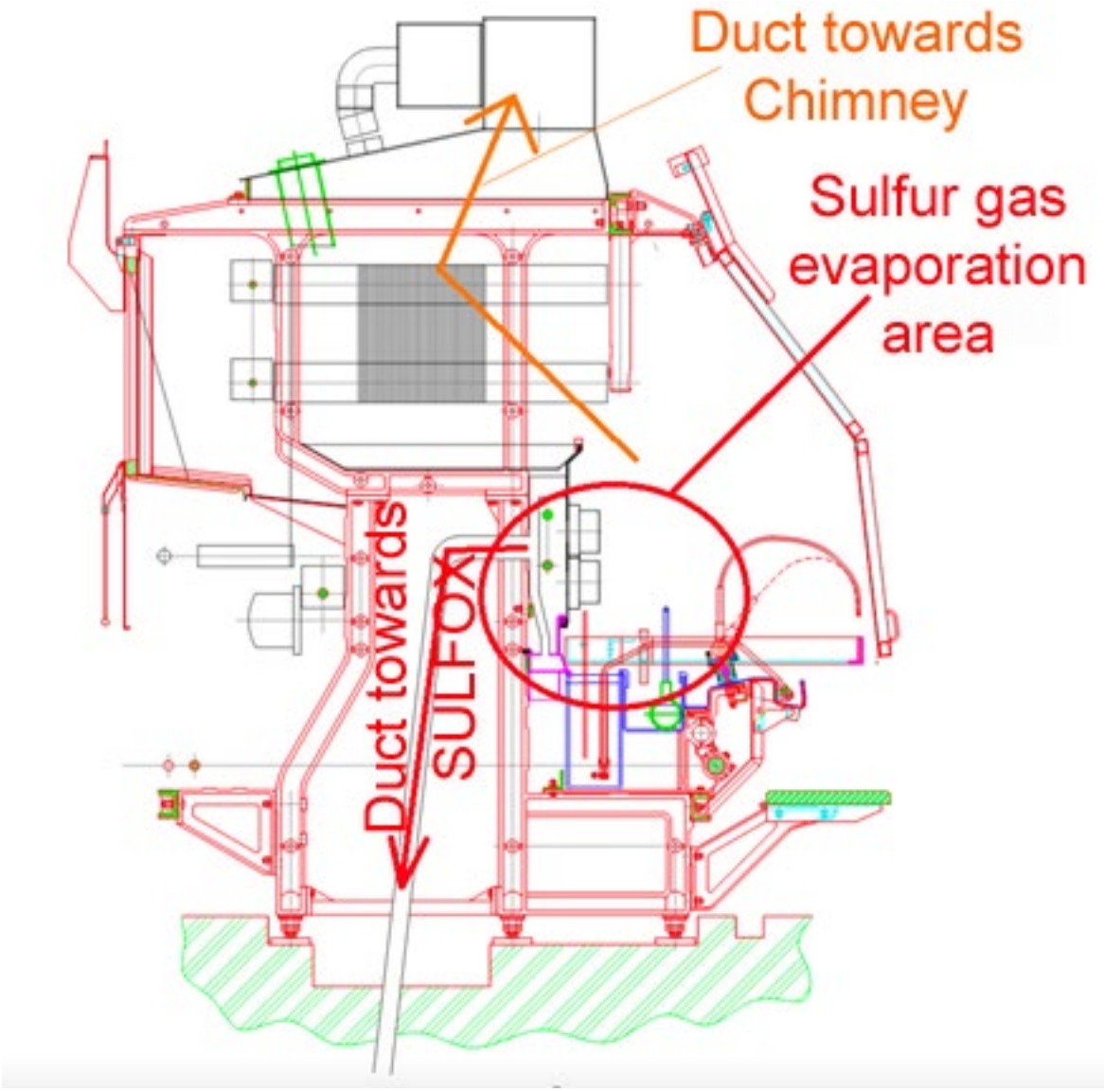

Fig. 2 Cross section drawing of spinning machine

Such an arrangement had the following negative effects:

- A large part of mass flow of sulfur gas was not reprocessed and thus got emitted through the chimney into the atmosphere.
- The ducting of high concentration gas within machines was inappropriately designed and therefore there used to be a significant dilution of the air mass, while the air mass route, where high content of sulfur gas is expected, actually contained relatively low concentrations of sulfur compounds.

- Due to gas evaporation with inside the machine and subsequent inefficient extraction by the bottom duct, there was significant contact with machine components in top section causing corrosion due to the acidic nature of the environment.
- The diluted air stream with relatively low concentration of sulfur gas, where there was expected high content of sulfur gas, had a negative effect on the operation of the SULFOX unit. A low content of sulfur compounds means a low oxidation heat supplied for catalytic oxidation. For this reason, it was necessary to supply external thermal energy to the reaction and heat the air up using natural gas.

AIR SYSTEM WITH A STREAM RICH IN SULFUR GAS

Air system of spinning mill is divided according to the process into primary extraction from the spinning mill machines. Each machine has an outlet DN160. The outlet then gets connected to a DN600 pipeline. Overall, then 4 x DN600, that are connected to a graded central pipeline. It has a dimension of DN1200 at the outlet and is routed to SULFOX unit. See figure (Fig. 3). The venting of plasticizing bath as well as suction of laundry water was connected here by a DN250 pipe. Each stream has its own fan and at the point of connection between row A and B there used to be congestions in the central pipeline. These two streams were installed additionally not of the original design and used to be disturbing hydraulic proportions in the system. Due to this, the suction rows used to be uneven, and the pipe got congested, as shown in figure (Fig. 4).

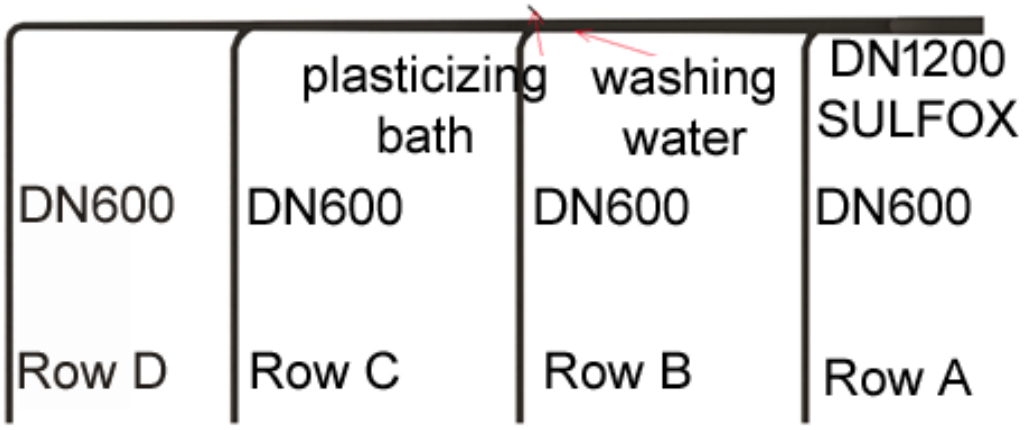

Fig. 3 Schematic of rich sulfur gas air duct

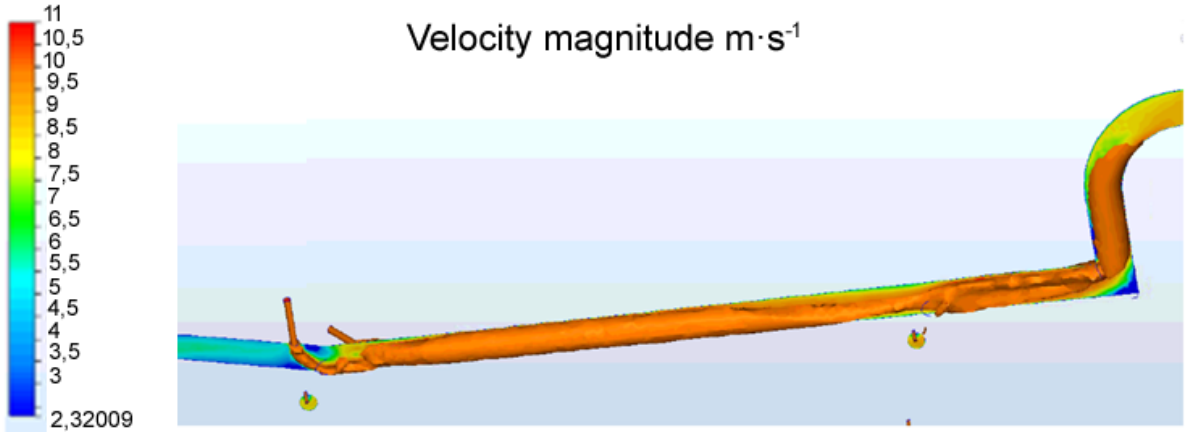

Fig. 4 Simulation of hydraulic proportions in central pipeline

SULFUR GAS PROCESSING UNIT SULFOX

The SULFOX device as shown in figure (Fig. 5) works on principle of catalytic oxidation and subsequent hydration. Carbon disulfide together with hydrogen sulfide are heated using residual heat and pass through a catalytic reactor where it oxidizes to sulfur dioxide. Subsequently, the sulfur dioxide gets showered with water leading to sulfuric acid production. Simply put, raw sulfur remains in the cycle – sulfur compounds are recycled and not released into the atmosphere. The disadvantage of this principle lays in a fact that if there are low concentrations of sulfur compounds at the inlet to SULFOX unit, the air must be additionally heated by burning natural gas due to low oxidation heat. SULFOX processes volume flow of air with total nominal flow rate 33 000 $m^3 \cdot h^{-1}$, while the maximum concentration of sulfur compounds able to regenerate are following. Carbon disulfide can be regenerated up to 7 000 $mg \cdot m^{-3}$. Hydrogen sulfide can be regenerated up to 5 000 $mg \cdot m^{-3}$. The concentration is related to a cubic meter of air.

Fig. 5 SULFOX catalytic oxidation unit

WET SIDE SPINNING MILL MACHINES COVERING

As part of this research, galette space was covered with a new mechanism (Fig. 6 and 7) and subsequent measurement had been carried out. Change in yield of sulfur compounds for regeneration had been established. This implementation took place on wet side, which is where the most evaporation of gas occurs on the spinning mill machine. The modification proves extraction with much higher gas content dedicated to regeneration on SULFOX unit, thereby reduction of emitted amount of carbon disulfide into atmosphere and, as a result, increased yield

of regenerated sulfuric acid. The advantage of this concept is physical separation of space with high content of evaporated gas and normal working space. Due to that, no mixing of gas vapor with ambient air occurs. High concentration sulfur gas does not interfere with machine internals at the top part of machine, so any corrosive processes get mitigated. Also, there is no contamination of surroundings. The disadvantage is complexity of mechanization and increased requirements for serviceability of the machinery.

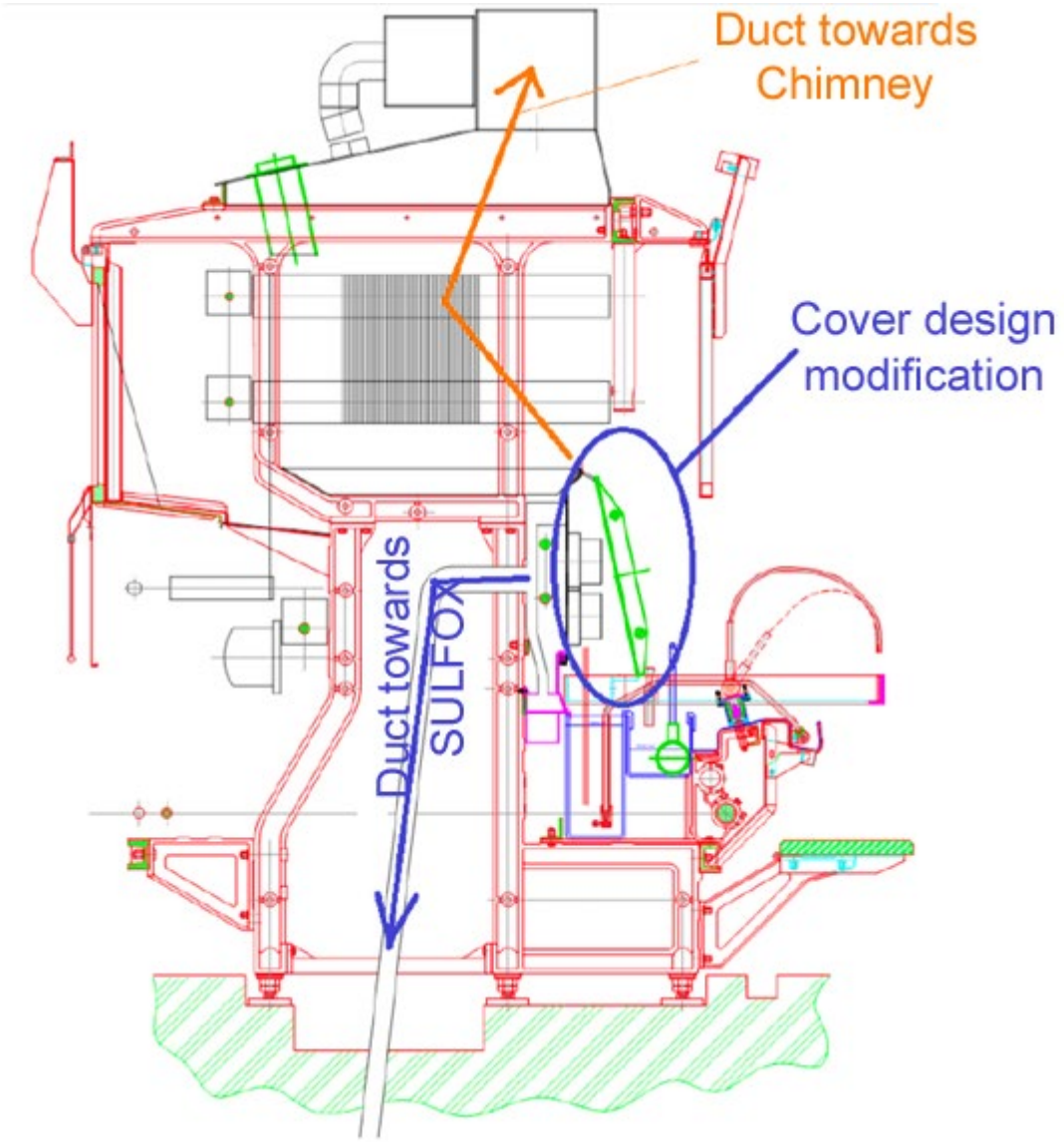

Fig. 6 Cross section drawing of spinning machine indicating modification of coverage on wet side

The cover is attached to the machine using a rack and pinion gear and an electric motor. It moves upwards when opened. The whole system is controlled by up, down and stop buttons. After activating the up button, the window is opened along with the cover.

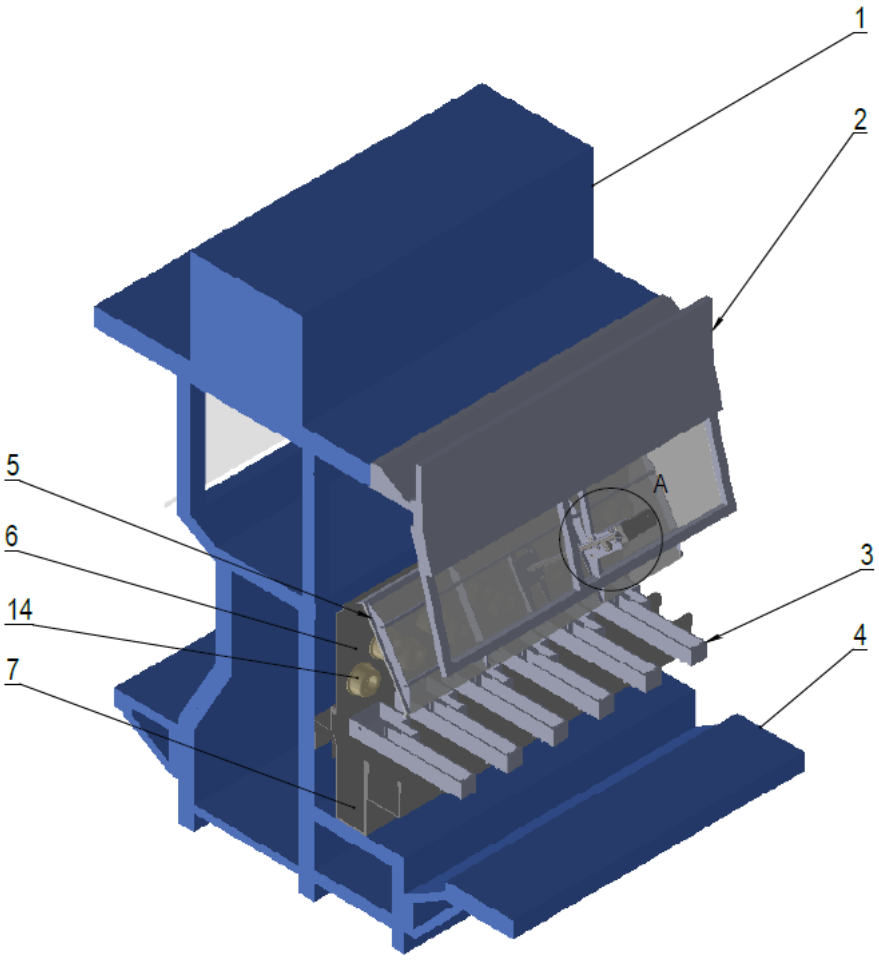

Fig. 7 Design solution for covering the spinning area (wet side)

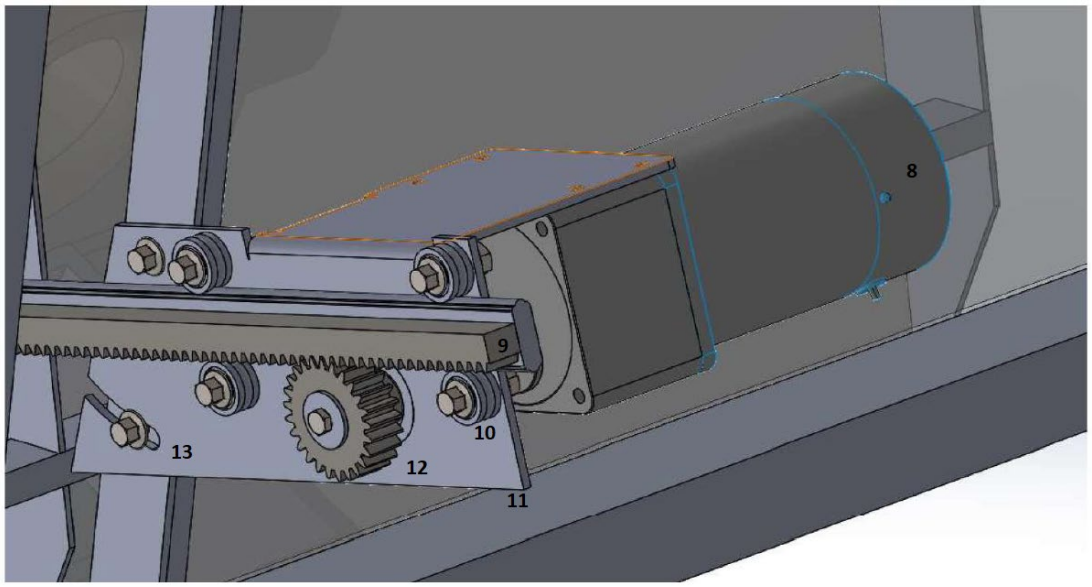

Fig. 8 Cover drive mechanism

The whole concept, as shown in figure (Fig.7), consists of a spinning mill machine design (1), new concept of the cover (2), spinning tubs (3), walking boards (4), cover of the galette space (5), galette space itself (6), plasticizing trough (7), drive of the cover of galette space (8), gear

rail (9), guide rolls (10), supporting plate (11), drive gear (12), positioning mechanism (13) and galette (14). These components are shown in figure (Fig. 8).

DRY SIDE SPINNING MILL MACHINES COVERING

A very similar situation is also on the dry side of the machine, where the fiber gets dried. As part of this research, the washing area was separated from drying area, as can be seen in figure (Fig. 9). This prevents high concentrations of rich sulfur gas from reaching the dry side. The cover is made of clear PVC, which is placed on hinges of the washing cylinders, and with the help of a roller mechanism, the individual covers are moved over each other. The advantage of this solution is to prevent channel congestion on the dry side of the machine.

Fig. 9 Modification of drying space cover on spinning machine at dry side

ROUTING MODIFICATION OF AIR DUCT FOR PLASTICIZING BATH AND WASHING WATER VENT

In order to solve the hydraulic conditions, it was necessary to change routing of washing water vent together with vent of plasticizing bath. Both routes are ducted separately to the SULFOX device. It stabilizes volume flows of individual rows. The gas evaporation of the wash water connects to SULFOX 2 unit to increase volumetric flow capacity for cord spinning mill facility. It is therefore an overall conceptual change in the air system, as can be seen in figure (Fig. 10).

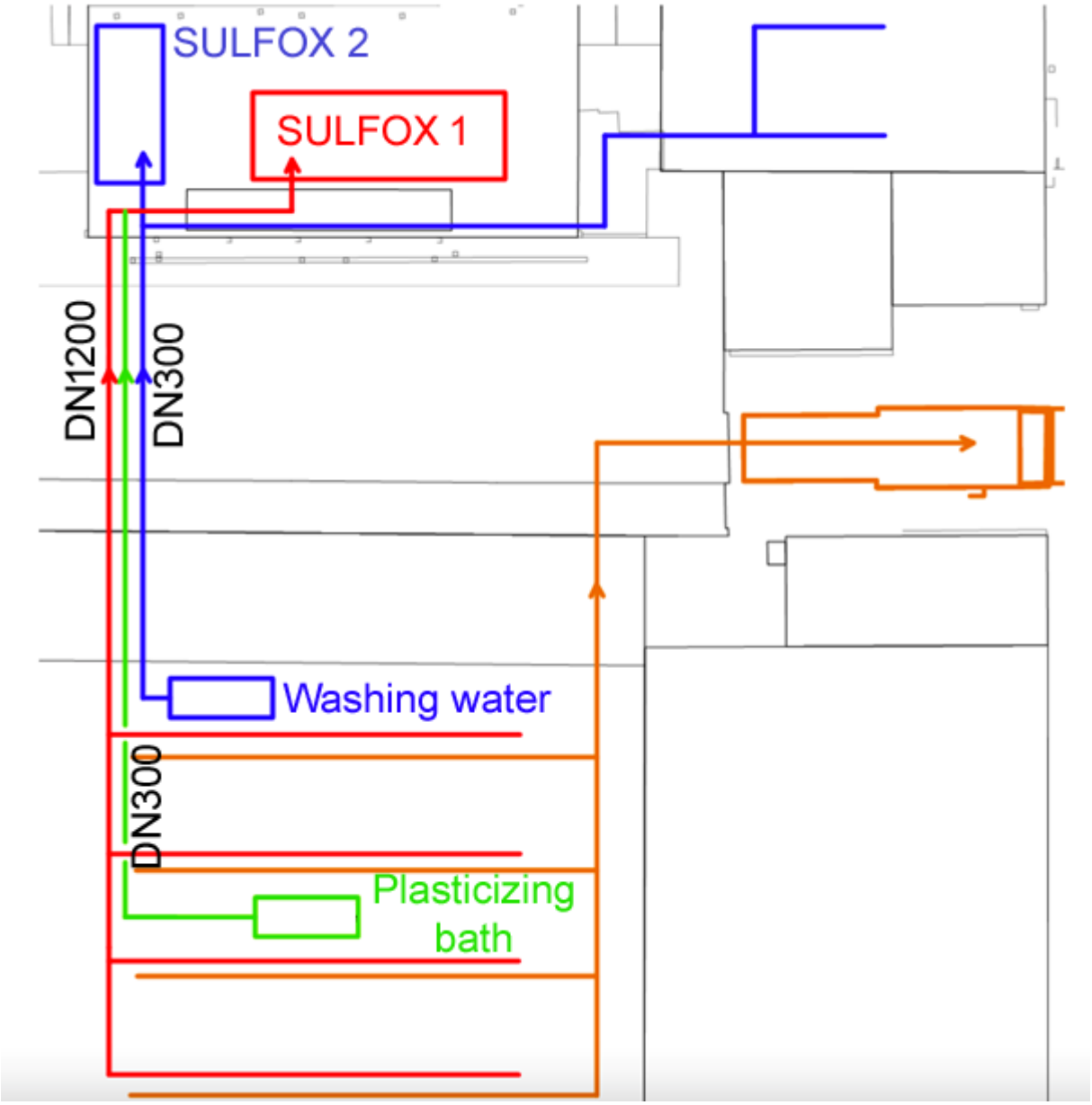

Fig. 10 Air system routing modification

MEASUREMENTS

Air volume balance is measured in key points inside ducts by online embedded anemometer. Readings are monitored in the building management system as shown in figure (Fig. 11). The other pipes have sampling points where a portable digital anemometer gets plugged in. The values are read and recorded manually. Testo 440 devices are used for these measurements (operating temperature range -40 – 150 °C, accuracy at 22 °C ± 0.5 %, volumetric flow rate 0.3 to 35 ms^{-1}; accuracy: ± 0.1 ms^{-1} + 1.5 % of measured value, resolution: 0.01 ms^{-1}). This instrument for air conditioning and ventilation enables long-term measurements with recording. Second measuring device used is MultiRAE (operating temperature range -20 – 50 °C, measuring range 0 – 5000 ppm at resolution 0.1 ppm, sensor sensitivity ±10 % of test gas concentration used), which is a portable chemical detector with six gas sensors. It gets used to determine concentrations of sulfur compounds.

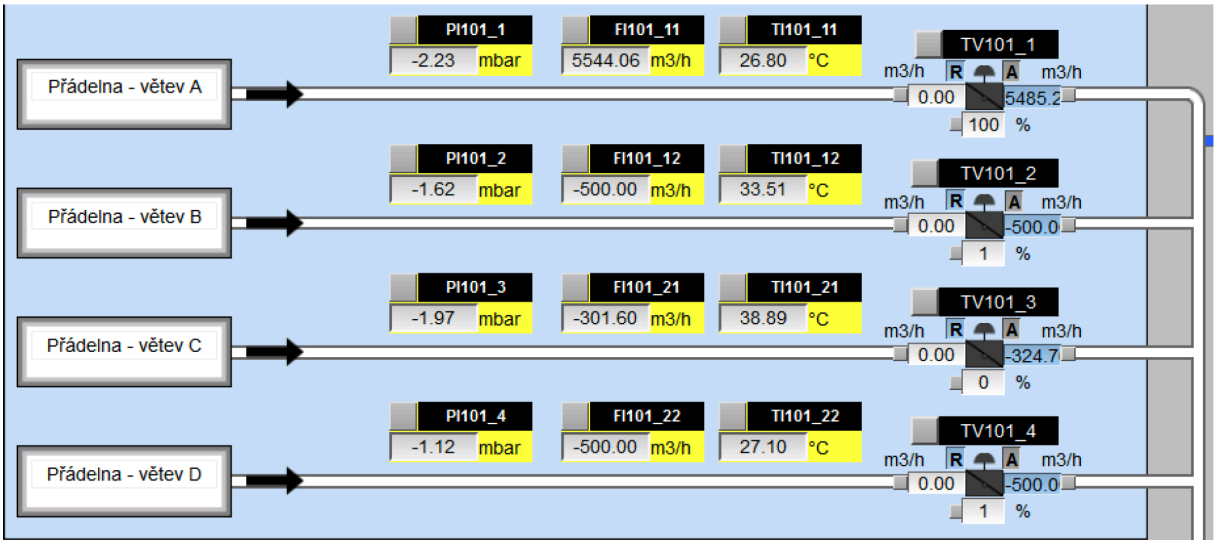

Fig. 11 Visualization of continuous air measurements in building management system

RESULTS AND DISCUSSION

As part of the optimization, the solution had been tested on machines with implemented coverage modification. The design change will be implemented on the entire cord spinning mill technology. The conceptual change also includes a change in connection of the air duct for venting plasticizing bath and venting washing water system, which are already in place.

Testing had been carried out on technology of high and low gas concentration ducts inside the machines specifically area of emissions where sulfur gas evaporates. In the bottom part of the machine, where measurements took place, the readings measured are as shown in table (Tab. 1). Then in the top part of the machine, where measurements took place as well, readings obtained are as shown in table (Tab. 2).

Tab. 1 Testing the machine with modified cover on side of high sulfur gas concentrations

	Before	After	Difference
CS_2 [mg·m^{-3}]	1296.9	4002.9	2706
Rich concentration stream [m^3·h]	450	450	
CS_2 [kg·h^{-1}]	0.583605	1.801305	1.2177

By carrying out the system modification test and subsequent measurements, the table shows an increase in mass flow of carbon disulfide towards regeneration. As a matter of verification, another set of readings had been carried out on duct with low concentrations of sulfur gas. In this test, as can be seen from table (Tab. 2), there is a gas concentration reduction visible. It decreased by almost the same value as it increased on the opposite side where high concentrations of sulfur gas are present. From the performed measurement, it can be concluded that there is gain in form of increased gas yield approximately by 4000 mg·m^{-3}.

Tab. 2 Testing the machine with modified cover on side of low sulfur gas concentrations

	Before	After	Difference
CS_2 [mg·m^{-3}]	527	390	-137
Rich concentration stream [m^3·h]	9000	9000	
CS_2 [kg·h^{-1}]	4.743	3.51	-1.233

BALANCE IN AIR DUCTS AT THE CORD FIBER SPINNING MILL

The balance of air mass movements presents a comparison of measured values in air-system routes. The following tables show measured values in the respective measuring points of ducts in direction to SULFOX facility. The readings in table (Tab. 3) represent condition before implementing the modified coverage for entire technology of the cord fiber spinning mill. Table (Tab. 4) represents condition after implementing the solution to the whole technology in operation of the cord fiber spinning mill. The distribution of volumetric flow rate together with concentrations gets equalized thanks to solving hydraulic congestion issues in the air system.

Tab. 3 CS_2 mass flows before coverage

Route	Designation	Volumetric flow rate [m^3·h^{-1}]	Concentration [mg·m^{-3}]	Mass flow CS_2 [kg·h^{-1}]
Plasticization outgassing	$m_{PL_{CS_2}}$	5300	6858	36.35
Air removal from washing water	$m_{PV_{CS_2}}$	4700	1951	9.17
Row A	$m_{A_{CS_2}}$	5500	1300	7.15
Row B	$m_{B_{CS_2}}$	4900	1300	6.37
Row C	$m_{C_{CS_2}}$	5100	1300	6.63
Row D	$m_{D_{CS_2}}$	4500	1300	5.85
SULFOX 1	$m_{SX1_{CS_2}}$	30000	2384	71.52

Tab. 4 CS_2 mass flows after coverage

Route	Designation	Volumetric flow rate [m^3·h^{-1}]	Concentration [mg·m^{-3}]	Mass flow CS_2 [kg·h^{-1}]
Plasticization outgassing	$m_{PL_{CS_2}}$	5300	6858	36.35
Air removal from washing water	$m_{PV_{CS_2}}$	4700	1951	9.17
Row A	$m_{A_{CS_2}}$	5000	4000	20
Row B	$m_{B_{CS_2}}$	5000	4000	20
Row C	$m_{C_{CS_2}}$	5000	4000	20
Row D	$m_{D_{CS_2}}$	5000	4000	20
SULFOX 1	$m_{SX1_{CS_2}}$	30000	4184	125.52

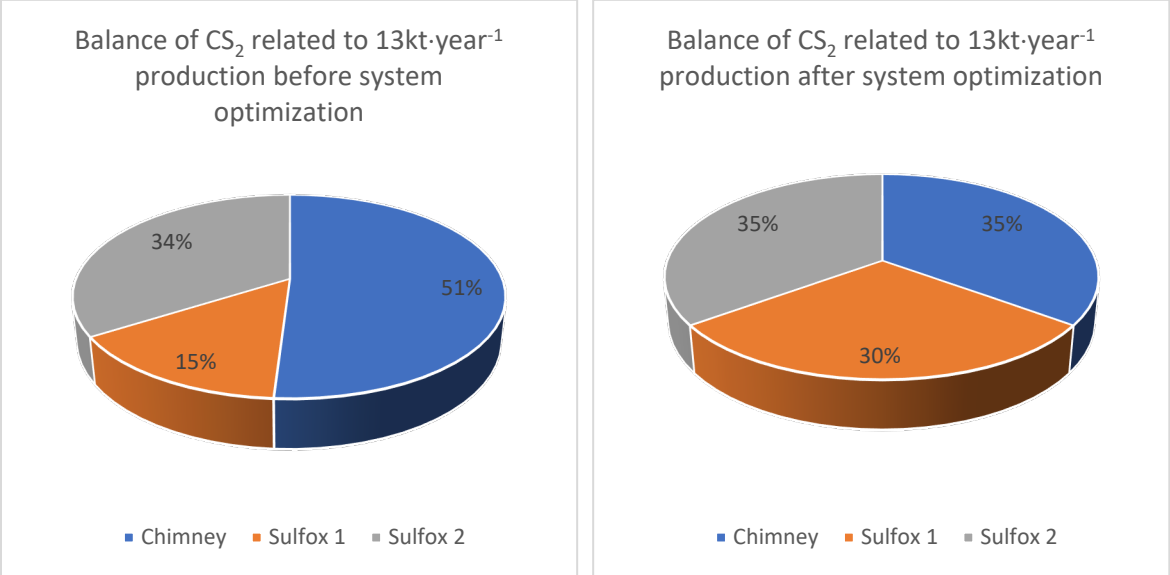

Fig. 12 Comparison of CS_2 balance before and after implementing system optimization

An increase in mass flow of carbon disulfide towards SULFOX facility is visible from the balance for year-round production, which is around about 13 kt. An increase in regeneration proportion of carbon disulfide will cause a decrease in released polluting emissions to atmosphere from 397 $mg \cdot m^{-3}$ to 276 $mg \cdot m^{-3}$. The stream with rich sulfur gas concentrations will increase from 2384 $mg \cdot m^{-3}$ to 4184 $mg \cdot m^{-3}$.

Tab. 5 Final balance of emissions

	CS_2 concentration at chimney [$mg \cdot m^{-3}$]	Mass flow of CS_2 to chimney [$kg \cdot h^{-1}$]	Mass flow CS_2 on the chimney [$t \cdot year^{-1}$]
Before	397	237.43	2022.9
After	276	183.64	1505.9
Difference	-121	-53.79	-517

It is assumed there will be reduction in consumption of natural gas from 110 $m^3 \cdot h^{-1}$ to 60 $m^3 \cdot h^{-1}$, due to a greater amount of exothermic heat generated during catalytic oxidation thanks to a higher sulfur gas content heading towards SULFOX unit. Looking at the balance in the cord fiber spinning mill machine, the total sulfur content for regeneration changed from 49% to 65%. The mass flow of carbon disulfide towards chimney and further into the atmosphere will decrease from 237 $kg \cdot h^{-1}$ to 183 $kg \cdot h^{-1}$. In the annual total, a reduction from 2 022 940 kg to 1 505 895 kg will be obtained after implementing the solution throughout the whole cord fiber spinning mill technology. Absolutely, then 517 045 kg less emissions of carbon disulfide into the atmosphere during a year of operation of the facility.

CONCLUSION

By changing the air venting system of cord fiber spinning mill technology and especially thanks to new design of covering machines both on dry and wet side, the efficiency of venting evaporated sulfur gas dedicated for regeneration increases.

- New concept redirects 2706 $mg \cdot m^{-3}$ more gas compared to the original state into regeneration facility.
- After implementing the solution throughout the whole cord fiber spinning mill facility, a 16% higher yield of regenerated sulfuric acid is expected to be obtained compared to the original concept.
- The technological change will result into significant decrease of polluting emissions. Specifically, 517 045 kg (at 13kt product per year) less carbon disulfide to be released into atmosphere per year of operation of the cord fiber spinning mill facility.

REFERENCES

Chaaban, M. A. (2001). Hazardous waste source reduction in materials and processing technologies. *Journal of Materials Processing Technology*, *119*(1–3), 336–343.

Hall, D. S., & Losee, L. A. (1997). Carbon disulfide incidents during viscose rayon processing. *Process Safety Progress*, *16*(4), 251–254.

Hossain, K. A., Khan, F. I., & Hawboldt, K. (2008). Sustainable development of process facilities: State-of-the-art review of pollution prevention frameworks. *Journal of Hazardous Materials*, *150*(1), 4–20.

King, M. J., Davenport, W. G., & Moats, M. S. (2013a). Making sulfuric acid from wet feed gas. *Sulfuric Acid Manufacture*, 283–294.

King, M. J., Davenport, W. G., & Moats, M. S. (2013b). SO2 oxidation catalyst and catalyst beds. *Sulfuric Acid Manufacture*, 91–101.

Klemeš, J. J., & Varbanov, P. S. (2018). Heat transfer improvement, energy saving, management and pollution reduction. *Energy*, *162*, 267–271.

Li, Y., Peng, J., Liu, X., Song, D., Xu, W., & Zhu, K. (2021). Dissolving waste viscose to spin cellulose fibers. *Polymer*, *237*, 124349.

Majumdar, D., Bhanarkar, A., Rao, C., & Gouda, D. (2022). Carbon disulphide and hydrogen sulphide emissions from viscose fibre manufacturing industry: A case study in India. *Atmospheric Environment: X*, *13*, 100157.

Mondal, S., Dutta, S., Agarwala, P., Nimbalkar, V., & Dhumal, S. S. (2020). Intensification of cellulosic fiber drying through fundamental insights and process modeling. *Drying Technology*, *38*(16), 2151–2161.

Huang, L. X., & Han, Y. H. (2014). Industrial restructuring and emission reduction. *Advanced Materials Research*, *869–870*, 777–780.

Sayyed, A. J., Deshmukh, N. A., & Pinjari, D. V. (2019). A critical review of manufacturing processes used in regenerated cellulosic fibres: viscose, cellulose acetate, cuprammonium, LiCl/DMAc, ionic liquids, and NMMO based lyocell. *Cellulose*, *26*(5), 2913–2940.

Seferlis, P., Varbanov, P. S., Papadopoulos, A. I., Chin, H. H., & Klemeš, J. J. (2021). Sustainable design, integration, and operation for energy high-performance process systems. *Energy*, *224*.

Shen, L., Worrell, E., & Patel, M. K. (2010). Environmental impact assessment of man-made cellulose fibres. *Resources, Conservation and Recycling*, *55*(2), 260–274.

SULFOX - SYSTEM FOR SULFIDE POLLUTION-CONTROL-Web of Science Core Collection. (n.d.). Retrieved December 4, 2021

Tan, X., Wang, F., Bi, Y., He, J., Su, Y., Braeckman, L., De Bacquer, D., & Vanhoorne, M. (2001). Carbon disulfide exposure assessment in a Chinese viscose filament plant. *International Journal of Hygiene and Environmental Health*, *203*(5–6), 465–471.

Varbanov, P. S., Jia, X., & Lim, J. S. (2021). Process assessment, integration and optimisation: The path towards cleaner production. *Journal of Cleaner Production*, *281*.

Wang, F., Wang, J., Ren, J., Li, Z., Nie, X., Tan, R. R., & Jia, X. (2020). Continuous improvement strategies for environmental risk mitigation in chemical plants. *Resources, Conservation and Recycling*, *160*, 104885.

Xu, Q., Li, H., & Li, Q. (n.d.). *Sustainable development of industry and economy : selected, peer reviewed papers from the 3rd International Conference on Energy, Environment and Sustainable Development (EESD 2013), November 12-13, 2013, Shanghai, China*. 1176.

Yong, J. Y., Klemeš, J. J., Varbanov, P. S., & Huisingh, D. (2016). Cleaner energy for cleaner production: Modelling, simulation, optimisation and waste management. *Journal of Cleaner Production*, *111*, 1–16.

Zivkovic, S., Vukadinovic, B., & Veljkovic, M. (2018). Cleaner and energy efficient production: A case study. *Environmental Engineering and Management Journal*, *17*(1),175–188.

Numerical and experimental analysis of hybrid composites partially reinforced with bio-fibers and fillers

C. Vijay[1], R. K. Mishra[1], V. Kolář[1], P. Jirků[1], M. Müller[1]

[1]Department of Material Science and Manufacturing Technology, Faculty of Engineering, Czech University of Life Sciences Prague, Kamycka 129, Suchdol, 165 00 Prague, Czech Republic

Abstract

The current work is focused on numerical and experimental studies on woven fabric composites by hybridization with biological (cellulosic) filler materials. The mechanical performance is characterized under tensile, bending and impact loads and the effect of hybridization is observed with respect to pure and nonhybrid composites. Numerical models were developed using computational tools to predict the mechanical performance under tensile loading. The results of computational prediction are compared and validated with relevant experimental results. This research is aimed at understanding the mechanical performance of basalt-epoxy composites partially reinforced with micro/nano sized bio-fillers from cellulose intended for various application areas. Different weave structures e.g., plain, twill and matt etc. were investigated with respect to mechanical properties of hybrid composites. The effect of hybridizing with cellulose particles and weave pattern of basal fabric is studied. In general, the use of high strength fibers like basalt along with cellulosic fillers up to 3% of weight improves the mechanical performance of the hybrid structures. Thermomechanical performance of hybrid composites improved significantly by using basalt fabric as well as 3% of cellulosic fillers. Results reveal advantages of hybridization and inclusion of natural cellulosic fillers in the hybrid composite structures. The material developed is suitable. for high end applications in the components for construction which demand advanced mechanical and thermomechanical performance. Furthermore, the inclusion of biodegradable fillers fulfils the objectives of sustainable and ecological construction materials.

Key words: hybrid composites; cellulosic/bio fillers; basalt woven fabrics; mechanical properties; modulus

INTRODUCTION

Polymer based composite materials have developed wider significance in many areas of application in the current time. The research in this area is gaining more and more importance (Abrate et al., 1994), (Kretsis et al., 1987). Experimental investigation is somehow successful however, it is not simple to predict the performance of final composite product accurately (Wang et al., 2012), (Güneş et al., 2020), (Swolfs et al., 2014).

Woven fabrics are used as reinforcement in composites because of their symmetry and balanced properties in the fabric plane as well as their easiness in handling during fabrication of composites. However, the structure being two dimensional in geometry, these fabrics show poor mechanical properties in thickness direction and their reinforcement in composites results in relatively lower impact properties (Tehrani-Dehkordi et al., 201), (Simić et al., 2022). In order to achieve better impact performance of composites, significant work has been done on increasing the thickness of fabrics by engineering the woven structures or simply by layering the 2D fabrics. Despite increased thickness after layering, previous studies pointed out no clear trend in improvement of impact properties because of delamination of individual layers (Zhang et al., 2013), (Sarasini et al., 2013), (Stavrakis et al., 2021). Recently an idea of filling micro/nanofillers in composites is being practised to improve the delamination resistance of composites but at the increased cost of additional filler material. Therefore, in last few years hybrid composite structures have created a lot of interest in technical applications where properties in thickness direction are extremely important (Sinha et al., 2022), (Stavrakis et al., 2022), (Sinha et al., 2023), (Sinha et al., 2022).

Basalt fibers have been used in composite materials due to their advanced mechanical, thermal and thermomechanical performance (Jamshaid et al., 2015), (Li et al., 2016), (Wang et al., 2008), (Amuthakkannan et al., 2012). Since they are derived from minerals, they are considered as an eco-friendly alternative to high performance synthetic fibers used in composite industry. There is limited literature which indicates an in-depth study of basalt based composite materials in polymer matrices (Azadi et al., 2021).

Since the fibrous/textile-based reinforcement does not provide enough orientation of fibers in the thickness direction, there is an inferior mechanical performance in the bulk direction. By plying several layers of fabrics, one cannot completely eliminate the risk of delamination under severe mechanical loading conditions. Therefore, one of the alternative ways is to combine or hybridize fibrous reinforcement with filler materials. Thus, the mechanical, thermal and thermomechanical performance can be controlled and improved also in the bulk/thickness direction (Kariz et al., 2018), (Yao et al., 2019) (Daver et al., 2018), (Tanikella et al., 2017). Hybrid composites in several instances have offered improved impact resistance under low velocity loading (Tiwary et al., 2020), (Mishra et al., 2020). They can be engineered in order to provide enough mechanical performance in the preferential direction.

The cost factor associated with high performance fibers can be compensated by hybridization with low-cost biological materials e.g., cellulosic waste from plant products (Pincheira et al., 2015). The hybrid effect can complement the performance of the fibers and the fillers (Baghaei et al., 2015), (Sezgin et al., 2016). Such practice is common in metallurgy but so far not much research is reported in the area of hybridizing high performance fibers and cellulosic fillers in a polymer composite (Lee et al., 2017), (Rajasekar et al., 2018), (Swolfs et al., 2015), (Gomez et al., 2021).

Epoxy resins are popularly used in composite applications as they do not give off reaction products while curing and have low cure shrinkage (Baek et al., 2020). They show a few

outstanding characteristics such as high strength and stiffness, good chemical and electrical resistance besides very good adhesion to fibres and inorganic substrates (Minchenkov et al., 2021), (Bandaru et al., 2017), (Minchenkov et al., 2022). However, because of their brittle nature they have poor crack resistance and low impact strength. Therefore, in the last few decades toughening of epoxies has received much attention (Cerit et al., 2016). There are several methods to overcome brittleness of epoxy resins. It can be done by using chemical modifiers (Ahmetli et al., 2015), by reducing the cross-linking density of the epoxy network or by modifying the epoxy resin with secondary components e.g., bio-fillers (Subagia et al., 2017), (Vedernikov et al., 2022), (Zhou et al., 2022). A simple and effective way to improve fracture energy without loss of strength and elastic modulus is via incorporating micro/nano sized fillers like cellulosic fillers. Thus, the role of cellulose could also be studied in improvement of toughness of epoxy besides delamination resistance (Pavlovski et al., 2007).

The interfacial bond between textile fabric reinforcement and the composite matrix is highly heterogeneous owing to orientation of fibers/yarns in x and y direction. Therefore, it is essential to characterize the bond behaviour in order to understand the macroscale behaviour of a fiber reinforced composite material (Aji et al., 2011). Several researchers have reported the advantages of textile fibers and woven fabrics on mechanical performance of composite materials. However, the influence of hybridizing woven structures with micro/nano fillers is not experimented extensively (Banea et al., 2011), (Muller et al., 2022), (Jarukumjorn et al., 2009).

The primary objective of this work is to study the role of various basalt fabric constructions engineered for improvement of properties of composites in thickness direction vis-à-vis to those composites designed after hybridization with micro/nano cellulosic fillers. The second objective is utilisation of bio-origin, low-cost fillers like cellulose for improvement of tensile, bending as well as impact performance in hybrid composites. The investigations are focused on reinforcement of basalt woven fabrics with plain, twill and matt constructions. Numerical modelling was done for the tensile performance of the developed composites and the predicted results were compared with experimental data. The combined effect of a varying weave structure and an optimized concentration of cellulosic fillers is investigated so as to develop hybrid composite samples with enhanced mechanical and thermomechanical performance.

MATERIALS AND METHODS

MATERIALS

Basalt is a fiber originated from rocks and having excellent mechanical and thermal performance. The basalt yarns were sourced from Kamenny Vek (KV) (North Carolina, USA). The details of fibers and yarns are given in table (Tab. 1).

Tab. 1 Properties of fibers and yarns used.

Properties	Basalt
Diameter of fibers (micron)	12
No. of filaments	890
Linear density of yarn (Tex)	296
TPM (Twists/meter)	20 ± 1
Tensile strength (N)	92.75 ± 3.54
Tensile elongation (%)	1.29 ± 0.03
Tenacity (N/tex)	0.315 ± 0.01
Initial modulus (MPa)	9,378 ± 32

Green epoxy resin CHS-G530 (new commercial name EnviPOXY®530) was purchased from company SPOLCHEMIE in Ústí nad Labem, Czech Republic. Chemically it contains 4,4'-Isopropylidenediphenol, oligomeric reaction products with 1-chloro-2-3-epoxypropane. It is called "green" due to obtaining 1-chloro-2-3-epoxypropane (epichlorohydrine) from glycerine originating from waste generated at biodiesel production. The properties of epoxy resin are given in table (Tab. 2).

Tab. 2 Properties of green epoxy resin.

Properties	Value
Physical State	Liquid at 20 °C
Color	Yellowish to Yellow
Boiling Point	270–280 °C (at very low pressure)
Density (g/cm^3)	1.16 at 20 °C
Water Solubility (g/L)	6–9 at 20 °C
Viscosity (Poise)	8–10 at 25 °C
Solubility	Soluble in Acetone
Storage Temperature	5–25 °C
Epoxide Index (mol/kg)	5.4–5.7
Mass Equivalent of Epoxide, EEW (g/mol)	176–186
Color (Hz, G*)	Max. 100
Hydrolyzable Chlorine Content (%)	Max. 0.03
Non-Volatile Substances (2 h/140 °C)	Min. 99.5%

METHODS

The basalt fabrics were made on the CCI sample loom (CCI, Taiwan) with the same thread density for all fabric structures. 12 threads/cm in warp and 8 threads/cm in weft were maintained. The weave structures are shown in figure (Fig. 1).

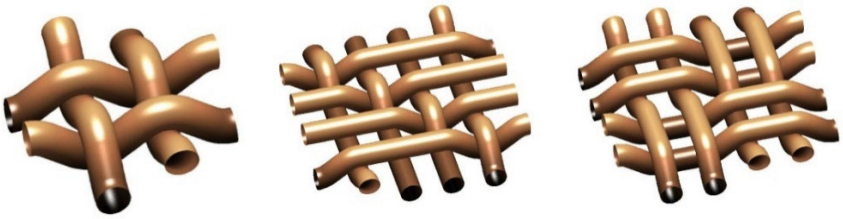

Fig. 1 Fabric structures developed.

PREDICTION OF TENSILE PROPERTIES USING NUMERICAL/COMPUTATIONAL MODELS

The software package WiseTex (Leuven, Belgium) was used to predict the mechanical performance of composites with various fabric structures. It is a computational tool for modelling of the internal geometry and mechanical properties of composite structures. Internal geometry of textiles is based on the hierarchical principle of textile geometries. The simulation algorithm uses the minimum energy principle, calculating the equilibrium of yarn interactions in the composites. The models cover wide range of structures, either relaxed or after compression, shear or tensile deformation. The model was developed for the internal geometry of plain, twill and matt weaves (Sahu et al., 2017), (Sen et al., 2010), (Ayrilmis et al., 2010), (Ruggiero et al., 2016), based on a minimum number of binding elements (weave style, inter-yarn distance) and yarn mechanical properties. The model is a mechanical model, as it applies a minimization algorithm to yarn deformation energy in order to define the internal geometry of any weave and then to predict mechanical performance of composites.

GRINDING OF MICRO CELLULOSE BY BALL MILLING

Cellulose micro fillers were obtained from Havel composites, (Svésedlice, Czech Republic). The cellulose micro particles were subjected to mechanical grinding in a ball milling device, Fritsch Pulverisette 7 (Kyjov, Czech Republic). The material was grinded for upto 5 hours in order to obtain the nanosized fillers. The nano fillers were dispersed in deionised water. Bandelin ultrasonic probe (Merck Life Science spol. s r.o., Prague, Czech Republic) was used for mixing the dispersion before characterisation of particle size. The cellulosic nanofillers were dried in an oven at 120°C for 6 hours.

FABRICATION OF HYBRID COMPOSITE SAMPLES BY HAND LAYUP PROCESS

The composites samples were developed by hand layup method maintaining a 50:50 weight ratio of fabric to matrix. While using cellulosic fillers, the weight fraction of epoxy resin was reduced proportionally but fabric weight fraction was 50%. Weighed amounts of dried cellulose fillers in 1, 3, 5 & 10 wt% were mixed with epoxy resin at room temperature in order to prepare a homogeneous mixture. The mixture was subjected to ultrasonic stirring for 30 minutes using a Bandelin Sonoplus (Merck Life Science spol. s r.o., Prague, Czech Republic) device.

The matrix was prepared with resin, harden and the cellulosic fillers. A mixture of epoxy and hardener (CHS-HARDENER P11, SPOLCHEMIE in Ústí nad Labem, Czech Republic) was prepared as per manufacturer guidelines with a ratio of 100:32 and stirred well for uniform mixing. The viscosity of (resin+hardener) was found to be 10 Poise at 25 °C, viscosity for (resin+hardener+micro cellulose) was 11 Poise and that for (resin+hardener+nano cellulose) was 9 Poise at 25 °C. The decrease in viscosity due to addition of nano particles does not follow Einstein-Stokes equation and is well documented in literature (Ayrilmis et al., 2010), (Ruggiero et al., 201),. In order to develop composite samples, a mold of 20 cm × 20 cm (length × width) and 3 mm thickness was prepared. Fabric layers were placed within the boundaries of the mold. In order to ensure uniform resin application, the spreading was done layer by layer so that the averaging effect will minimize the variation. No visible voids were found in the prepared samples. The mixture was dispensed over the fabric layers in the mold very carefully to ensure uniform distribution of matrix throughout the sample. A Teflon sheet was placed on both sides of the material in order to keep them intact. It was followed by curing of the samples at room temperature for 16 hours. Further the samples were cured for 30 min at 120 °C under 100 bar pressure. After curing under pressure, the thickness was measured for each sample and found to be within the limits. The schematic of hybrid composite sample preparation is shown in figure (Fig. 2).

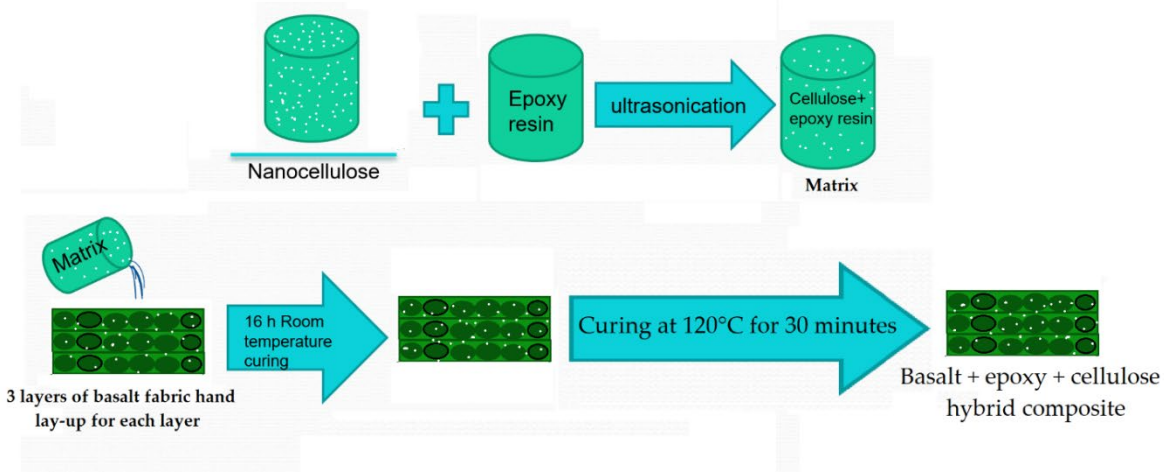

Fig. 2 Schematic of hybrid composite sample preparation.

TESTING OF MECHANICAL PROPERTIES

For testing purpose, the samples were cut using high energy water jet cutting technology (CNC cutting machine AWJ CT 0806). Therefore, no edge errors were detected.

The testing of mechanical properties was carried out on the universal testing machine LABTest 5.50 ST (LABORTECH s.r.o., Opava, Czech Republic), with the measuring unit AST KAF 50 kN (LABORTECH s.r.o., Opava, Czech Republic) and the evaluation software Test & Motion (version 4.5.0.15, LABORTECH s.r.o., Opava, Czech Republic) as per ASTM D3039/D3039M-08 (*ASTM D3039/D3039M-08*, 2014). The tensile test was carried out

at the speed of 12mm/min. A specimen size of 100 mm × 10 mm was used. Each test was repeated 20 times and the average was calculated.

Flexural strength was measured on LABTest 5.50 ST (LABORTECH s.r.o., Opava, Czech Republic), using 500 N capacity load-cell using 3-point bending mode as per ASTM D7264/D7264M-07 (*ASTM D7264/D7264M-07*, 2015). The sample dimensions were entered into the system and the stress-strain curves were recorded for all samples. The specimen size for this test is 100 mm × 10 mm. Bending test for each type of sample was repeated 20 times. Testomeric tester M350-10CT (LABORTECH s.r.o., Opava, Czech Republic) with ball impactor was used to assess the impact resistance of composite samples following ASTM D7136/D7136M-05 (*ASTM D7136/D7136M-15*, 2020). The impactor was allowed to strike the samples using 100kg load-cell at a velocity of 100 m/s. The specimen size for this test is 100 mm × 100 mm. Each test was repeated 20 times and the average was calculated. The experimental set ups for the tensile, bending and impact test are shown in figure (Fig. 3).

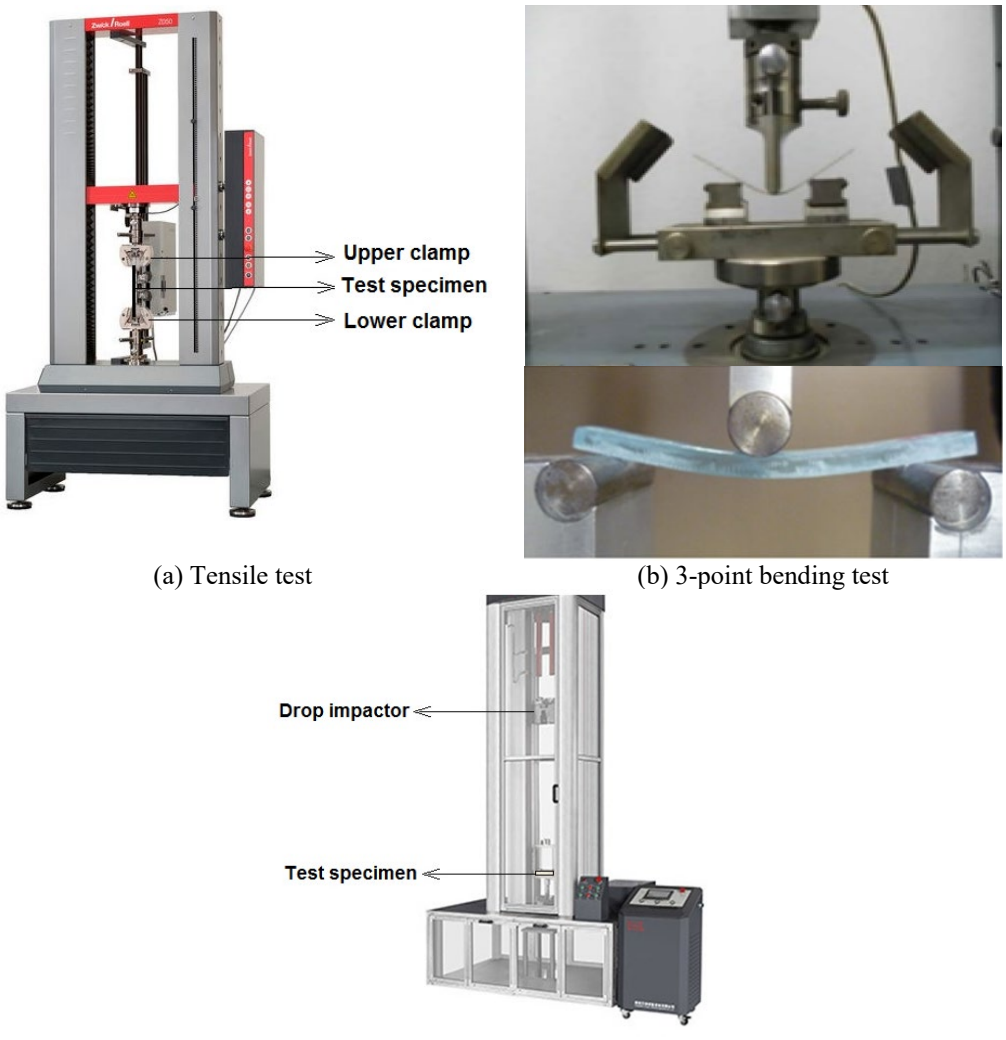

(a) Tensile test (b) 3-point bending test

(c) Drop impact test

Fig. 3 Test set ups for (a) Tensile test, (b) 3-point bending test, and (c) Impact test.

SCANNING ELECTRON MICROSCOPY (SEM) ANALYSIS

SEM analysis was performed using a TESCAN VEGA 3 XMU (TESCAN ORSAY HOLDING a.s., Brno, Czech Republic) The microscopic samples were coated with gold using Quorum Q150R ES Plus (Quorum Technologies - Judges House, Laughton, England).

THERMO-MECHANICAL ANALYSIS (DMA)

The dynamic mechanical analysis of the hybrid composite materials was performed on DMA DX04T RMI instrument (R.M.I., Pardubice, Czech Republic). The test was performed in three-point bending mode with gauge length and sample width of 30 mm and 10 mm respectively. The samples were subjected to an oscillating frequency of 1 Hz and 100 % oscillating amplitude in the temperature range of 30°C to 300°C at the heating rate of 5°C min^{-1}.

RESULTS AND DISCUSSION

EFFECT OF BALL MILLING ON SIZE OF CELLULOSIC FILLER

Figure (Fig. 4 (a & b)) show the SEM images of micro and nanosized cellulosic fillers. It is visible that the spherical shape of the original micro cellulose is broken and an irregular nanoscale filler with higher active surface is obtained. It is established by previous research that a non-spherical and irregular surface of the filler offers much higher specific surface area for better interface with the surrounding matrix (Pakkanen, et al., 2017), (Zhao et al., 2016) (Antonio Travieso-Rodriguez et al., 2020), (Svatik et al., 2021), (Correa et al., 2015), (Mishra et al., 2012). Figure (Fig. 4 (c & d)) show the filler size distribution curves of the milled cellulose for time intervals of 1, 2, 3, 4 and 5 hours respectively. It can be seen that the rate of filler size reduction was greatest during the initial one hour of milling during which the characteristic filler diameter (Z-average) reduced from 3547 nm to 989 nm. However, the filler size was gradually reduced later and reached to 450 nm after five hours of wet milling as shown in figure (Fig. 4 (d)). When milling was performed for longer time, filler size distribution changed from multimodal to near unimodal distribution.

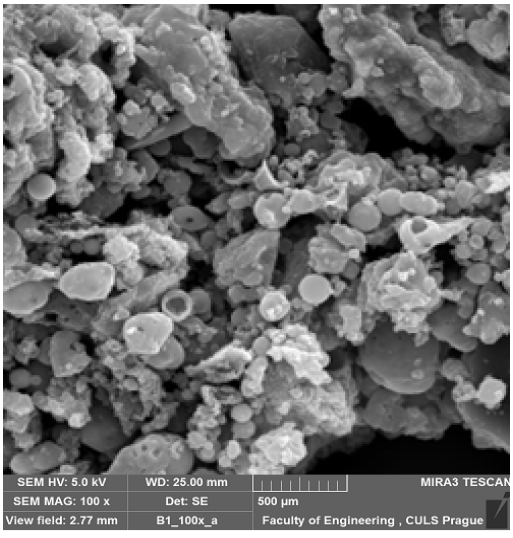

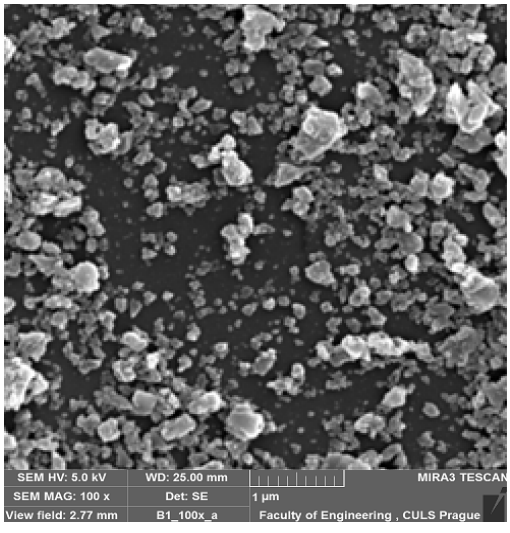

(a) Cellulosic micro fillers

(b) Cellulosic nano fillers

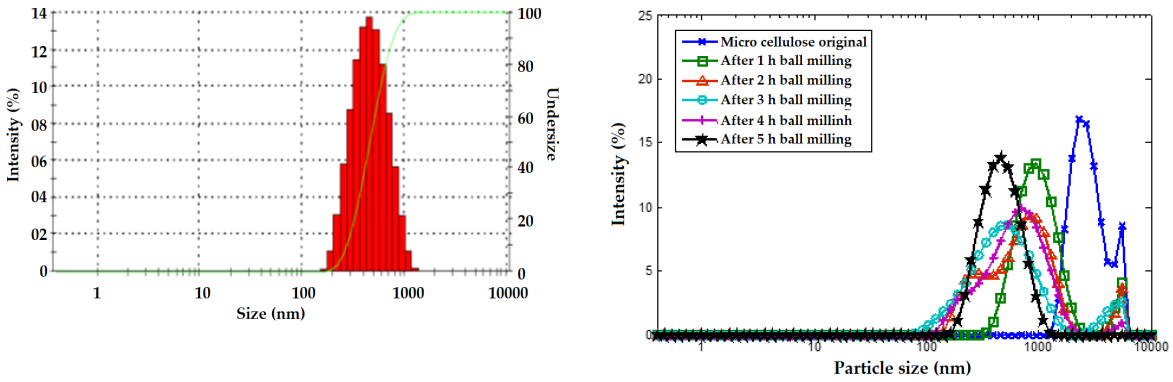

(c) Distribution of filler size after milling

(d) Effect of milling time on filler size

Fig. 4 (a) SEM of cellulosic micro fillers, (b) SEM of cellulosic nano fillers, (c) Distribution of filler size after milling and (d) Effect of milling time on filler size.

NUMERICAL MODELLING OF TENSILE PROPERTIES USING WISETEX

Numerical models were adopted for prediction of tensile properties in composite samples. Woven fabrics are composed of orthogonally interlaced yarn elements, can be further subdivided into basic elemental structures and can be numerically modelled to predict the properties related to structures. Modelling the different weave of fabric as a laminate and computing the equivalent laminate properties results in approximate values for the inplane properties of the fabric. Further the property of the resin is implemented along with the fabric reinforcement for predicting tensile performance of the composites. The Halpin-Tsai model for calculation of basic mechanical properties in a composite is adopted. The tensile properties of the reinforcing fibers and epoxy resin were tested and then the properties of the composite were calculated using rule of mixture and Halpin–Tsai model. The Halpin–Tsai model is widely used to predict the effective tensile strength and modulus for fiber reinforced composites with perfect fiber alignment as reported by several researchers (Tucker et al., 1999), (Halpin Affdl et al., 1976), (Budarapu et al., 2019), (Behera et al., 2007). The details of derivation for the Halpin–Tsai equations are reported in the literature (Behera et al., 2008). The Halpin–Tsai equation has the following form:

$$K_c = K_m \left[\frac{1 + \xi\zeta V_f}{1 - \eta V_f} \right] \tag{1}$$

$$\text{With } \eta = \left[\frac{(K_f / K_m) - 1}{(K_f / K_m) + \zeta} \right] \tag{2}$$

where Kc represents the effective tensile property of the composite while Kf and Km are the corresponding fiber and matrix tensile properties, Vf denotes the fiber volume fraction and ζ is a geometrical parameter, which represents the reinforcement geometry (plain, twill, matt), packing geometry, and loading conditions. In the present analysis, the geometry is defined by

the weave pattern. While predicting tensile properties of samples filled with cellulosic particles, the property of the cellulose filled matrix (epoxy resin + cellulosic filler) was considered.

The tensile modulus of a hybrid composite can be calculated by using rule of mixture if the corresponding values for the constituent fiber and matrix are known. The tensile modulus of a unidirectionally reinforced composite in longitudinal (parallel) direction can be calculated based on Eq. 3.

$$E_c = E_f V_f + E_m (1 - V_f) \qquad (3)$$

Where, Ec represents elastic modulus of the composite, Ef is elastic modulus of fiber, Em is elastic modulus of matrix (epoxy resin + cellulosic filler) and V_f is volume fraction of fiber/fabric in the composite.

The representative models are shown in figure (Fig. 5).

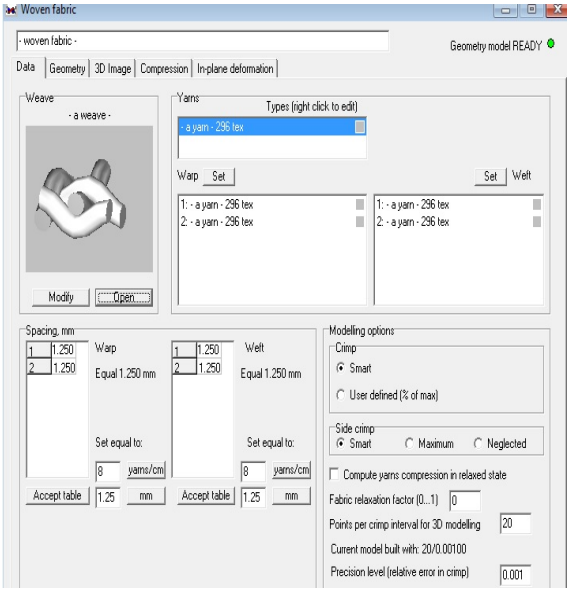

(a) Defining the parameters of fiber and matrix

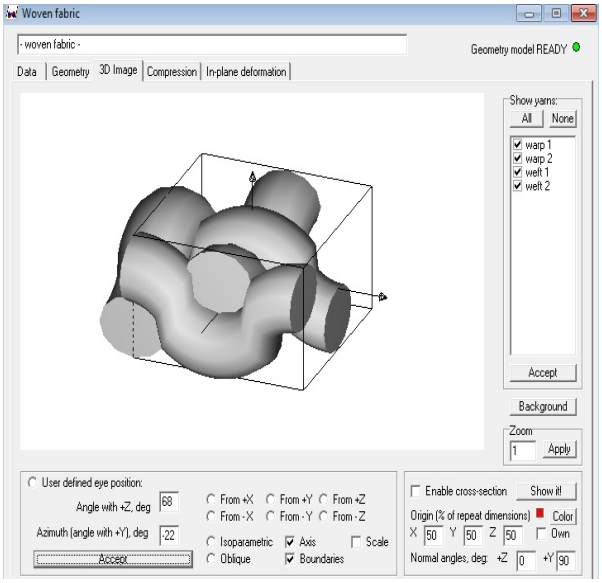

(b) Defining the geometrical parameters

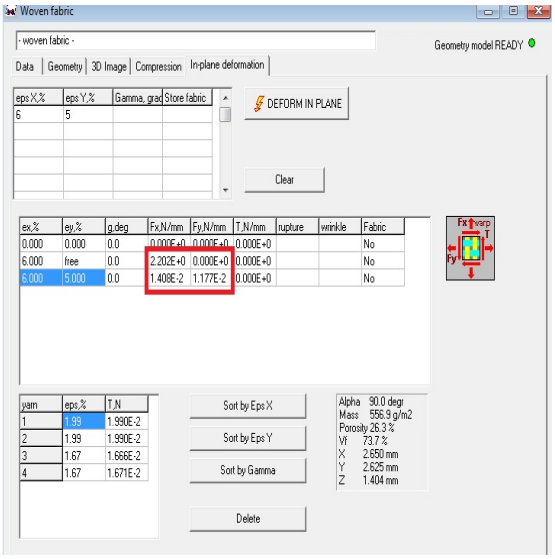

(c) Prediction of tensile properties in composites

Fig. 5 Prediction of tensile properties in composites (a) Defining the parameters of fiber and matrix, (b) Defining the geometrical parameters and (c) prediction of tensile properties in composites.

Samples were prepared with pure resin as well as with cellulosic fillers. For comparison purpose both micro and nano cellulosic fillers were used in 1,3,5 & 10% wt in the matrix based on previous literature (Muller et al., 2022). The purpose was to understand the extent of improvement when the resin is reinforced with the cellulosic filler and then the hybrid effect of fabric as well as cellulosic filler in the resin. The control/reference sample with pure resin was also tested to estimate the % improvement by the hybrid reinforcement. The details of the samples developed are given in table (Tab. 3).

Tab. 3 Details of samples.

Sample No.	Sample code	Description	Fabric wt%	Epoxy wt%	Cellulose wt%
1	ER	Pure epoxy resin	0	100	0
2	BF+ER	Basalt fabric + epoxy resin	50	50	-
3	BF+ER+1%MC	Basalt fabric + epoxy resin + 1% micro cellulose	50	49	1
4	BF+ER+3%MC	Basalt fabric + epoxy resin + 3% micro cellulose	50	47	3
5	BF+ER+5%MC	Basalt fabric + epoxy resin + 5% micro cellulose	50	45	5
6	BF+ER+10%MC	Basalt fabric + epoxy resin + 10% micro cellulose	50	40	10
7	BF+ER+1%NC	Basalt fabric + epoxy resin + 1% nanocellulose	50	49	1
8	BF+ER+3%NC	Basalt fabric + epoxy resin + 3% nanocellulose	50	47	3
9	BF+ER+5%NC	Basalt fabric + epoxy resin + 5% nanocellulose	50	45	5
10	BF+ER+10%NC	Basalt fabric + epoxy resin + 10% nanocellulose	50	40	10

The data obtained from experimental measurement of 20 samples was statistically analysed and the mean values are presented with standard error. The coefficient of variation was found to be within 5% limit; therefore, the results and the differences are statistically significant. The tensile strength and modulus of the samples measured experimentally were compared with the numerical models. The results of tensile test are shown in figure (Fig. 6).

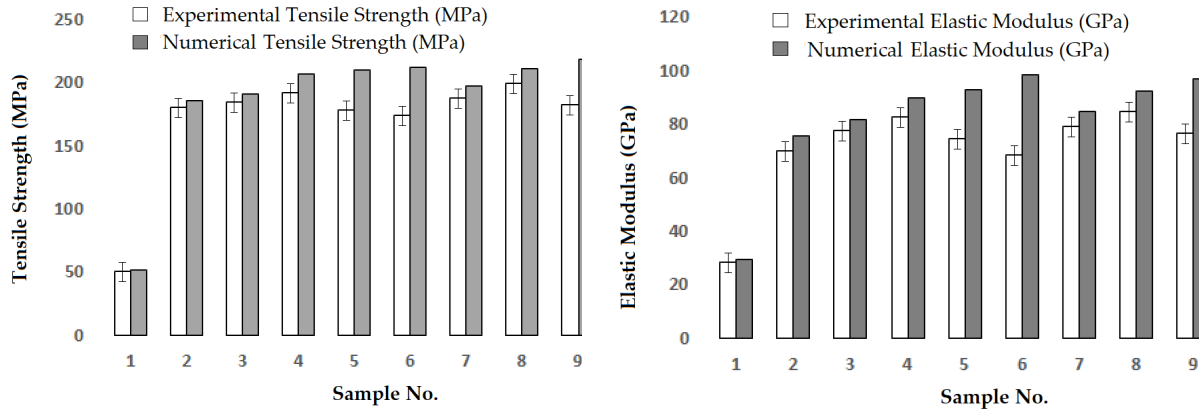

(a) Tensile strength of composite samples

(b) Elastic modulus of composite samples

Fig. 6 Comparison of experimental vs numerical tensile properties of composites (a) Tensile strength, and (b) Elastic modulus.

The numerically calculated values were compared with the measured tensile properties. The experimental tensile strength and elastic modulus were compared with results of the numerical analysis, resulting in a high level of agreement between them. The correlation between numerical and experimental results for tensile strength is 75.25% and the correlation of elastic

modulus was found to be 77.52%. The important reasons for the uncertainty of the results are due to boundary conditions and numerical approximation in the models, which do not consider micro details of the contact between the fibers and the matrix and experimental irregularities and dissimilarities which are unavoidable. It was observed that inclusion of cellulosic micro/nano fillers up to 3% of wt in the matrix improves the tensile strength. However, further increase in the amount of cellulosic fillers rather deteriorates the experimental mechanical properties which are not accurately predictable. by the numerical models. The reason could be due to irregular dispersion of cellulosic fillers at a higher concentration. Further it was observed that milled nano fillers of cellulose are more effective in enhancing the mechanical performance of the hybrid composites as compared to unmilled micro sized cellulosic fillers. This is attributed to enhanced specific surface area when micro fillers are broken into nano fillers during ball milling (Gama et al., 2019), (Senatov et al., 2016), (Essassi et al., 2020), (Yang et al., 2019), (Ayrilmis et al., 2018). Therefore, in the further analysis only milled nanofillers were considered.

SEM FRACTURE SURFACES

The SEM fractographs of the hybrid composites partially reinforced with wet milled cellulosic fillers are depicted in figure (Fig. 7). It can be found that the dispersion of cellulosic fillers in the matrix is good, and the cellulosic fillers disperse well within the matrix except for a few rich regions generated from nonuniform dispersion of cellulosic fillers at higher loadings especially beyond 3%.

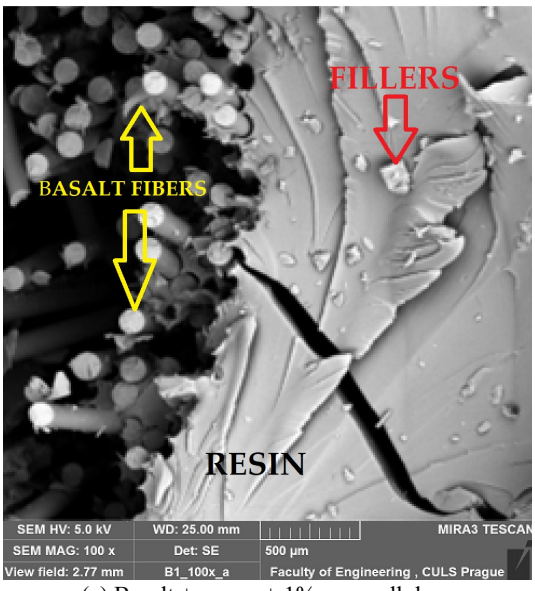

(a) Basalt + epoxy + 1% nanocellulose

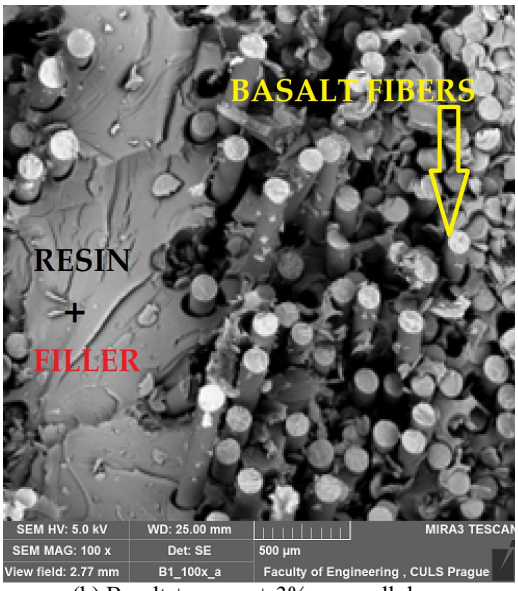

(b) Basalt + epoxy + 3% nanocellulose

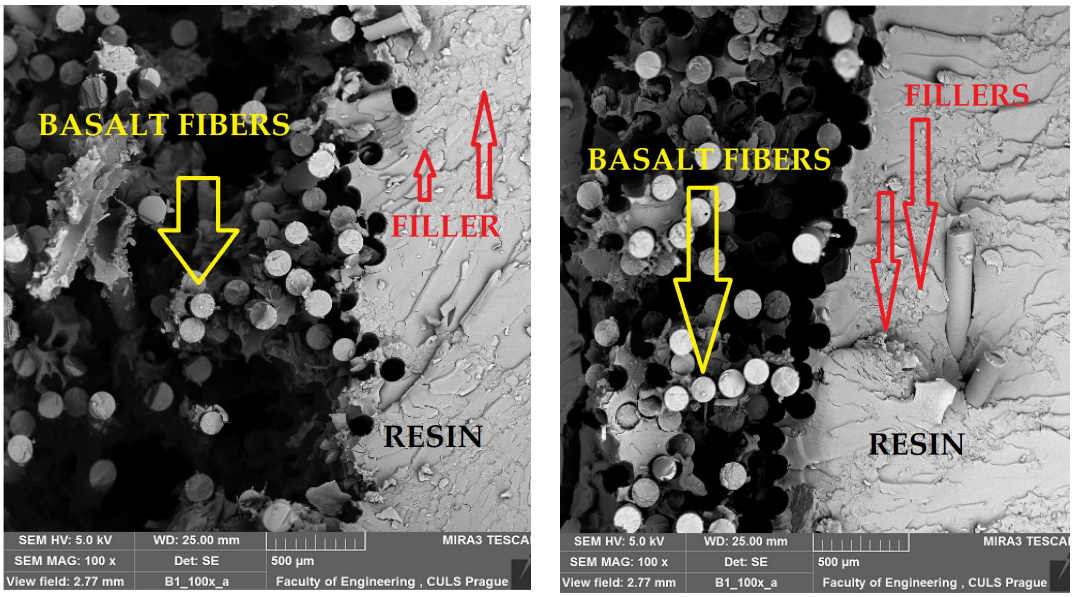

(c) Basalt + epoxy + 5% nanocellulose (d) Basalt + epoxy +10% nanocellulose

Fig. 7 Scanning Electron Microscope (SEM) images of fractured hybrid composites reinforced with cellulosic fillers, (a) 1%, (b) 3%, (c) 5% and (d) 10%.

The basalt fibers, resin and the cellulosic fillers are identified and described in the pictures. Only at 3% filler content, there is adequate bonding between fibers and the matrix, and no visible delamination was found. Fiber matrix interface is optimum at 3% of filler content. The filler and resin separation are visible in the pictures only when there is lack of supersaturation (1% content) or nonuniform dispersion due to high filler content (5% and 10%). This can be a technological error in the production of samples with high filler content. Cellulosic nano fillers are rigid with much higher fracture strength as compared to the epoxy resin. Therefore, the samples reinforced with 3% of fillers did not fracture by the growing crack. A large number of cellulosic fillers were observed on the fractured surface. This indicates that during the process of fracture, the growing crack front, has to change its path many times after interaction with cellulosic fillers, leading to increase in effective crack length and hence, higher absorption of energy in the process of fracture (Yang et al., 2018). A curvilinear tendency for crack progression is seen for hybrid composites partially reinforced with cellulosic fillers. Thus, the total crack length is highest for the 3% cellulose filled hybrid composites and is smallest for 1% cellulose filled composites.

Further, since the addition of 10% cellulosic filler in the matrix was visibly inefficient and ineffective, further analysis of mechanical performance was carried out only for 1%, 3% and 5% nano cellulosic fillers in the hybrid composites.

FLEXURAL TESTS

The flexural stress-strain of composite samples were obtained using 3-point bending test according to standard test method ASTM-D7264. The machine speed was maintained at 1 mm/min and the bending force was exerted on the samples until the value of force reduced to 40% of maximum force (Huber et al., 2008).

The LABTest 5.50 ST (LABORTECH s.r.o., Opava, Czech Republic), universal testing device was used by changing the clamps. It measures the flexural stiffness and strength of polymer matrix composites. The specimens of rectangular shape having dimensions 100 mm × 10 mm were supported at the ends and deflected at the center point. As bending force was exerted, the specimen deflects at the centre. The dimensions of length, width and thickness for each sample were entered into the system. The stress-strain curves were recorded on the system until the maximum force reduced to 40%. For each type of sample 20 measurements were carried out.

The flexural stress-strain curves for hybrid composites partially reinforced with 1%, 3% and 5% nano cellulosic fillers are shown in figure (Fig. 8 (a)). The charts are averaged from 20 measurements for each type of sample. Since the sample with 3% filler exhibited the maximum flexural strength, further analysis was carried out to observe the influence of basalt fabric structure on the hybrid composites reinforced with 3% nanocellulose. The influence of fabric structure on flexural performance is shown in figure (Fig. 8 (b)).

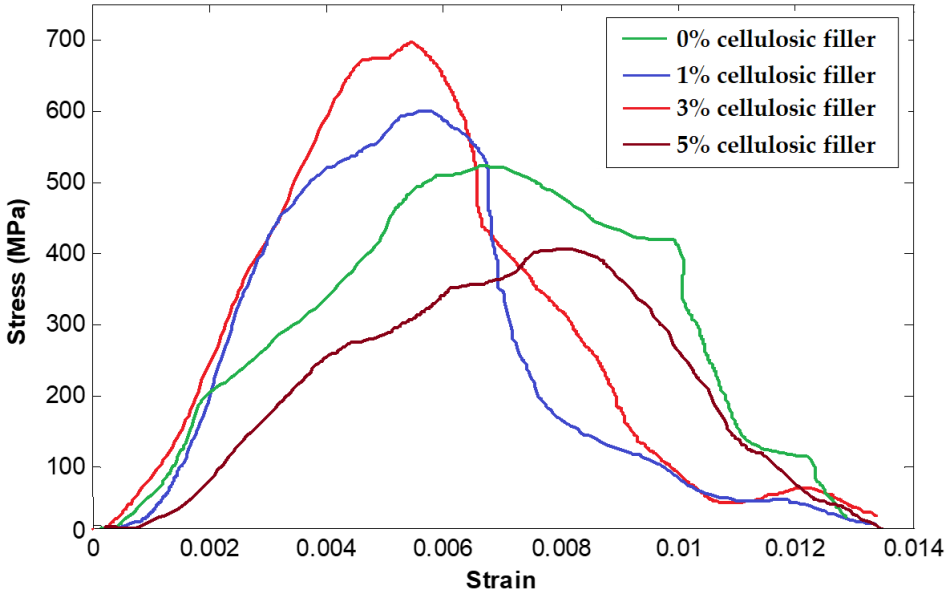

(a) Effect of nano cellulosic filler content

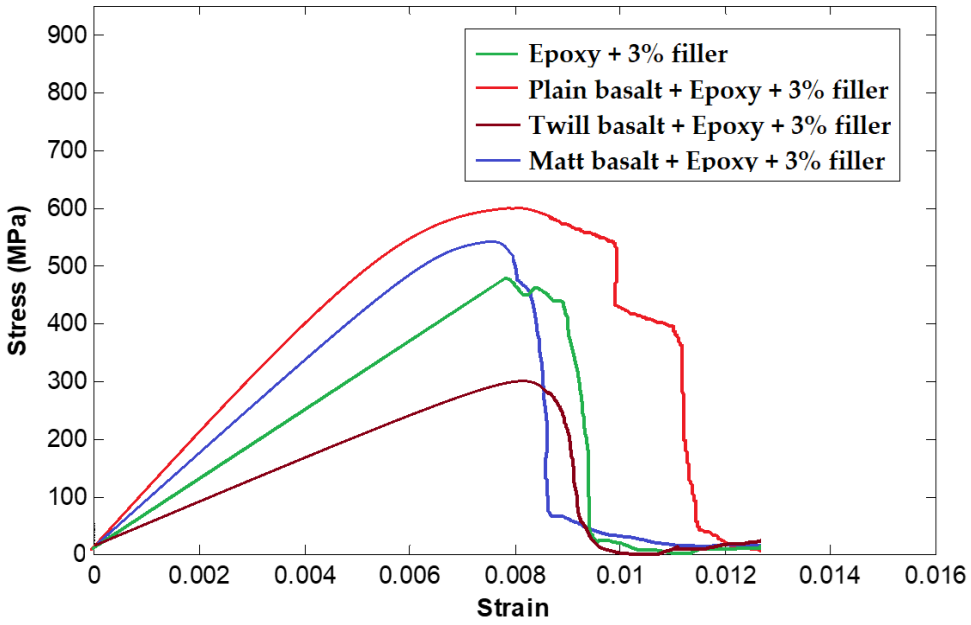

(b) Effect of weave structure at 3% cellulosic filler

Fig. 8 Flexural stress-strain curves for hybrid composite samples (a) Effect of nano cellulosic filler content (b) Effect of weave structure at 3% cellulosic filler.

It can be observed from the figure (Fig. 8 (a)) that flexural strength of composites improved after addition of cellulose nanofillers up to 3% in the epoxy resin. However, addition of 5% cellulose tends to decrease the flexural strength. These observations are supported by the trends obtained in tensile strength of the samples reinforced with cellulosic fillers. The flexural modulus was also observed to increase as the hybrid composites were reinforced with cellulosic fillers up to 3% wt. The high modulus corresponds often to lower strain to break. The interfacial bondage between nano fillers of cellulose with the molecules of epoxy resin is responsible for improved flexural performance (Shahar et al., 2022), (Yao et al., 2020), (Le Duigou et al., 2020). This increased flexural modulus indicates improved toughening of epoxy with addition of cellulose nanofillers. The decrease in strength for the 5% loading of cellulose can be attributed to the nonuniform dispersion due to higher number of nanosized cellulosic fillers. The formed agglomerates might have acted as stress concentration points leading to lower flexural strength and modulus. The results are supported by previous literature (Arockiam et al., 2022), (Le Duigou et al., 2016), (Calì et al., 2020) as well as the trends of tensile strength observed in the hybrid composite sample.

The influence of basalt fabric structure is observed from figure (Fig. 8 (b)). It is well known that the plain weave is stronger as compared to other weave patterns due to intensive interlocking between the constituent yarns. It is evident from the results that plain woven basalt fabric reinforced hybrid composite partially reinforced with 3% nano cellulosic filler performs the best with respect to tensile as well as flexural properties. Among the twill and matt structures, the matt structure presents a tighter construction and better mechanical performance. Therefore, matt woven fabric-based composite performs better than the twill fabric-based

hybrid composites. The directional bias (inclination of twill line) of the fabric results in an imbalanced force distribution and lower tensile and bending performance as demonstrated in several other literature (Wang et al., 2017), (Li et al., 2016), (Chacon et al., 2017), (Ying et al., 2016).

IMPACT TEST

Since the 3% wt of cellulosic filler proved to improve the tensile and flexural performance of the hybrid composites to the maximum extent, further evaluation of impact performance was carried out to examine the effect of fabric structure. Impact tests were carried out for 3% nano cellulose filled hybrid composites reinforced with different basalt fabric structures. Each type of sample was tested 20 times and the mean values were calculated. The stress-strain curves of the impact test for the composite samples are shown in figure (Fig. 9). The charts are averaged from 20 measurements for each type of sample.

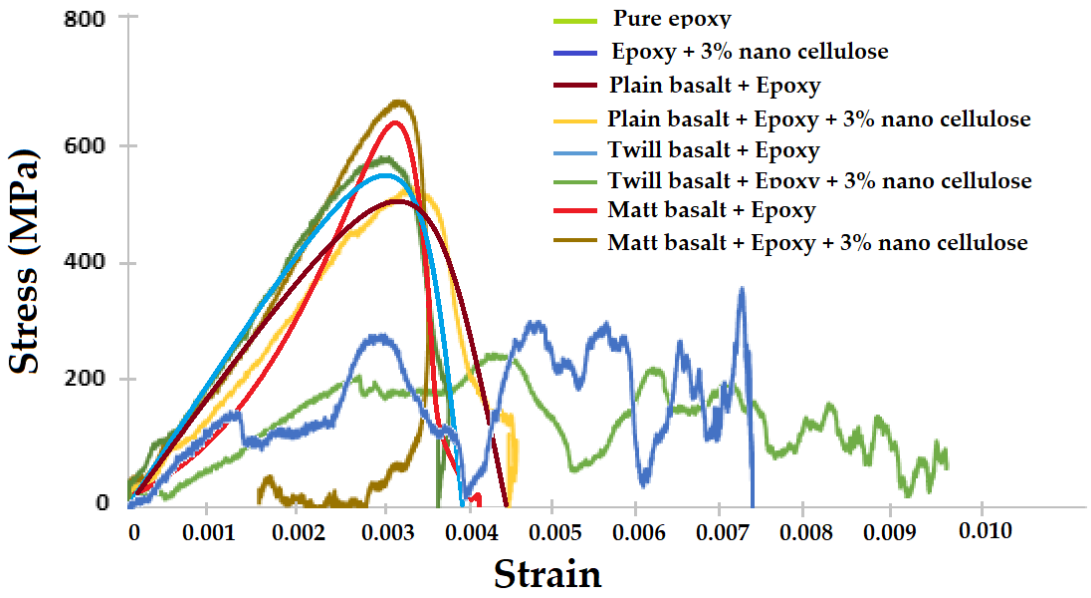

Fig. 9 Impact stress-strain curves for developed composite samples.

The impact strength (load at break) was recorded in the system and the energy at break for various hybrid composite samples reinforced with 3% cellulosic filler was calculated as follows,

$$E = \text{Mass of impactor (m) x acceleration due to gravity (g) x drop height (h)} \quad (4)$$

The results are shown in figure (Fig. 10 (a & b)) respectively. The confidence intervals are based on 20 measurements.

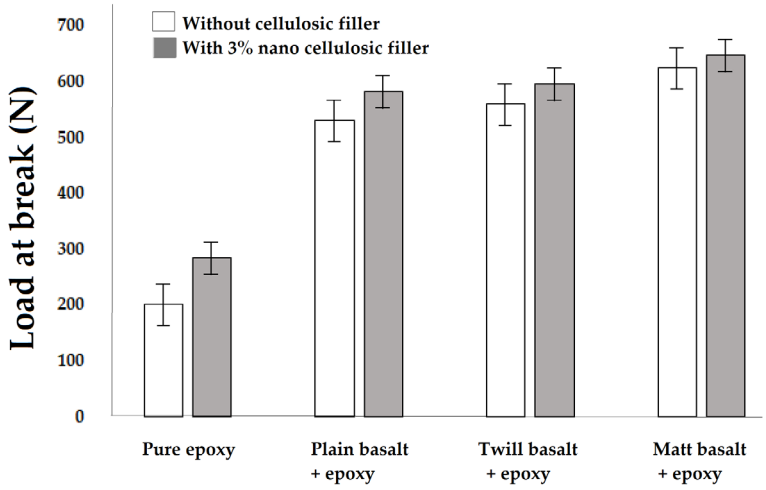

(a) Effect of 3% nano cellulosic filler content on load at break for different weaves

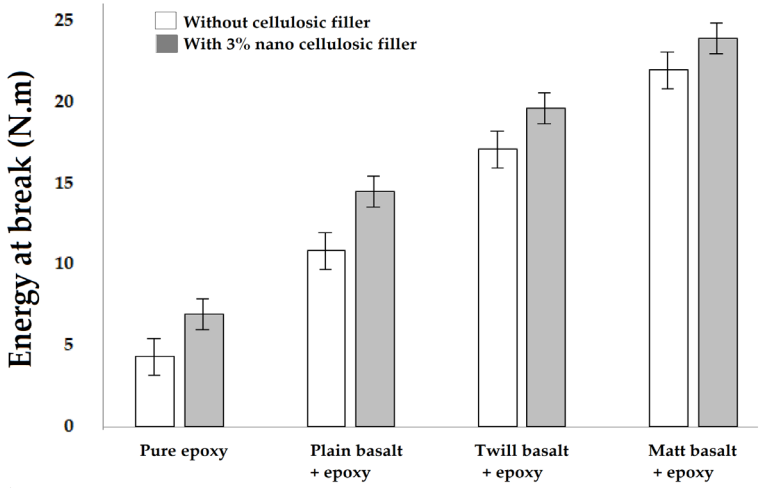

(b) Effect of 3% nano cellulosic filler content on energy at break for different weaves

Fig. 10 Impact performance of hybrid composite samples; Effect of 3% nano cellulosic filler content on (a) load at break and (b) energy at break for different weaves.

It was observed that the impact strength of hybrid composites improved by 6-8% after adding 3% cellulosic fillers as compared with the neat fabric-based nonhybrid composites without filler. The percent increments over pure epoxy resin matrix were found to be 72.02%, 82.22 % and 96.41%, corresponding to various woven constructions e.g., plain, twill, and matt structure of basalt fabrics. These results suggest that the cellulose fillers served as stress concentrators to initiate a multiplicity of small cracks around the particulates in composites, thus absorbing impact energy and diverting the ultimately subversive cracking. The branches of cracks can also help preventing the cracks from growing catastrophically. Therefore, the impact strength of composites is enhanced significantly. The reason is mechanical activation of cellulose fillers through ball milling enhanced the dispersion in epoxy with enhanced interfacial bonding between cellulose-epoxy and epoxy-basalt.

It is interesting to notice that the maximum impact performance (load as well as energy at break) of hybrid composites was observed with matt woven basalt fabrics followed by twill woven basalt. The minimum performance was observed in case of plain-woven basalt. These findings are in sharp contrast to the trends observed in tensile and bending performance. Such tendencies are also reported in previous literature (Dehkordi et al., 2010), (Rafiq et al., 2018).

Impact performance is a multiaxial load sharing unlike the tensile or bending deformations which are mostly uniaxial. When the impactor strikes the samples at a reasonably high momentum and kinetic energy, the force is radially distributed while simultaneously being transmitted through the thickness direction (Mishra et al., 2014). In case of plain-woven basalt fabrics, the constituent yarns and fibers are interlaced to the maximum extent and thus each individual layer is very firmly integrated in the axial direction. However, owing to very intensive change of plane for the interlacing yarns, the mechanical performance in the thickness direction is deteriorated. Further, the interlinking in between different layers is relatively weak which leads to delamination in certain instances. Such observations are also reported in literature (Safri et al., 2018), (Fiore et al., 2012). On the other hand, in case of weaves involving longer floats e.g., twill, matt or satin, the yarns present significantly longer lengths to bond with the adjacent laminates. This enhances the mechanical performance in the thickness direction substantially. That is the reason matt and twill basalt-based samples showed better impact performance as compared to plain woven fabric. Twill basalt shows a directional bias owing to the inclination of twill line (Z or S) direction. Therefore, it might not be as symmetrical as a matt weave. Ultimately in case of the matt construction, there is a combined advantage of longer float length as well as symmetry of the structure (Muñoz et al., 2014).

DYNAMIC MECHANICAL ANALYSIS (DMA)

Figure (Fig. 11 (a & b)) show the temperature dependence of storage modulus and tan δ respectively for the composites reinforced with different percentages of wet milled cellulosic fillers. The charts are averaged from 5 measurements for each type of composition.

The storage modulus decreases sharply in the temperature range of 60°C to 85°C. After 100°C, there is a plato on the curves. It was observed that the storage modulus increases as the cellulosic filler content increases from 1% to 3%. Such behaviour is attributed to the higher thermal stability of cellulosic nano fillers as compared to the epoxy resin. However, for 5% cellulose content, the storage modulus decreases. This could be due to nonuniform dispersion of nano fillers at higher concentrations as was observed while analysing the mechanical performance.

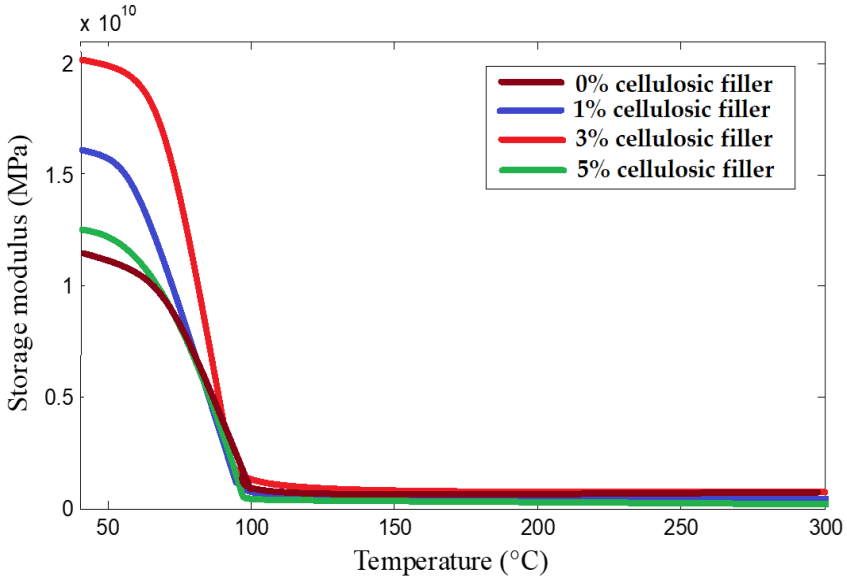

(a) Effect of cellulosic filler content on storage modulus

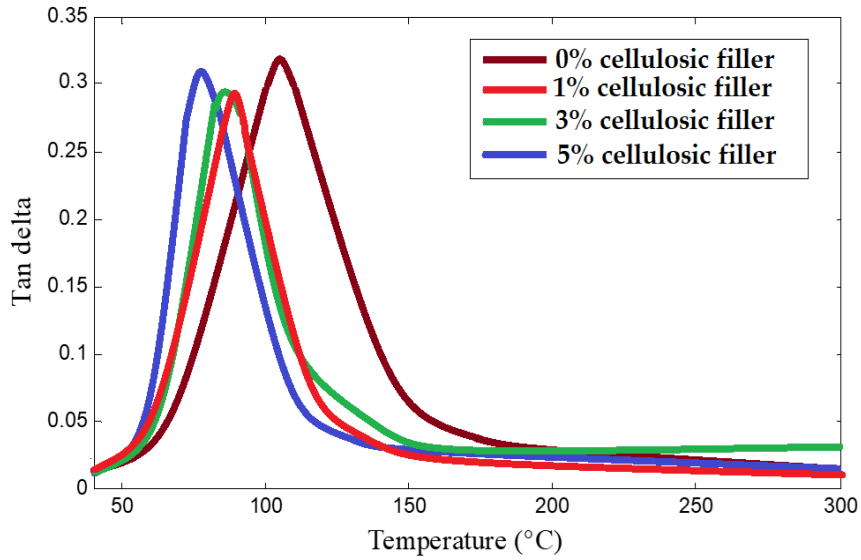

(b) Effect of cellulosic filler content on Tan δ

Fig. 11 Temperature dependence of (a) storage modulus and (b) tan δ based on cellulosic filler content in the composites.

The tan δ values shown in figure (Fig. 11 (b)) increase initially and then decrease with increasing temperature. Addition of cellulosic fillers reduces the loss modulus and consequently the tan δ of the composites. Inclusion of cellulosic fillers might have given rise to some weaker interfacial bonds as compared to a stronger and uniform intermolecular force in the pure resin. Thus, the molecules in a cellulose filled resin may start to destabilize at a lower temperature as compared to the pure resin. This could be a reason for lower Tg value for a composite with cellulosic filler as compared to pure resin.

figure (Fig. 12 (a & b)) show the temperature dependence of storage modulus and tan δ respectively for the hybrid composites reinforced with different structures of basalt fabric and partially reinforced with 3% cellulosic fillers. The charts are averaged from 5 measurements for each type of composition.

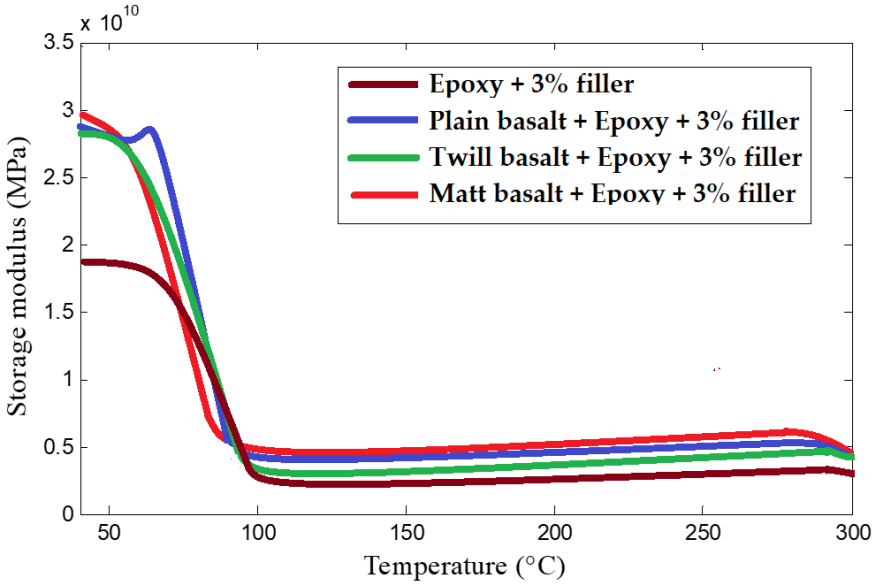

(a) Effect of basalt fabric weave on storage modulus at 3% filler content

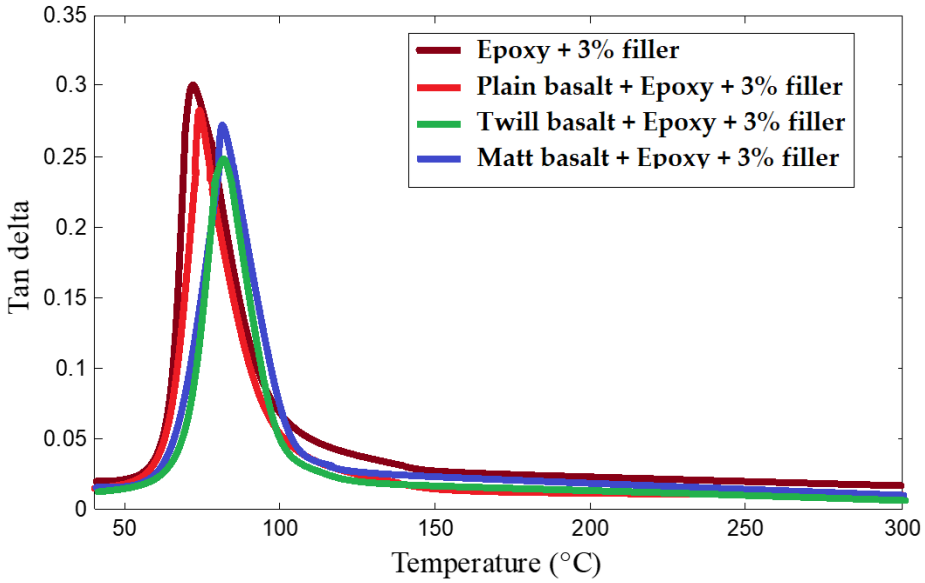

(b) Effect of basalt fabric weave on Tan δ at 3% filler content

Fig. 12 Temperature dependence of (a) storage modulus and (b) tan δ based on different basalt fabric weaves and 3% cellulosic filler content in the hybrid composites.

It can be observed from figure (Fig. 12 (a)), that the storage modulus of hybrid composite samples increases significantly due to the basalt fabrics used as reinforcement. Basalt is highly stable. at high temperatures and thus it enhances the stability of the hybrid composites. Since

the dynamic mechanical properties are mostly related to the microscale structure and molecular stability, the macroscale weave structures seem to have insignificant influence on the storage modulus and tan δ. Therefore, no significant difference in behaviour was observed between hybrid composites using plain, twill and matt structures of the basalt fabrics.

The curves of the temperature dependence of tan δ are shown in figure (Fig. 12 (b)). The composite samples show a peak at about 85° - 90°C which is closely related to the glass transition temperature (Tg) of the matrix (epoxy + nanocellulose). A further lowering in the peaks was observed after reinforcing the composites with basalt fabric. In other words, basalt helps in lowering the loss modulus and tan δ of epoxy resin along with addition of 3% wet milled cellulosic fillers.

In general, the tan δ values of composites filled with cellulosic particles are lower than that of the unfilled epoxy matrix, which proves that the addition of cellulose enhances the damping capacity of epoxy resin. All fabric constructions showed improvement in damping capacity of composites along with addition of cellulosic fillers. This fact may be explained by the addition of cellulose which increases the contributions of the hollow structure in cellulose and frictional damping, thereby leading to the decrease of the loss of energy, and thus the tan δ decreases.

Overall, both the basalt fabric as well as cellulosic fillers up to 3%, enhance the mechanical as well as thermomechanical performance of hybrid composites.

CONCLUSION

In this research, the hybridization of cellulosic filler material in matrix along with basalt woven fabric reinforcement has been proved as a successful method. The cellulosic nanofillers with size of 450nm were obtained after prolonger milling action. Mechanical properties of the basalt-epoxy-cellulose hybrid composites were determined and compared with those of regular basalt-epoxy composites. The tensile properties were determined numerically by using computational tools. The prediction of tensile performance showed relatively good agreement with the experimental results. At higher concentration of the cellulosic fillers, the properties cannot be predicted accurately due to experimental shortcomings relating to dispersion of particles. The mechanical testing of composite samples revealed that hybrid woven composites perform better in terms of energy absorption compared to nonhybrid composites. The results are in agreement with previous studies dealing with nanofillers (Mishra et al., 2012), (Tucker et al., 1999), (Halpin Affdl et al., 1976). The tensile and bending performance of hybrid composites proved to be optimum at 3% filler content. Among the various weaves of basalt fabric, plain structure showed the best tensile and bending performance. However, the best impact performance was observed for the matt weave of basalt fabric. Similar results were reported by several other researchers (Baghaei et al., 2015), (Lee et al., 2017).

Thermomechanical performance of hybrid composites improved by addition of nano fillers up to 3%. The storage modulus increased while the tan δ values decreased by addition of cellulosic fillers in the hybrid composites (Gomez, et al., 2021), (Dehkordi et al., 2010). The reinforcement of basalt fabric enabled significant increase in storage modulus irrespective of

the weave type. The high temperature resistance of basalt (Jamshaid et al., 2015), (Li et al., 2016), (Amuthakkannan et al., 2012), as well as cellulosic fillers is a contributing factor towards enhanced thermomechanical performance of such hybrid composites. The developed samples are suitable. for high performance construction materials in housing, sports, transportation applications. For these specific applications the material properties of basalt-epoxy-cellulose hybrid composites are comparable with widely used glass and carbon fiber plastics. On the other hand, the cost can be lower due to use of inexpensive bio-based filler materials. The inclusion of biological fillers is a futuristic step towards developing ecofriendly construction materials without compromising with the mechanical and thermomechanical performance.

REFERENCES

Abrate, S. Impact on Laminated Composites: Recent Advances. *Appl. Mech. Rev.* 1994, 47, 517–544.

Kretsis, G. A review of the tensile, compressive, flexural and shear properties of hybrid fibre-reinforced plastics. *Composites* 1987, 18, 13–23.

Wang, J., Waas, A.M., Wang, H. Experimental and numerical study on the low-velocity impact behavior of foam-core sandwich panels. *Compos. Struct.* 2013, 96, 298–311.

Güneş, A., Şahin, Ö.S. Investigation of the effect of surface crack on low-velocity impact response in hybrid laminated composite plates. J. *Braz. Soc. Mech. Sci. Eng.* 2020, 42, 1–20.

Swolfs, Y., Gorbatikh, L., Verpoest, I. Fibre hybridisation in polymer composites: A review. *Compos. Part A Appl. Sci. Manuf.* 2014, 67, 181–200.

Tehrani-Dehkordi, M., Nosraty, H., Rajabzadeh, M.-H. Effects of plies stacking sequence and fiber volume ratio on flexural properties of basalt/nylon-epoxy hybrid composites. *Fibers Polym.* 2015, 16, 918–925.

Simić, M., Stavrakis, A.K., Sinha, A., Premčevski, V., Markoski, B., Stojanović, G.M. Portable Respiration Monitoring System with an Embroidered Capacitive Facemask Sensor. *Biosensors* 2022, 12, 339.

Zhang, D., Sun, Y., Chen, L., Pan, N. A comparative study on low-velocity impact response of fabric composite laminates. *Mater. Des.* 2013, 50, 750–756.

Sarasini, F., Tirillò, J., Ferrante, L., Valente, M., Valente, T., Lampani, L., Gaudenzi, P., Cioffi, S., Iannace, S., Sorrentino, L. Drop-weight impact behaviour of woven hybrid basalt–carbon/epoxy composites. *Compos. Part B Eng.* 2013, 59, 204–220.

Stavrakis, A.K., Simić, M., Stojanović, G.M. Electrical Characterization of Conductive Threads for Textile Electronics. *Electronics* 2021, 10, 967.

Karataş, M.A., Gökkaya, H. A review on machinability of carbon fiber reinforced polymer (CFRP) and glass fiber reinforced polymer (GFRP) composite materials. *Def. Technol*. China Ordnance Soc. 2018, 14, 318–326.

Sinha, A., Dhanjai, Stavrakis, A.K., Stojanović, G.M. Textile-based electrochemical sensors and their applications. *Talanta* 2022, 244, 123425.

Stavrakis, A.K., Simić, M., Stojanović, G.M. A Study of the Performance Degradation of Conductive Threads Based on the Effects of Tensile Forces and Repeated Washing. *Polymers* 2022, 14, 4581.

Sinha, A., Stavrakis, A.K., Simić, M., Stojanović, G.M. Polymer-Thread-Based Fully Textile Capacitive Sensor Embroidered on a Protective Face Mask for Humidity Detection. *ACS Omega* 2022, 7, 44928–44938.

Sinha, A., Stavrakis, A.K., Simić, M., Stojanović, G.M. Wearable humidity sensor embroidered on a commercial face mask and its electrical properties. J. *Mater. Sci.* 2023, 58, 1680–1693.

Jamshaid, H., Mishra, R. A green material from rock: Basalt fiber—A review. J. *Text. Inst.* 2015, 107, 923–937.

Li, Z., Xiao, T., Zhao, S. Effects of surface treatments on Mechanical properties of Continuous basalt fibre cords and their Adhesion with rubber matrix. *Fibers Polym.* 2016, 17, 910–916.

Wang, X., Hu, B., Feng, Y., Liang, F., Mo, J., Xiong, J., Qiu, Y. Low velocity impact properties of 3D woven basalt/aramid hybrid composites. *Compos. Sci. Technol.* 2008, 68, 444–450.

Amuthakkannan, P., Manikandan, V., Jappes, J.T.W., Uthayakumar, M. Influence of stacking sequence on mechanical properties of basalt-jute fiber-reinforced polymer hybrid composites. *J. Polym. Eng.* 2012, 32, 547–554.

Azadi, M., Dadashi, A., Dezianian, S., Kianifar, M., Torkaman, S., Chiyani, M. High-Cycle Bending Fatigue Properties of Additive-Manufactured ABS and PLA Polymers Fabricated by Fused Deposition Modeling 3D-Printing. *Forces Mech.* 2021, 3, 100016.

Kariz, M., Sernek, M., Obućina, M., Kuzman, M.K. Effect of Wood Content in FDM Filament on Properties of 3D Printed Parts. Mater. *Today Commun.* 2018, 14, 135–140.

Yao, T., Deng, Z., Zhang, K., Li, S. A Method to Predict the Ultimate Tensile Strength of 3D Printing Polylactic Acid (PLA) Materials with Different Printing Orientations. *Compos. Part B Eng.* 2019, 163, 393–402.

Daver, F., Lee, K.P.M., Brandt, M., Shanks, R. Cork–PLA Composite Filaments for Fused Deposition Modelling. *Compos. Sci. Technol.* 2018, 168, 230–237.

Tanikella, N.G., Wittbrodt, B., Pearce, J.M. Tensile Strength of Commercial Polymer Materials for Fused Filament Fabrication 3D Printing. *Addit. Manuf.* 2017, 15, 40–47.

Tiwary, V.K., Arunkumar, P., Kulkarni, P.M. Micro-Particle Grafted Eco-Friendly Polymer Filaments for 3D Printing Technology. *Mater. Today Proc.* 2020, 28, 1980–1984.

Mishra, R., Wiener, J. Petru, M. & Novotna, J. Bio-Composites Reinforced with Natural Fibers: Comparative Analysis of Thermal, Static and Dynamic-Mechanical Properties. *Fiber Polym.,* 2020, 21(3), 619-627.

Pincheira, G., Canales, C., Medina, C., Fernández, E., Flores, P. Influence of aramid fibers on the mechanical behavior of a hybrid carbon–aramid–reinforced epoxy composite. *Proc. Inst. Mech. Eng. Part L J. Mater. Des. Appl.* 2015, 232, 58–66.

Baghaei, B., Skrifvars, M., Berglin, L. Characterization of thermoplastic natural fibre composites made from woven hybrid yarn prepregs with different weave pattern. *Compos. Part A Appl. Sci. Manuf.* 2015, 76, 154–161.

Sezgin, H., Berkalp, O.B. The effect of hybridization on significant characteristics of jute/glass and jute/carbon-reinforced composites. *J. Ind. Text.* 2016, 47, 283–296.

Lee, J.S., Kim, J.W. Impact response of carbon fibre fabric/thermoset-thermoplastic combined polymer composites. *Compos. Adv. Lett.* 2017, 26, 82–88.

Rajasekar, B.R., Asokan, R., Senbagan, M., Karthika, R., Sivajyothi, K., Sharma, N. Evaluation on mechanical properties of intra-ply hybrid carbon-aramid/epoxy composite laminates. *Mater. Today Proc.* 2018, 5, 25323–25330.

Swolfs, Y., McMeeking, R.M., Verpoest, I., Gorbatikh, L. The effect of fibre dispersion on initial failure strain and cluster development in unidirectional carbon/glass hybrid composites. *Compos. Part A Appl. Sci. Manuf.* 2015, 69, 279–287.

Gomez, C., Salvatori, D., Caglar, B., Trigueira, R., Orange, G., Michaud, V. Resin Transfer molding of High-Fluidity Polyamide-6 with modified Glass-Fabric preforms. *Compos. Part A Appl. Sci. Manuf.* 2021, 147, 106448.

Baek, I., Lee, S. A Study of Films Incorporating Magnetite Nanoparticles as Susceptors for Induction Welding of Carbon Fiber Reinforced Thermoplastic. *Materials* 2020, 13, 318.

Minchenkov, K., Vedernikov, A., Safonov, A., Akhatov, I. Thermoplastic Pultrusion: A Review. *Polymers* 2021, 13, 180.

Bandaru, A.K., Sachan, Y., Ahmad, S., Alagirusamy, R., Bhatnagar, N. On the mechanical response of 2D plain woven and 3D angle-interlock fabrics. *Compos. Part B Eng.* 2017, 118, 135–148.

Minchenkov, K., Vedernikov, A., Kuzminova, Y., Gusev, S., Sulimov, A., Gulyaev, A., Kreslavskaya, A., Prosyanoy, I., Xian, G., Akhatov, I., et al. Effects of the quality of pre-consolidated materials on the mechanical properties and morphology of thermoplastic pultruded flat laminates. *Compos. Commun.* 2022, 35, 101281.

Cerit, A., Marti, M.E., Soydal, U., Kocaman, S., Ahmetli, G. Effect of Modification with Various Epoxide Compounds on Mechanical, Thermal, and Coating Properties of Epoxy Resin. *Int. J. Polym. Sci.* 2016, 4968365.

Ahmetli, G., Yazicigil, Z., Soydal, U. Modification of the epoxy resin with epoxide and ester group containing oligomers and compounds. *Proceedings of the Estonian Academy of Sciences,* 2015, 64(1S), 71-76.

Subagia, I.A., Sugita, I.K.G., Wirawan, I.K.G., Dwidiani, N.M., Yuwono, A.H.Y.A.H. Thermal Conductivity of Carbon/Basal Fiber Reinforced Epoxy Hybrid Composites. *Int. J. Technol.* 2017, 8, 1498–1506.

Vedernikov, A., Minchenkov, K., Gusev, S., Sulimov, A., Zhou, P., Li, C., Xian, G., Akhatov, I., Safonov, A. Effects of the Pre-Consolidated Materials Manufacturing Method on the Mechanical Properties of Pultruded Thermoplastic Composites. *Polymers* 2022, 14, 2246.

Zhou, P., Li, C., Bai, Y., Dong, S., Xian, G., Vedernikov, A., Akhatov, I., Safonov, A., Yue, Q. Durability study on the interlaminar shear behavior of glass-fibre reinforced polypropylene (GFRPP) bars for marine applications. *Constr. Build. Mater.* 2022, 349, 128694.

Pavlovski, D., Mislavsky, B., Antonov, A. CNG cylinder manufacturers test basalt fibre. *Reinf. Plast.* 2007, 51, 36–39.

Aji, I.S., Zainudin, E.S., Khalina, A., Sapuan, S.M., Khairul, M.D., Sapuan, M.S. Thermal property determination of hybridized kenaf/PALF reinforced HDPE composite by thermogravimetric analysis. *J. Therm. Anal. Calorim.* 2011, 109, 893–900.

Banea, M.D., de Sousa, F.S.M., da Silva, L.F.M., Campilho, R.D.S.G., de Pereira, A.M.B. Effects of Temperature and Loading Rate on the Mechanical Properties of a High Temperature Epoxy Adhesive. *J. Adhes. Sci. Technol.* 2011, 25, 2461–2474.

Muller, M., Sleger, V., Kolar, V., Hromasova, M., Pis, D., Mishra, R.K. Low-Cycle Fatigue Behavior of 3D-Printed PLA Reinforced with Natural Filler. *Polymers.* 2022, 14, 1301.

Jarukumjorn, K., Suppakarn, N. Effect of glass fiber hybridization on properties of sisal fiber–polypropylene composites. *Compos. Part B Eng.* 2009, 40, 623–627.

Sahu, P., Gupta, M. Sisal (Agave sisalana) fibre and its polymer-based composites: A review on current developments. *J. Reinf. Plast. Compos.* 2017, 36, 1759–1780.

Sen, A.K., Kumar, S. Coir-fiber-based fire retardant nano filler for epoxy composites. *J. Therm. Anal. Calorim.* 2010, 101, 265–271.

Ayrilmis, N., Buyuksari, U., Dundar, T. Waste Pine Cones as a Source of Reinforcing Fillers for Thermoplastic Composites. *J. Appl. Polym. Sci.* 2010, 117, 2324–2330.

Ruggiero, A., Valasek, P., Mueller, M. Exploitation of Waste Date Seeds Phoenix Dactylifera in Form of Polymeric Particle Biocomposite: Investigation on Adhesion, Cohesion. *Compos. Part B Eng.* 2016, 104, 9–16.

ASTM D3039/D3039M-08, Standard Test Method for Tensile Properties of Polymer Matrix Composite Materials. *ASTM International: West Conshohocken*, PA, USA, 2014.

ASTM D7264/D7264M-07, Standard Test Method for Flexural Properties of Polymer Matrix Composite Materials. *ASTM International: West Conshohocken*, PA, USA, 2015.

ASTM D7136/D7136M-15, Standard Test Method for Measuring the Damage Resistance of a Fiber-Reinforced Polymer Matrix Composite to a Drop-Weight Impact Event. *ASTM International: West Conshohocken*, PA, USA, 2020.

Pakkanen, J., Manfredi, D., Minetola, P., Iuliano, L. About the Use of Recycled or Biodegradable Filaments for Sustainability of 3D Printing. In Proceedings of *the Sustainable Design and Manufacturing 2017*, Campana, G., Howlett, R.J., Setchi, R., Cimatti, B., Eds., Springer International Publishing: Cham, Germany,2017, pp. 776–785.

Zhao, D.X., Cai, X., Shou, G.Z., Gu, Y.Q., Wang, P.X. Study on the Preparation of Bamboo Plastic Composite Intend for Additive Manufacturing. *Key Eng. Mater.* 2016, 667, 250–258.

Antonio Travieso-Rodriguez, J., Zandi, M.D., Jerez-Mesa, R., Lluma-Fuentes, J. Fatigue Behavior of PLA-Wood Composite Manufactured by Fused Filament Fabrication. *J. Mater. Res. Technol.* 2020, 9, 8507–8516.

Svatik, J., Lepcio, P., Ondreas, F., Zarybnicka, K., Zboncak, M., Mencik, P., Jancar, J. PLA Toughening via Bamboo-Inspired 3D Printed Structural Design. *Polym. Test.* 2021, 104, 107405.

Correa, D., Papadopoulou, A., Guberan, C., Jhaveri, N., Reichert, S., Menges, A., Tibbits, S. 3D-Printed Wood: Programming Hygroscopic Material Transformations. 3D Print. Addit. Manuf. 2015, 2, 106–116.

Mishra, R., Tiwari, R., Marsalkova, M., Behera, B.K. Effect of TiO2 Nanoparticles on Basalt/Polysiloxane Composites: Mechanical and Thermal Characterization. *J. Text. Inst.* 2012, 103, 1361–1368.

Tucker, C.L., Liang, E. Stiffness predictions for unidirectional short-fiber composites: Review and evaluation. *Compos. Sci. Technol.* 1999, 59, 655–671.

Halpin Affdl, J.C., Kardos, J.L. The Halpin-Tsai equations: A review. *Polym. Eng. Sci.* 1976, 16, 344–352,

Budarapu, P.R., Zhuang, X., Rabczuk, T., Bordas, S.P. Multiscale modeling of material failure: Theory and computational methods. *Adv. Appl. Mech.* 2019, 52, 1–103,

Behera, B.K. & Mishra, R. Artificial neural network-based prediction of aesthetic and functional properties of worsted suiting fabrics. *Int. J. Cloth. Sci. Tech,* 2007, 19(5), 259-276.

Behera, B.K., Pattanayak, A.K. & Mishra, R.K. Prediction of fabric drape behaviour using finite element method, *J. Text. Eng.*, 2008, 54(4), 103 – 110.

Gama, N., Ferreira, A., Barros-Timmons, A. 3D Printed Cork/Polyurethane Composite Foams. *Mater. Des.* 2019, 179, 107905.

Senatov, F.S., Niaza, K.V., Stepashkin, A.A., Kaloshkin, S.D. Low-Cycle Fatigue Behavior of 3d-Printed PLA-Based Porous Scaffolds. *Compos. Part B Eng.* 2016, 97, 193–200.

Essassi, K., Rebiere, J.-L., El Mahi, A., Ben Souf, M.A., Bouguecha, A., Haddar, M. Experimental and Analytical Investigation of the Bending Behaviour of 3D-Printed Bio-Based Sandwich Structures Composites with Auxetic Core under Cyclic Fatigue Tests. *Compos. Part A Appl. Sci. Manuf.* 2020, 131, 105775.

Yang, T., Saati, F., Horoshenkov, K., Xiong, X. & Mishra, R. Study on the sound absorption behavior of multi-component polyester nonwovens: experimental and numerical methods. *Text. Res. J.* 2019, 89(16), 3342–3361.

Ayrilmis, N. Effect of Layer Thickness on Surface Properties of 3D Printed Materials Produced from Wood Flour/PLA Filament. *Polym. Test.* 2018, 71, 163–166.

Yang, T., Xiong, X., Mishra, R., Novák, J., Militký, J. Acoustic evaluation of Struto nonwovens and their relationship with thermal properties. *Text. Res. J.* 2018, 88, 426–437.

Huber, T., Müssig, J. Fibre Matrix Adhesion of Natural Fibres Cotton, Flax and Hemp in Polymeric Matrices Analyzed with the Single Fibre Fragmentation Test. *Compos. Interfaces* 2008, 15, 335–349.

Shahar, F.S., Sultan, M.T.H., Safri, S.N.A., Jawaid, M., Abu Talib, A.R., Basri, A.A., Shah, A.U.M. Fatigue and Impact Properties of 3D Printed PLA Reinforced with Kenaf Particles. *J. Mater. Res. Technol.* 2022, 16, 461–470.

Yao, T., Zhang, K., Deng, Z., Ye, J. A Novel Generalized Stress Invariant-Based Strength Model for Inter-Layer Failure of FFF 3D Printing PLA Material. *Mater. Des.* 2020, 193, 108799.

Le Duigou, A., Correa, D., Ueda, M., Matsuzaki, R., Castro, M. A Review of 3D and 4D Printing of Natural Fibre Biocomposites. *Mater. Des.* 2020, 194, 108911.

Arockiam, A.J., Subramanian, K., Padmanabhan, R.G., Selvaraj, R., Bagal, D.K., Rajesh, S. A Review on PLA with Different Fillers Used as a Filament in 3D Printing. *Mater. Today Proc.* 2022, 50, 2057–2064.

Le Duigou, A., Castro, M., Bevan, R., Martin, N. 3D Printing of Wood Fibre Biocomposites: From Mechanical to Actuation Functionality. *Mater. Des.* 2016, 96, 106–114.

Calì, M., Pascoletti, G., Gaeta, M., Milazzo, G., Ambu, R. New Filaments with Natural Fillers for FDM 3D Printing and Their Applications in Biomedical Field. *Procedia Manuf.* 2020, 51, 698–703.

Wang, Z., Xu, J., Lu, Y., Hu, L., Fan, Y., Ma, J., Zhou, X. Preparation of 3D Printable. Micro/Nanocellulose-Polylactic Acid (MNC/PLA) Composite Wire Rods with High MNC Constitution. *Ind. Crop. Prod.* 2017, 109, 889–896.

Li, T., Aspler, J., Kingsland, A., Cormier, L.M., Zou, X. 3d Printing—A Review of Technologies, Markets, and Opportunities for the Forest Industry. *J. Sci. Technol. For. Prod. Process* 2016, 5, 30.

Chacon, J.M., Caminero, M.A., Garcia-Plaza, E., Nunez, P.J. Additive Manufacturing of PLA Structures Using Fused Deposition Modelling: Effect of Process Parameters on Mechanical Properties and Their Optimal Selection. *Mater. Des.* 2017, 124, 143–157.

Ying, S., Mengyun, T., Zhijun, R., Baohui, S., Li, C. An experimental investigation on the low-velocity impact response of carbon–aramid/epoxy hybrid composite laminates. *J. Reinf. Plast. Compos.* 2016, 36, 422–434.

Dehkordi, M.T., Nosraty, H., Shokrieh, M.M., Minak, G., Ghelli, D. Low velocity impact properties of intra-ply hybrid composites based on basalt and nylon woven fabrics. *Mater. Des.* 2010, 31, 3835–3844.

Rafiq, A., Merah, N. Nanoclay enhancement of flexural properties and water uptake resistance of glass fiber-reinforced epoxy composites at different temperatures. *J. Compos. Mater.* 2018, 53, 143–154.

Mishra, R. & Behera, B.K. Novelties of 3-D woven composites and nanocomposites. *J. text. I.*, 2014, 105(1), 84-92.

Safri, S.N.A., Sultan, M.T.H., Jawaid, M., Jayakrishna, K. Impact behaviour of hybrid composites for structural applications: A review. *Compos. Part B Eng.* 2018, 133, 112–121.

Fiore, V., Valenza, A., Di Bella, G. Mechanical behavior of carbon/flax hybrid composites for structural applications. *J. Compos. Mater.* 2012, 46, 2089–2096.

Muñoz, R., Martínez, V., Sket, F., González, C., Llorca, J. Mechanical behavior and failure micromechanisms of hybrid 3D woven composites in tension. *Compos. Part A Appl. Sci. Manuf.* 2014, 59, 93–104.

Temperature dependence of photovoltaic cells characteristics

M. Zholobov[1], P. Kouřím[1], M. Libra[1], V. Poulek[1], J. Šafránková[1]

[1]Department of Physics, Faculty of Engineering, Czech University of Life Sciences Prague, Prague, Czech Republic

Abstract

In this article, we present selected results of temperature dependence of photovoltaic cells characteristics. The characteristics were measured in the wide temperature interval. The results are in a good agreement with the physical theory of semiconductors.

Key words: Photovoltaic cell, photovoltaics, energy conversion

INTRODUCTION

We monitored the behaviour of important characteristics of the photovoltaic cells based on monocrystalline silicon in the wide temperature range (Libra et al., 2021). The efficiency of the photovoltaic energy conversion depends on the temperature significantly. The temperature changes of important characteristics correspond with the physical theory of solid states (Kittel, 2005). The consequently evaluated data are presented in this article.

MATERIALS AND METHODS

The PV cells based on monocrystalline silicon was used for the measurement. The vacuum chamber was used to prevent condensation of air humidity on the cooled photovoltaic cell. The halogen incandescent lamp with a reflector was the source of radiation. It illuminated the chamber through a window of clear acrylate glass. The spectrum of this radiation is continuous and is similar to that of a black body at about 2900 °C. The radiation intensity on the photovoltaic cell was 297 $W.m^{-2}$, which is less than the intensity of direct sunlight, but there was no significant heating up of the photovoltaic cell by the incident radiation. The liquid nitrogen was the cooling medium, a small-plate cooker with autotransformer power control was the heat source.

RESULTS AND DISCUSSION

Figures (Fig.1, Fig. 2) show the characteristics of the photovoltaic cell measured over a very wide temperature range from −100 °C to +100 °C. The increase of the temperature causes a reduction in the instantaneous power of the photovoltaic cell at a constant radiation intensity and thus a reduction in the efficiency of the photovoltaic energy conversion. If the photovoltaic system operates in locations with extreme climatic conditions, especially with extreme temperature changes during the year or even in space, the electrical voltage of the photovoltaic modules will change significantly as well as the instantaneous power.

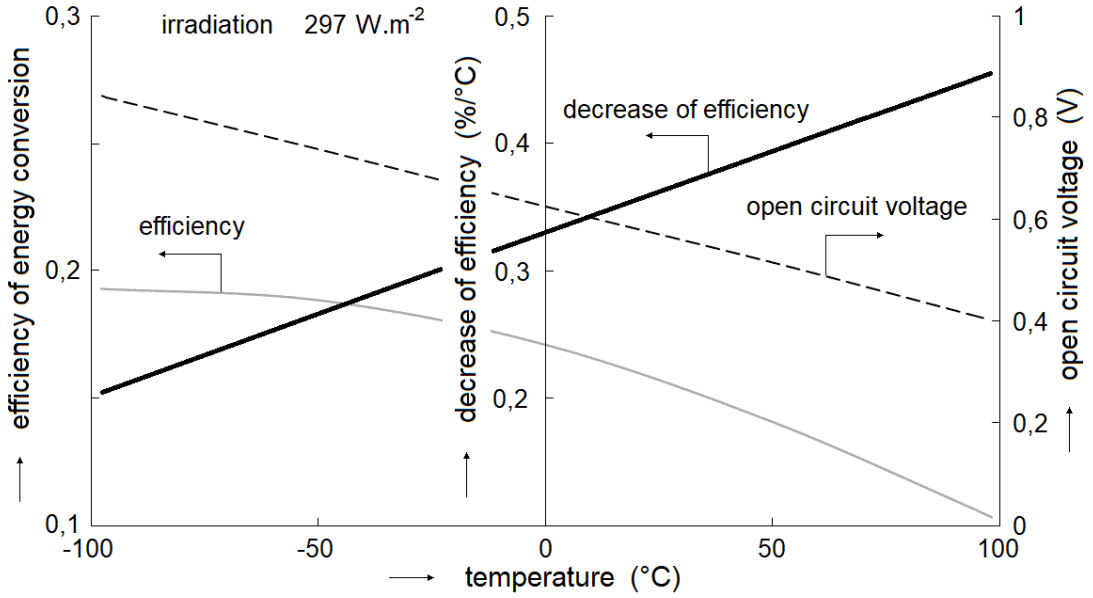

Fig. 1 Dependences of open circuit voltage and energy conversion efficiency on temperature.

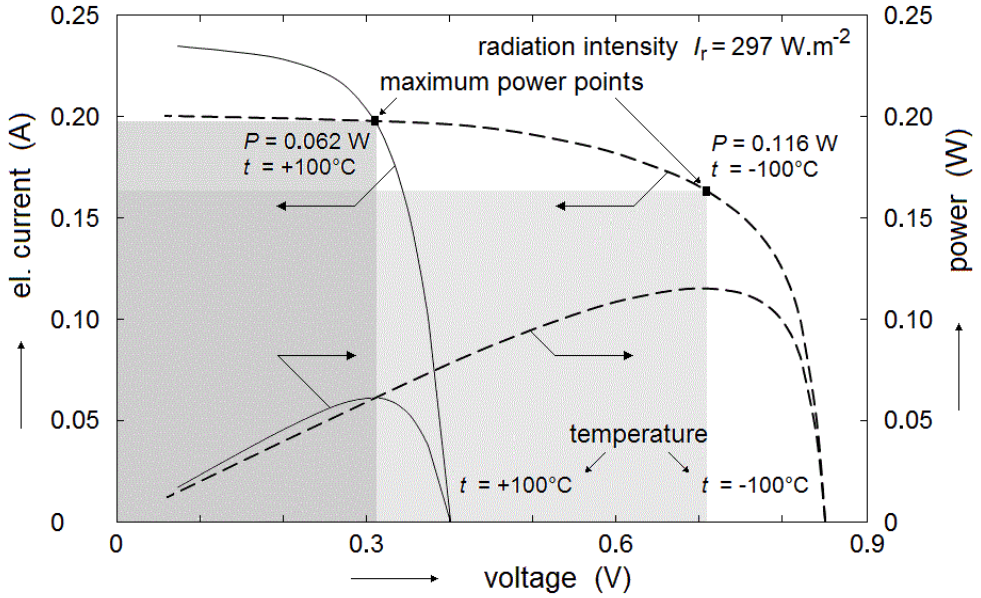

Fig. 2 *I-U* and *P-U* characteristics at two selected temperatures.

Thus, the efficiency of energy conversion and open circuit voltage can up to double on Earth in extreme climatic conditions during the year. In space applications, these values can triple in a single satellite orbit around the Earth.

CONCLUSION

The temperature significantly influences the important characteristics of the photovoltaic cells. This effect must be taken into account in the design of the photovoltaic system, and the individual components must be carefully selected. Especially, electronic inverters tend to be sensitive to overvoltage or undervoltage. The rectangles marked in figure (Fig. 2) corresponds with the instantaneous power. The difference is seen.

REFERENCES

Libra, M., Petrík, T., Poulek, V., Tyukhov, I.I., Kouřím, P.: Changes in the Efficiency of Photovoltaic Energy Conversion in Temperature Range With Extreme Limits. IEEE Journal of Photovoltaics, 2021, 11(6): 1476-1481.

Kittel, CH., Introduction to solid state physics. Danvers, MA, USA: Wiley, 2005.

Corresponding author:

Ing. Maxim Zholobov, Department of Physics, Faculty of Engineering, Czech University of Life Sciences Prague, Kamýcká 129, Praha 6, Prague, 16521, Czech Republic, email: zholobov@tf.czu.cz

Proceeding of 25th International Conference of Young Scientists 2023

September 12th 2023 – September 13th 2023

Publisher:	Czech University of Life Sciences Prague Kamýcká 129, Prague, Czech Republic
Editors:	Rostislav Chotěborský, Barbora Černilová, Lenka Křivánková
Printing house:	CULS Prague
Number of copies:	0
Number of pages:	102
Issue:	First
Year:	2023
ISBN	978-80-213-3345-1